TRAJECTORY SIMULATIONS OF H_2O, O_3, AND CO IN THE UPPER TROPOSPHERE AND LOWER STRATOSPHERE (UTLS)

A Dissertation

by

TAO WANG

Submitted to the Office of Graduate and Professional Studies of
Texas A&M University
in partial fulfillment of the requirements for the degree of

DOCTOR OF PHILOSOPHY

Chair of Committee,	Andrew E. Dessler
Committee Members,	Mark R. Schoeberl
	Kenneth P. Bowman
	Renyi Zhang
	Shaima L. Nasiri
Head of Department,	Ping Yang

May 2014

Major Subject: Atmospheric Sciences

Copyright 2014 Tao Wang

ABSTRACT

The purpose of this work is to simulate water vapor (H_2O), ozone (O_3), and carbon monoxide (CO) in the upper troposphere and lower stratosphere (UTLS) using a domain-filling, forward trajectory model. The influx of H_2O to the UTLS is largely determined by the large-scale troposphere-to-stratosphere transport in the tropics, during which air is dehydrated across the cold tropical tropopause. In the domain-filling, forward trajectory model, trajectories are initialized in the upper troposphere, and the circulation is based on reanalysis wind fields. Along the trajectories, winds determine the pathways of parcels and temperature determines the H_2O content through an idealized saturation calculation. Compared with the Aura Microwave Limb Sounder (MLS) measurements, this simple advection-condensation strategy yields reasonable results for H_2O in the stratosphere in terms of both seasonal variability and vertical structures. The detailed global dehydration patterns are also revealed from this model and it improves our understanding of the H_2O and its transport within the UTLS.

Besides H_2O, ozone (O_3) and carbon monoxide (CO) are also important trace gases in the UTLS linked to circulation, transport and climate forcing (for O_3). Combined with simple parameterization of chemical production and loss rates from the Whole Atmosphere Community Climate Model (WACCM), we also managed to simulate O_3 and CO transport in the UTLS via this trajectory model. The trajectory modeled O_3 and CO show good overall agreement with satellite observations from the MLS and the Atmospheric Chemistry Experiment Fourier Transform Spectrometer (ACE-FTS) in terms of spatial structure and seasonal variability. The trajectory model results also agree well with the Eulerian WACCM simulations. Analysis of the simulated tracers shows that seasonal variations in tropical upwelling exerts strong influence on O_3 and CO in the tropical lower stratosphere, and the coupled seasonal cycles provide a useful test of the transport simulations. Interannual variations in the tracers are also closely coupled to changes in upwelling, and the trajectory model can accurately capture and explain observed changes. This demonstrates the importance of variability in tropical upwelling in forcing chemical changes in the tropical UTLS.

Trajectory modeling of O_3 and CO can provide useful tests for simplified understanding of transport and chemical processes in the UTLS, and provide complementary information to the H_2O simulations, which are primarily constrained by tropopause temperatures. This model is easy to use, easy to diagnose, and the Lagrangian perspective makes it exceptionally useful in studying transport processes within the UTLS.

ACKNOWLEDGEMENTS

I thank my advisor, Prof. Andrew Dessler for offering me this opportunity to study and work on this interesting topic. I feel much appreciated for his support and encouragement during my work. Prof. Dessler's profound insights into global climate change inspire me greatly to keep exploring many cutting-edge issues in this field. The whole journey working with Prof. Dessler has always been so much fun and inspiring, but never dull for a moment. I thank him for supporting me to continue my education in Texas A&M University for the past four and a half years.

Many thanks to my committee members, Prof. Kenneth Bowman, Prof. Shaima Nasiri and Prof. Renyi Zhang, for giving me many valuable suggestions through my work. By working through some detailed questions brought by them, I learned even more. Great appreciation goes to Prof. Nasiri especially, for many helpful instructions on not just science but also on writing.

Besides, I feel grateful for having the opportunity working with two of the top scientists in the world: Dr. Mark Schoeberl and Dr. William Randel. Working with them is indeed a once-in-a-life experience for me, and for this I feel extremely honored. Their critical thinking and inexhaustible supply of ideas and enthusiasm have been the source of this project. I especially feel grateful for Dr. Randel's help during the entire journey – there are so much to learn from you!

I would like to thank all friends and colleagues in this department for making my journey here enjoyable. Thank Neil Smith for endless help on IT issues, thank Barbara Straube, Renee Campos, Mellisa Mathews, etc. for all kinds of help in the department.

Great thanks to our group members Chen Zhou, John Kummer, and Hao Ye for their helpful discussions with me.

Lastly, I want to take this opportunity to thank my parents and my brother for their endless love and support for those years. Thank them to always have faith on me. Deep appreciation goes to my wife for her unconditional love and support in every possible way. I feel so lucky to have her in my companionship for the rest of my life.

TABLE OF CONTENTS

LIST OF TABLES

LIST OF FIGURES

Page

.

.

1. INTRODUCTION

The upper troposphere and lower stratosphere (UTLS) is crucial for the Earth's energy balance, as changes in the composition of the UTLS, such as water vapor and ozone, have a direct impact on the radiative forcing of the atmosphere. This forcing can influence the global circulation, and could conceivably alter the entire climate system. Understanding the UTLS region requires knowledge of the coupled radiation, dynamics, chemistry, and transport processes in the atmosphere.

1.1 The Upper Troposphere and Lower Stratosphere (UTLS)

The sun provides the source of energy for the atmosphere. The earth absorbs short-wave radiation from the sun after it travels through the atmosphere, resulting in a warm surface. The warm surface also emits long-wave radiation back to the space. Due to the absorption of long-wave radiation by radiatively active chemical species, such as carbon dioxide (CO_2), water vapor (H_2O) and ozone (O_3), the lower atmosphere is heated consistently. Since the primary heat source is the surface, air temperature will be the warmest at the surface and decrease steadily with height. This region of air is known as the troposphere. Above the troposphere is the stratosphere, in which temperature increases with height between about 12-50 km.

From the transport perspective, the atmosphere is divided into three regions: the "overworld", the "middleworld", and the "underworld" following *Hoskins* [1991] (Fig. 1.1). The overworld is defined as the region above the 380-K potential temperature surface (isentrope, thick dashed line in Fig. 1.1), where air is stratospheric at all latitudes. Here, seasonally dependent meridional transport is faster. The underworld is defined to be the region below the 320-K isentrope where air is tropospheric at all latitudes. The region between overworld and underworld is usually referred as the middleworld, characterized by tropospheric air at low latitudes and stratospheric air at high latitudes. The stratospheric part of the middleworld is often called the “lowermost stratosphere” (LMS). Here isentropes intersect the tropopause (thick blue line) and potentially connect the troposphere with the stratosphere via rapid adiabatic motions.

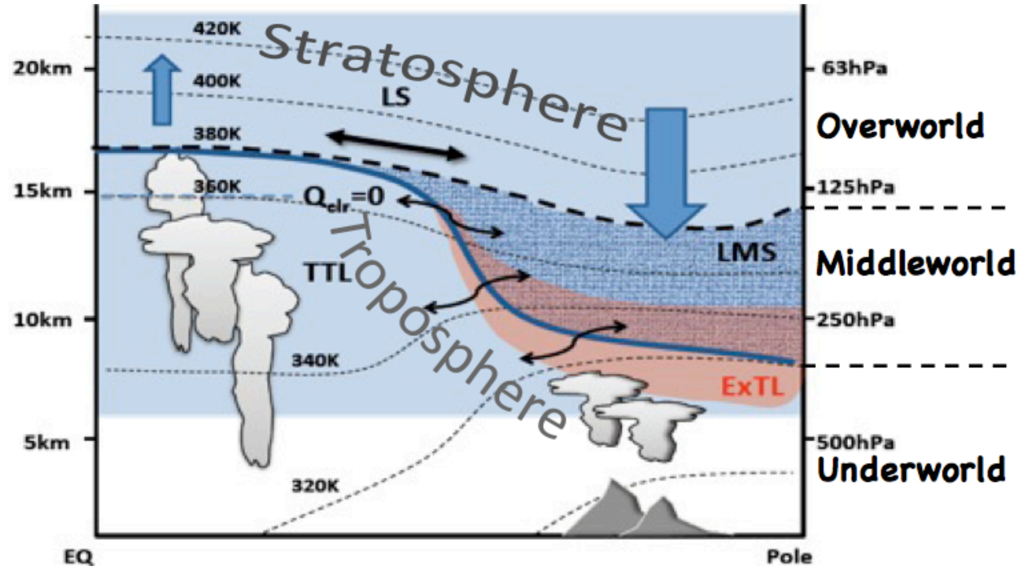

Figure 1.1. Schematic of the Upper Troposphere and Lower Stratosphere (UTLS). The tropical UTLS – Tropical Tropopause Layer (TTL), extends from the level of deep convective outflow, through the level of zero clear-sky radiative heating up to the cold point and the thermal tropopause (thick blue line). The extra-tropical UTLS contains the lowermost stratosphere (LMS) air between the 380-K isentrope and the tropopause (usually PV tropopause). Red is the Extra-tropical Transition Layer (ExTL) that represents a mixing layer in which air has partly tropospheric, partly stratospheric chemical characteristics. The lower stratospheric (LS) branch of the Brewer-Dobson wave driven circulation is shown in blue arrows. Faster and seasonally dependent meridional transport between the tropics and extra-tropics is found within the 380-420 K isentropes (the “overworld”, black straight arrow). Modified from *SPARC CCMVal* [2010].

From the above convention, the Upper Troposphere and Lower Stratosphere (UTLS) is defined as the region lying between the troposphere and the stratosphere, from roughly 8 to 22 km (see Fig. 1.1). Air in the UTLS is chemically and dynamically distinct from those that are pure stratospheric (above 380-K overworld) or tropospheric (below 310-K underworld). In fact, it exhibits features of both the troposphere and the stratosphere [*Holton et al.*, 1995; *Highwood and Hoskins*, 1998; *Sherwood and Dessler*, 2000].

The tropical part of the UTLS is known as the tropical tropopause layer (TTL), which is usually defined as the tropic region between 14-18.5 km, 355-425 K in isentrope, or 150-70 hPa in pressure (see Fig. 1.1) [*Fueglistaler et al.*, 2009a]. Here, the atmosphere experiences an important transition from a balance between latent heating and radiative cooling in the troposphere to a balance between tropical radiative heating and extratopical cooling in the stratosphere. From the perspective of transport, the level of zero clear-sky radiative heating, which changes from positive above ~15 km to negative below, is generally considered the base of the TTL. The maximum height of outflow from convective towers demarcates the TTL upper boundary [*Highwood and Hoskins*, 1998; *Sherwood and Dessler*, 2000; *Fueglistaler et al.*, 2009a]. The TTL is maintained by the interaction of convective transport, convectively generated waves, radiation, cloud microphysics and the large-scale stratospheric circulation. Most of the air enters the stratosphere through the TTL, known as the ascending branch of the Brewer-Dobson circulation [*Brewer*, 1949]. Clouds in the TTL, especially thin cirrus clouds, have a significant impact on the radiation balance [*Rosenfield et al.*, 1998; *Gettelman et al.*, 2004].

The extratropical part of the UTLS is essentially the lowermost stratosphere (LMS). Here, the isentropes intersect the tropopause, potentially connecting the troposphere and the stratosphere via rapid adiabatic motion (doubled headed lines in Fig. 1.1). The slower diabatic circulation is predominantly downward in the LMS, which controls the flux and variability of many chemical species into the troposphere (see Sect. 4). These species include lower stratospheric O_3 and mesosphere carbon monoxide (CO), both of which exert a crucial influence over both the radiative budget and the chemistry of the upper troposphere. The lower boundary of the LMS is the so-called Extra-tropical Transition Layer (ExTL) – the extratropical layer around the tropopause, in parallel to the TTL in the tropics [*Gettelman et al.*, 2011], where, like in the TTL, air exhibits both tropospheric and stratospheric feature.

It is well known that the mixing timescales are much more rapid in the troposphere than in the stratosphere [e.g., *Fueglistaler et al.*, 2009a; *Gettelman et al.*, 2011]. In the TTL and the ExTL, this leads to a sharp change in the concentration of chemical species that have moderate lifetimes, such as O_3 (high in the stratosphere and low in the troposphere), H_2O, and CO (high in the troposphere and low in the stratosphere).

1.2 H_2O, O_3, and CO in the UTLS

1.2.1 H_2O in the UTLS

Water vapor (H_2O) is the most important greenhouse gas in the atmosphere. Understanding the mechanisms that regulate it is very important for understanding past and future climate change. Of particular interest is H_2O in the UTLS. Besides its potential effect on stratospheric ozone loss [*Vogel et al.*, 2011; *Anderson et al.*, 2012], H_2O and its feedback play an important role in regulating the global radiation budget of the troposphere [*Held and Soden*, 2000] and the stratosphere [e.g., *Forster and Shine*, 1999; *Solomon et al.*, 2010; *Dessler et al.*, 2013].

The UTLS influx of H_2O is largely determined by the large-scale troposphere-to-stratosphere transport, during which air is essentially dehydrated in a transition region called the tropical tropopause layer (TTL) [e.g., *Sherwood and Dessler*, 2000; *Fueglistaler et al.*, 2009a]. Within the TTL the cold tropopause acts like a "cold trap" to freeze and dry air passing through it to the region's local saturation mixing ratio [*Brewer*, 1949]. Observations such as the entry mixing ratios [*Dessler*, 1998], the coherent relations between H_2O and temperature [*Mote et al.*, 1996], and the extensive cirrus clouds near the tropopause [e.g., *Winker and Trepte*, 1998; *Wang and Dessler*, 2012] all support this theory.

Fig. 1.2 shows the zonal mean H_2O distributions observed from the Microwave Limb Sounder (MLS) onboard the Aura Satellite [*Waters et al.*, 2006; *Read et al.*, 2007]. As shown, H_2O is limited in the stratosphere but abundant in the troposphere (this distinct feature of the abundances of H_2O was also used to identify TTL cirrus of convective origin [*Wang and Dessler*, 2012]). As explained, the 380-K isentrope (thick dashed line in Fig. 1.2) and above is the stratospheric overworld, where air is extremely dry and H_2O never exceeds 8 ppmv. The lowermost stratospheric air is enclosed by the 380-K isentrope and the PV based tropopause (2-PVU, thick grey lines in Fig. 1.2), where air is frequently exchanged between the troposphere and the stratosphere, resulting in H_2O ranges from as low as 3 ppmv to a few hundred ppmv. Fig. 1.2 also reveals strong horizontal and vertical gradients of H_2O across the upper troposphere and tropopause.

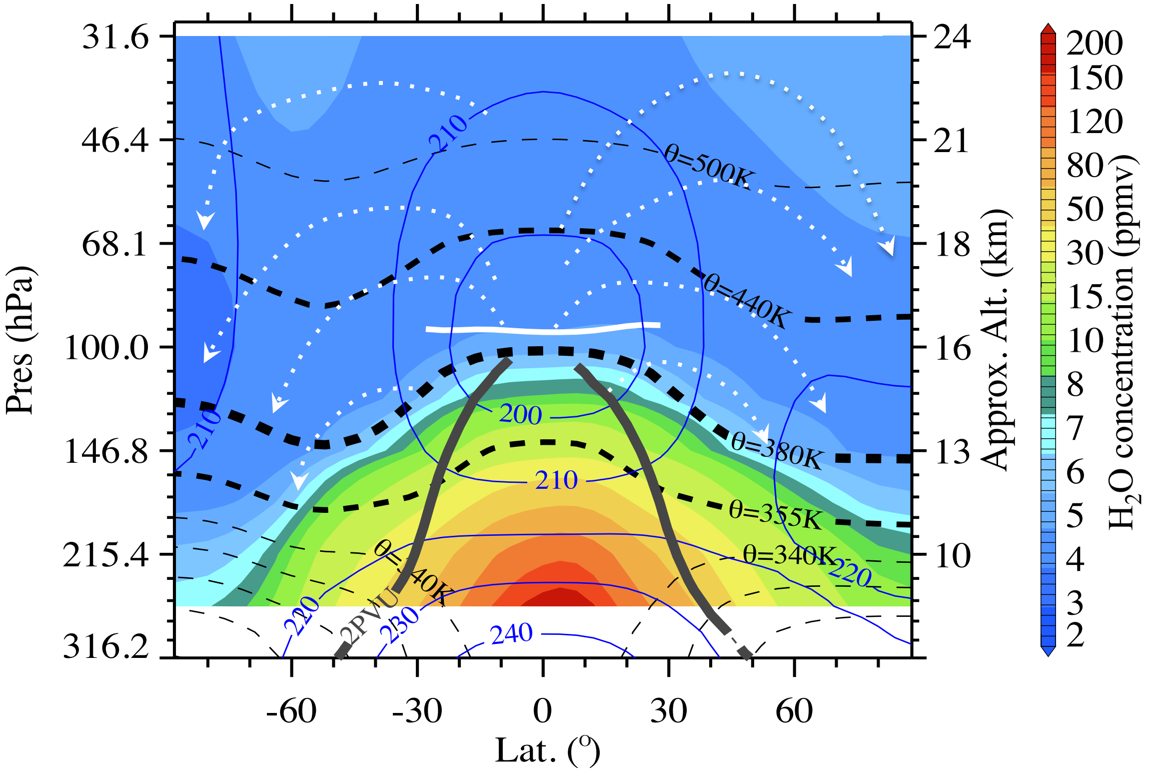

Figure 1.2. MLS observations of zonal mean H_2O mixing ratio in the UTLS, averaged over 2005-2011. Blue solid contours are temperature; black dash lines are the potential temperature, with 380-K highlighted thicker, separates the "overworld" from the "middle" world air [*Holton et al.*, 1995]; dotted white arrows indicate the Brew-Dobson Circulation. The 355-400 K isentropes enclosed in the tropical region defines the Tropical Tropopause Layer (TTL). The level of zero net radiative heating is around the 355-K isentrope. The white line over tropics at ~17 km indicates the cold-point tropopause (CPT), where the temperature is coldest.

In the stratosphere, two sources are believed to contribute to the H_2O abundances: in situ oxidation of methane (CH_4) in the upper stratosphere and direct transport from the troposphere. We know that stratospheric dynamics are dominated by the wave-driven Brewer-Dobson circulation [*Brewer*, 1949], which transports air from the troposphere across the tropopause into the lower stratosphere, followed by poleward flow at middle latitudes and downward flow at higher latitudes (blue arrows in Fig. 1.1).

Observations show that stratospheric H_2O has been increasing by ~0.05 ppmv/year over the past 50 years [*Oltmans and Hofmann*, 1995; *Evans et al.*, 1998; *Oltmans et al.*, 2000; *Rosenlof et al.*, 2001]. A recent analysis pointed out that the observed increase in tropospheric methane concentrations can only account for ~50% of the increased stratospheric H_2O, which means that the other half of the increase could only be explained by increases in the direct transport from the tropical troposphere to the stratosphere.

The TTL temperature primarily controls the amount of H_2O that is directly transported from the troposphere [*Brewer*, 1949]. In other words, the increased H_2O from transport should have been coincident with an increase in the tropopause temperature. However, radiosonde measurements show that the tropical tropopause has actually cooled off at ~0.5 K/decade [*Seidel et al.*, 2001; *Zhou et al.*, 2001], which makes it contrary to what would be required to explain the observed increase in stratospheric H_2O.

The above has shown that the dehydration processes are complex and cannot be understood from mean tropical tropopause temperatures alone. In fact, stratospheric water is not solely controlled by the temperature but also by the transport processes (different paths in different time-scales). Understanding this is one of the major objectives of our study, and will be discussed in detail in Sect. 3.

Besides the slow large-scale upwelling branch of the Brewer-Dobson circulation, a fast transport of air from the troposphere into the stratosphere via deep tropical convection – so-called convective overshooting, can lead to subsequent anvil formation, and then hydrates the UTLS [e.g., *Kley et al.*, 2000; *Sherwood and Dessler,* 2000; *Dessler*, 2002). While theories of this process exist, there is currently not enough data to validate or quantify this path with certainty.

1.2.2 O_3 and CO in the UTLS

Ozone (O_3) in the upper troposphere/lower stratosphere (UTLS) is an important constituent of the climate system, and has revealed trend changes in the last few decades that are only partly understood [*Schnadt Poberaj et al.*, 2009]. O_3 abundances in the UTLS vary in a wide dynamic range (~10's of ppbv to a few ppmv), and are influenced by a variety of chemical and dynamical processes, including photochemical production and loss and large- to small-scale transport (for example, deep convective lofting of boundary layer low O_3 air to the upper troposphere, e.g. *Folkins et al.,* 2002).

O_3 is radiatively important in our climate system. The global average radiative forcing of ozone is estimated to be between $0.25 - 0.65$ Wm^{-2} [*Forster et al.*, 2007], with the majority of this forcing coming from O_3 changes at the tropopause [*Lacis et al.*, 1990; *Forster and Shine*, 1997]. O_3 is therefore one of the most important greenhouse gases along with H_2O, CO_2, and CH_4.

The other important tracer in the UTLS – Carbon monoxide (CO), is produced near the Earth's surface from the oxidation of hydrocarbons (primarily isoprene and methane) and through combustion processes such as fossil fuel and biomass burning. Its concentration is highly variable in the troposphere, ranging between 50 and 100 ppbv in uncontaminated air and increasing to at least 500 ppbv in urban or biomass-burning plumes [*Sachse et al.*, 1988; *Barnes et al.*, 2003].

CO has a photochemical lifetime of months, which is at least as long as the time scale for many of the dynamical problems of interests. This makes it a useful tracer to diagnose horizontal and vertical transport in the UTLS [e.g., *Kar et al.*, 2004; *Huang et al.*, 2012] and to infer large-scale mesospheric circulations [*Clancy et al.*, 1984;

Minschwaner et al., 2010] and vertical motions in the stratosphere and mesosphere [*Allen et al.*, 2000; *Forkmann et al.*, 2005].

Unlike H_2O, CO is insoluble and immune from the dehydration processes, which makes it distinct in understanding the driving mechanisms behind H_2O in the UTLS. Similar to the gradual upward propagation of H_2O in the stratosphere – the so-called "tape recorder" signal [*Mote et al.*, 1996] (see also Sect. 3), subsequent observations from the Aura Microwave Limb Sounder (MLS) have shown a corresponding CO ''tape recorder'' [*Schoeberl et al.*, 2006].

In the UTLS, both O_3 and CO experience drastic changes. Figure 1.3 shows the zonal mean O_3 and CO distribution in tropopause coordinates, scaled with the seasonal mean tropopause height. The distributions reveal strong horizontal and vertical tracer gradients across the tropopause in both species. O_3 increases away from the tropopause in the lower stratosphere, and is low (and well-mixed) in the troposphere. The opposite behavior is seen for CO (high in the troposphere, low in the stratosphere), with higher CO concentrations in the Northern Hemisphere consistent with stronger anthropogenic sources and a ~2 month tropospheric lifetime.

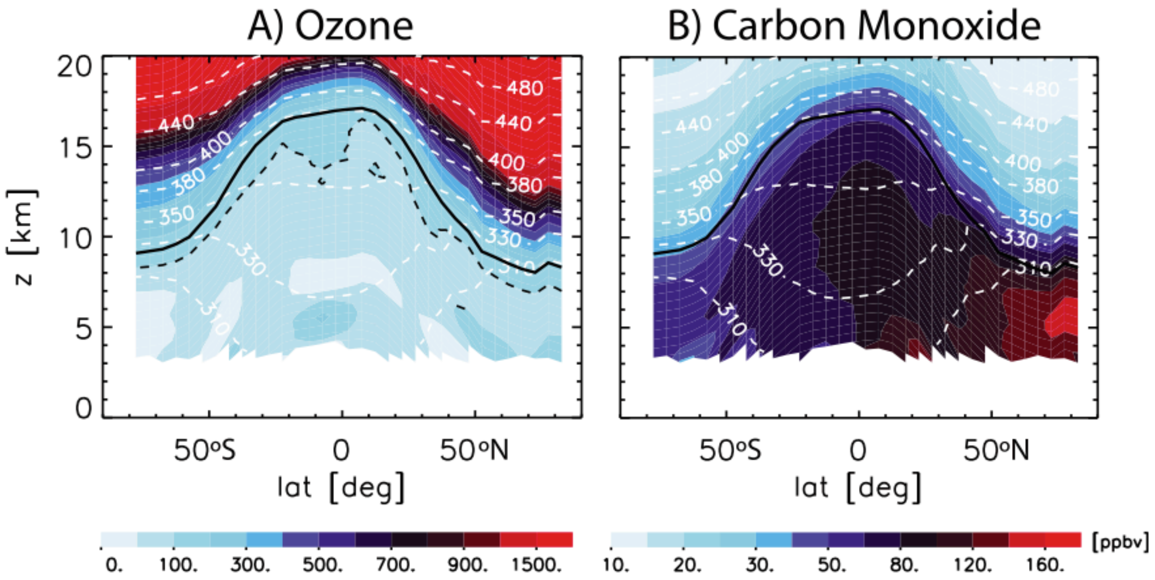

Figure 1.3. Zonal mean DJF (a) O_3 and (b) CO distribution from ACE-FTS satellite from 2004–2008 in tropopause coordinates scaled by the seasonal mean tropopause height. The thermal tropopause is the thick black line. The dashed black line in Figure 1.3a indicates the 100 ppbv ozone contour. Courtesy of *Gettelman et al.*, [2011].

The strong vertical gradients of species reflect the large contrasts of their stratospheric vs. tropospheric sources and sinks [e.g., *Gettelman et al.*, 2011]. Therefore, O_3 is generally considered a stratospheric tracer and H_2O and CO are referred as tropospheric tracers. A stratospheric tracer is a tracer with large stratospheric sources and much lower concentration and smaller variability in the troposphere, while a tropospheric tracer has higher concentrations and larger variability in the troposphere. Thus, a pair of tropospheric-stratospheric tracers (O_3 vs. H_2O, or O_3 vs. CO) can be used to identify the chemical tropopause or transport barrier as shown in Fig. 1.4 [e.g., *Fischer et al.*, 2000; *Pan et al.*, 2004, 2013].

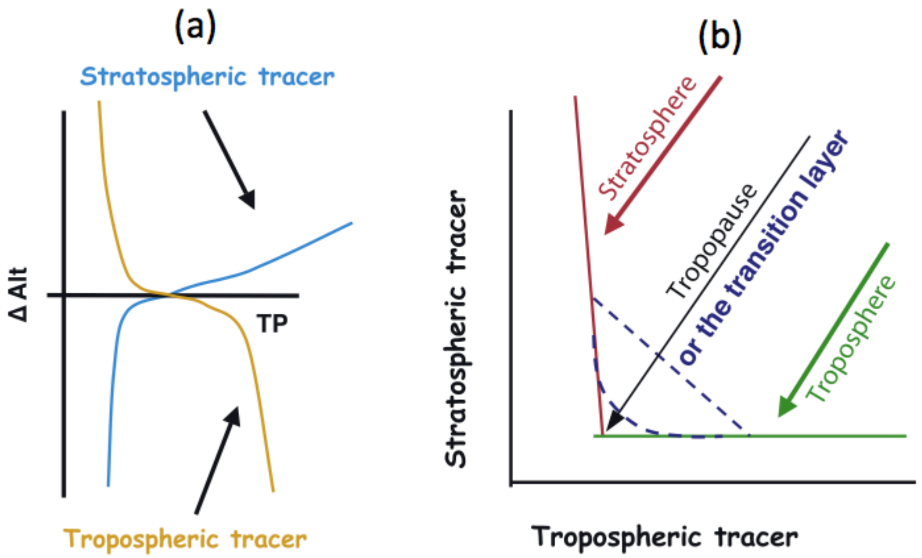

Figure 1.4. Schematic illustrating the tracer relationships: (a) stratospheric tracer and a tropospheric tracer in altitude space and (b) their relations in tracer-tracer space. Adapted from *Pan et al.*, [2004].

1.3 Motivation: Science Questions Addressable in Lagrangian Model

1.3.1 Lagrangian Studies of the Transport

The UTLS is strongly coupled to radiation, dynamics, and chemistry, dominated by trace gases such as H_2O and O_3, as well as aerosols and clouds. H_2O is the main source of cooling in the upper troposphere, whereas O_3 is the main source of warming in the lower stratosphere. Because of the low (background) temperature in the UTLS, radiative forcing is especially sensitive to the distribution of H_2O and O_3, i.e., small changes in tracer concentrations could result in relatively large changes in ratiation. Thus, perturbations to the distributions of H_2O and O_3 in the UTLS could potentially lead to direct forcing in the temperature structure, and hence changes to the atmospheric radiation, transport, and clouds, etc. In turn, those changes exert a strong impact back on the chemical composition (such as CO) and the dynamical structure of the UTLS. Such processes, on a wide range of length and time scales, constitute a feedback mechanism, which makes the climate system and the UTLS region (in particular), more complicated.

The above tells us that the most important aspect of H_2O, O_3, and CO in UTLS region is the transport process. Currently, global remote sensing from operational or research satellite platforms are unable to make accurate height-resolved measurements in the UTLS region. In situ measurements in the UTLS also suffer from a lack of global coverage. Model simulations, however, do not suffer from these limitations, and it is why we decided to study those tracer transport behaviors in the UTLS from a model perspective.

Model study of transport processes can be understood by either performing Lagrangian trajectory calculations, which track the movement of massless parcels in their moving frame of reference, or by observing fixed regions of space, i.e., the Eulerian perspective. The Eulerian perspective provides a continuous snapshot of observed field, which is common in the general circulation models (GCMs). However, when examining a particular mass of air, questions such as the historical or subsequent motion, or whether the air mass retains its identity, cannot be answered in a Eulerian framework. Therefore, in this study we focus on a Lagrangian model simulations of those tracers. The Lagrangian method is especially useful in studying the transport processes because it retains the full history of each ensemble, which allows us to tell when, where, and how much of chemical species transported. Moreover, with the full history of ensembles we could easily trace backward/forward to learn the parcels' history/future evolutions.

The Lagrangian method has been used in atmospheric studies for many years. Examples of applying the Lagrangian method ranges from micrometeorological to global scales, which include tracking the ash clouds produced by volcanic eruptions [*Webster et al*. 2012], predicting the transport of radioactive materials released following the accidents at the Fukushima nuclear power station in Japan [*Stohl et al*. 2012], examining the exchange of H_2O and O_3 between the troposphere and stratosphere [*Homeyer et al.*, 2011], modeling the atmospheric component in the global carbon cycle [*Lin et al*. 2004), and studying the water vapor transport and global dehydration patterns in the UTLS [*Fueglistaler et al.*, 2005; *Schoeberl and Dessler*, 2011; *Schoeberl et al.*, 2012, 2013].

Lagrangian studies also have several advantages over Eulerian calculations. They are often computationally less expensive at equivalent resolution and not subject to numerical diffusion, which is common to Eulerian models. It is this non-diffusive calculation in the Lagrangian framework that makes it especially accurate in regions where there are strong tracer gradients. For example, a Lagrangian calculation is most useful at the edge of the polar vortex or the tropopause, where sharp changes of chemical concentrations provide physical evidence of minimum mixing. The other important feature of Lagrangian model is that it could have "unlimited" resolution in both space and time. This is because the integration time step could be as small as an hour or less (assuming an accurate circulation available in at least 6-hourlyly manner), and the transport follows various paths in space.

Most UTLS trajectory studies have relied on back-trajectory calculations, in which parcels initiated in the lower stratosphere are advected backwards for a few months and only those that reach the upper troposphere are then analyzed to determine the details of mass transport, dehydration, or chemistry. In our studies, however, we use forward trajectory calculations, which allow a longer integration period (currently we use

~15 years) and are more straightforward in understanding parcel movements (as they follow the winds), thereby providing continuous evolutions of stratospheric constituents. Furthermore, it also provides diagnosis of stratospheric air age-spectra [*Schoeberl et al.*, 2003]. Refer to Sect. 2 for more details.

1.3.2 Science Questions to Be Addressed

In Sect. 2 we will see that the fundamental factor that affect the trajectory modeling results is the input winds used since they drive parcel movements. Therefore, accurate winds, especially vertical velocities, are fundamental to successful trajectory transport studies. In our work, we use winds from three state-of-the-art reanalyses (MERRA, ERA interim, and CFSR, see Chap 2.), because they exhibit different features in transport represented in current assimilation systems. Using three reanalyses winds enable us to 1) diagnose the importance of circulation, particularly vertical upwelling, to the tracer distribution, annual cycles, and variability around the UTLS; and 2) indirectly imply advantages and flaws in different assimilation systems. Those can be found in our model results because those "inert" tracers have lifetime as long as a few months (for CO) to years (for H_2O and O_3), and their concentrations and distributions rely directly on the uncertainties inherent in circulations. This comparison will be covered in both Sect. 3 (sensitivity to H_2O simulation) and Sect. 4 (sensitivity to O_3 and CO simulations).

In addition to winds, temperatures are also important for our simulation. For modeling H_2O, along the trajectories air parcels went through dehydration constrained by temperature of air. Thus, precise temperature (especially temperature at the tropopause) is also of vital importance [*Brewer*, 1949; *Dessler*, 1998]. Then it comes to the question of how well the tropopause temperature is represented in reanalyses, which have only limited discrete levels (vertical) around the tropopause. In Sect. 3 we will see that none of the reanalyses are able to resolve the very fine curvature feature of tropopause temperature. That means that the parcel dehydrations are uniformly limited to reanalyses vertical levels and therefore are questionable, although the H_2O field is well reproduced. Therefore, our questions are 1) what are the true dehydration patterns in the UTLS, and 2) will it be a huge matter in using reanalyses temperature field since H_2O field is already well simulated?

To tackle this problem we have included trajectory run controlled by GPS instead of reanalysis temperaturea (see Sect. 3). The GPS temperatures have very fine vertical resolution (~200 m) and it practically captures the fine structures of tropopause temperature. In Sect. 3 we will show that trajectory model runs controlled by GPS temperatures yield realistic dehydration patterns in the UTLS while producing similar H_2O field. This also tells us that reanalysis temperature in model native levels are already good enough for this kind of study. The advantage of reanalysis temperature over GPS temperature is its long records, which makes a long-term prediction possible.

For modeling O_3 and CO, chemical production and loss rates from a fully coupled climate-chemistry model are used. These simple parameters represent the net effects of chemical sources and sinks behind the complicated chemical reactions and cycles. We will see that driven by reanalyses winds, this simple parameterization of chemistry is able to simulate both O_3 and CO transport in the UTLS very well (compared to satellite observations). Other than that, because our trajectory model does not include mixing until the very last step when we grid the results, hence, the results are pure Lagrangian and it could offer us an understanding of whether the in-mixing is important in the tropical tropopause where chemical gradients are the greatest. This was inspired from another trajectory study performed by *Konopka et al*. [2009, 2010] and *Ploeger et al*. [2012], in which they added inexplicitly an in-mixing scheme when performing the Lagrangian study. Their results show that horizontal in-mixing from the mid-latitude to the tropics dominates the tracer variability around the tropopause. Moreover, both *Randel et al*. [2002, 2007] and *Abalos et al*. [2012] show from Eulerian perspective that tropical upwelling is the main driver of the chemical annual cycle above the tropical tropopause. All those has come to a debate as to the importance of whether in-mixing or upwelling dominates the tracer variability around the tropopause (where chemical vertical gradients are the greatest) based on Eulerian (*Randel et al*. [2002, 2007]; *Abalos et al*. [2012]), semi-Lagrangian (*Konopka et al*. [2009, 2010]; *Ploeger et al*. [2012]), and pure Lagrangian (*Wang et al.*, [2014]) perspectives. Our results therefore are important because it potentially ends the debate and provides us direct evidence of the importance of upwelling. More details will be discussed in Sect. 4.

1.3.3 Concluding Remarks

Trajectory models have been widely used for simulating H_2O [e.g., *Fueglistaler et al.*, 2005; *Liu et al.*, 2010; *Schoeberl and Dessler*, 2011; *Schoeberl et al.*, 2012, 2013], which is uniquely insensitive to the complexity of TTL processes because it is primarily the minimum temperature that controls it. Hence, trajectory modeling of O_3 and CO can provide complementary information to the H_2O simulations because it serves as a useful test for simplified understanding of transport and chemical processes in the UTLS. In addition to testing circulation and transport within the trajectory model, the O_3 and CO simulations can elucidate the mechanisms leading to observed chemical behavior, including transport history and pathways, seasonal and interannual variations, and relation to the stratospheric age-of-air [*Waugh and Hall*, 2002]. Furthermore, O_3 and CO exhibit relatively large out-of-phase seasonal cycles in the tropical lower stratosphere [*Randel et al.*, 2007], and these coupled variations provide a sensitive test of the trajectory model performances in this region.

In summary, H_2O, CO, and O_3 are complementary tracers representing primarily tropospheric and stratospheric sources. Those tracers exhibit strong gradients and variability across the tropopause transition layer. The trajectory modeling of these tracers enables us, for the first time, to track the full histories of chemical evolution within air parcels simultaneously, and it provides us an unprecedented understanding of transport and chemical behavior in the UTLS.

1.4 Outline of Dissertation

The outline of this dissertation is organized as follows. In Sect. 2 we introduce the trajectory model and the input data, as well as the datasets that are used to verify the model results. Sect. 3 focuses on trajectory modeling of UTLS water vapor (H_2O) using different reanalyses. The comparisons among them demonstrate the importance of winds and temperatures regarding the regulation of H_2O. Two co-authored papers have been published from the contents of this section [*Schoeberl et al.*, 2012, 2013]. A further discussion concerning the effect of using GPS temperature on dehydration in very fine vertical resolution is included in the second part of this section, which is under preparation to be submitted to JGR. In Sect. 4 we first briefly review the UTLS chemistry (related to O_3 and CO) and how they are represented in a Eulerian climate-chemistry model. Then the trajectory modeling of O_3 and CO based on the imposed chemistry is shown in detail, with further discussion of the dominating factors that control tracer seasonal cycles and interannual variability. The contents of this section have been submitted to ACP, currently in public discussion. In Sect. 5 the conclusions are summarized and the outlines for future work are sketched, including diagnosing tracer transport in the lowermost stratosphere and summertime Asian Monsoon region, modeling TTL cirrus formation, and exploring H_2O enhancement during North American Monsoon.

2. TRAJECTORY MODEL, INPUT DATA, AND VERIFYING DATASETS

The trajectory model is performed in Lagrangian framework, in which each ensemble of parcel is treated massless and dimensionless and moves independently following winds. This perspective is proved to be very useful in studying the transport process in the atmosphere, especially around the UTLS region where tracer vertical gradients are the greatest and less mixing occurring. In this section we will discuss the basic concept of trajectory models and illustrates how our trajectory model is different from others'. We also include a section talking about the trajectory input data and evaluating datasets we will use in this study.

2.1 Lagrangian Trajectory Overview

Two methods are widely used to observe and analyze fluid flows: observing the flow velocity at fixed positions, which yields an Eulerian representation, and observing the trajectories of specific parcels, which yields a Lagrangian representation.

In the Eulerian system, the time derivatives of parcel can be expressed as

$$D[]/Dt = \partial[]/\partial t + \vec{\boldsymbol{V}} \cdot \nabla[] \qquad (2.1)$$

where [] is the arbitrary and fixed position in a fixed framework, and $\partial[]/\partial t$ is the local change at this position. $\vec{\boldsymbol{V}} \cdot \nabla[]$ is usually called the advection term, which represents the transport of flow at a definite rate and direction, so that parcel trajectories are the characteristics of the advection equation. Eq. (2.1) is also called the material derivative.

The time rate of change observed on a flowing parcel can be expressed as

$$D[]/Dt = \partial[]/\partial t \qquad (2.2)$$

in the Lagrangian system. Here, [] is the position of a moving parcel, i.e., the frame of reference that moves relatively to the fixed coordinate. The Advection term vanishes because particle motions are implicitly hinted by the flow. Combined with Eq. (1) we see that the material derivative at a given position is equal to the Lagrangian time rate of change of the particle present at that position.

Lagrangian methods are often the most efficient way to sample a flow. Furthermore, physical conservation laws are inherently Lagrangian since they apply to moving flows, rather than to the flow that happens to be present at some fixed point in space, i.e., the Eulerian point of view. As opposed to the Eulerian models, Lagrangian models produce non-diffusive transport and thus are especially accurate in regions where there are strong tracer gradients (e.g., the edge of the polar vortex, the tropopause). In Lagrangian models, both forward and backward trajectory calculations retain the history of the parcel, which is difficult to determine in Eulerian models.

The Lagrangian model computes the trajectories of air parcels given the locally instantaneous Eulerian velocity field, i.e.,

$$\boldsymbol{d}\vec{\boldsymbol{x}}(t)/dt = \vec{\boldsymbol{v}}(\vec{\boldsymbol{x}}, t),\ \vec{\boldsymbol{x}}(t=0) = \vec{\boldsymbol{x}}_{\boldsymbol{0}} \qquad (2.3)$$

Here, $\vec{\boldsymbol{x}}(t)$ is the position of a massless air parcel, which is sufficiently small that all particles within it are transported by the flow with the same velocity $\vec{\boldsymbol{v}}(\vec{\boldsymbol{x}}, t)$, but also large enough that it contains statistically representative ensembles; $\vec{\boldsymbol{x}}_{\boldsymbol{0}}$ is the initial position of the parcel. Given a velocity field $\vec{\boldsymbol{v}}$, the solution to Eq. (2.3) is the path (trajectory) of air parcel travelling to (forward in time) or from (backward in time). Depending on wind fields, the trajectory can be computed diagnostically using archived winds, or prognostically using forecast winds.

Over the years, different types of trajectory models have been developed in studying the dynamic and chemical aspects of the atmosphere. Those trajectory models and their accuracy and characteristics are summarized in *Stohl* [1998] and *Bowman et al.* [2013]. The numerical solver for those trajectory models generally follows the same procedures: 1) interpolate the velocity filed to the current positions of parcels in space and time; and 2) use a numerical scheme to integrate Eq. (2.3) backward or forward in time given the initial conditions and the interpolated velocities.

The precision of trajectory calculations can be attributed to the choice of numerical integration scheme, uncertainties in the wind field, or sampling errors. Examples of such errors include, respectively, truncation errors, wind measurement errors, and errors arising from poor spatial or temporal resolution.

2.2 Domain-Filling, Forward Diabatic Trajectory

2.2.1 Introduction to TRAJ3D

In our work we use Dr. Kenneth Bowman's trajectory code (TRAJ3D, *Bowman* [1993]; *Bowman and Carrie* [2002]) to calculate the paths of parcels. TRAJ3D was developed in **I**nteractive **D**ata **L**anguage (IDL). It uses 4-D linear interpolation on velocities and a standard fourth-order Runge-Kutta scheme with 32 time steps per day (45 minutes interval) to integrate Eq. (2.3). This is commonly used in trajectory calculations since it is fourth-order accurate in time. The implementation of fourth-order Runge-Kutta involves evaluation of the velocity $\vec{\boldsymbol{v}}$ at four points for each time step. Assuming a time step size δt, define:

$$\vec{\boldsymbol{x}}_{n+1} = \vec{\boldsymbol{x}}_n + \frac{\mathbf{1}}{\mathbf{6}}(\boldsymbol{k}_1 + 2\boldsymbol{k}_2 + 2\boldsymbol{k}_3 + \boldsymbol{k}_4) \qquad (2.4)$$

So value $\vec{\boldsymbol{x}}_{n+1}$ at time $t_{n+1}$is calculated from $\vec{\boldsymbol{x}}_n$ at time t_n for n=0, 1, 2, 3, …, using

$$\begin{aligned}
\boldsymbol{k_1} &= \vec{\boldsymbol{v}}(t_n, \vec{\boldsymbol{x}}_n) \\
\boldsymbol{k_2} &= \vec{\boldsymbol{v}}\left(t_n + \tfrac{1}{2}\delta t, \vec{\boldsymbol{x}}_n + \tfrac{\delta t}{2}\boldsymbol{k_1}\right) \qquad (2.5) \\
\boldsymbol{k_3} &= \vec{\boldsymbol{v}}\left(t_n + \tfrac{\boldsymbol{1}}{\boldsymbol{2}}\delta t, \vec{\boldsymbol{x}}_n + \tfrac{\delta t}{\boldsymbol{2}}\boldsymbol{k_2}\right) \\
\boldsymbol{k_4} &= \vec{\boldsymbol{v}}(t_n + \delta t, \vec{\boldsymbol{x}}_n + \delta t\boldsymbol{k_3})
\end{aligned}$$

Here, we express each step with vector notation to represent the 3-D integration. During the integration, $\boldsymbol{k_1}$ is the increment based on the slope at the beginning of the interval, $\boldsymbol{k_2}$ is the increment based on the slope of $\boldsymbol{k_1}$ at the midpoint of the interval, and $\boldsymbol{k_3}$ is again the increment based on the slope of $\boldsymbol{k_2}$ at midpoint, and $\boldsymbol{k_4}$ is the increment based on the slope at the end of the interval. This process repeats for each time step.

TRAJ3D uses an integrator time-step of $\delta t = 45\, min$, which is much smaller than the interval of wind fields (6-hourly or daily). The precision of this numerical scheme is evaluated by comparing errors due to integration (from varying time step sizes) and errors due to wind fields (by adding 1% noise to the wind fields), which suggest that errors in winds, rather than truncation errors in the numerical scheme, dominate the errors in trajectory calculations [*Bowman*, 1993].

2.2.2 Vertical Coordinate and Vertical Velocity

Of particular interest in trajectory calculations is how the vertical velocity fields are represented (horizontal winds). Vertical velocity in pressure (isobaric) coordinates is pressure tendency (dp/dt=**ω** field), and vertical velocity in potential temperature (isentropic) coordinate is potential temperature tendency (*dθ/dt*). In pressure coordinates, parcels are advected along pressure surfaces by horizontal wind, and across pressure surfaces vertically. The vertical velocity field is derived through mass conservation via the continuity equation. Trajectory calculations performed in pressure coordinates are usually referred as ***kinematic*** runs.

In potential temperature (isentropic) coordinates, parcels are advected along constant potential temperature surfaces (isentropes) by the large-scale wind and across isentropic surfaces by the net diabatic heating, which are produced from the release of latent heating during condensation/deposition, the absorption of solar and infrared radiation, the heating by diffusion, and frictional dissipation, etc. Trajectories calculated in isentropic coordinates are referred to as ***diabatic*** runs. In cases that diabatic heating is zero, trajectories are constrained on isentropic surfaces and known as isentropic trajectories [e.g., *Danielsen*, 1961]. Given this, diabatic trajectories are also called "quasi-isentropic" trajectories [*Schoeberl and Sparling*, 1995].

In the UTLS region, vertical motion is ~30 m/day (or ~1 K/day cross isentrope) – several orders of magnitude smaller than the horizontal motion (~1000 km/day). Therefore, the vertical velocity (**ω**) derived via mass continuity equation can be rather noisy in the event of even small errors in the horizontal wind. Besides, the underrepresented gravity drag or the under-sampled fast perturbations due to sampling could also results in noisy vertical wind [*Diallo et al.*, 2012]. As a result, 3-D kinematic runs show large vertical dispersion and parcels experience unrealistically movement [*Schoeberl et al.*, 2003; *Ploeger et al.*, 2010; *Schoeberl and Dessler*, 2011].

The noise in the vertical velocity field can be reduced in isentropic coordinates, where the vertical velocity is no longer pressure tendency (**ω**) but potential temperature tendency (*dθ/dt*), which is deduced from the diabatic heating rates via the First thermodynamic law [e.g., *Andrews et al.*, 1987]

$$d\theta/dt = Q\ (p_0/p)^{R/Cp} \qquad (4)$$

here Q is the diabatic heating rates in unit of K/s; p is pressure; p_0 is the reference pressure (usually 1000 hPa); Cp is the specific heat capacity at constant pressure, and R is the gas constant for air.

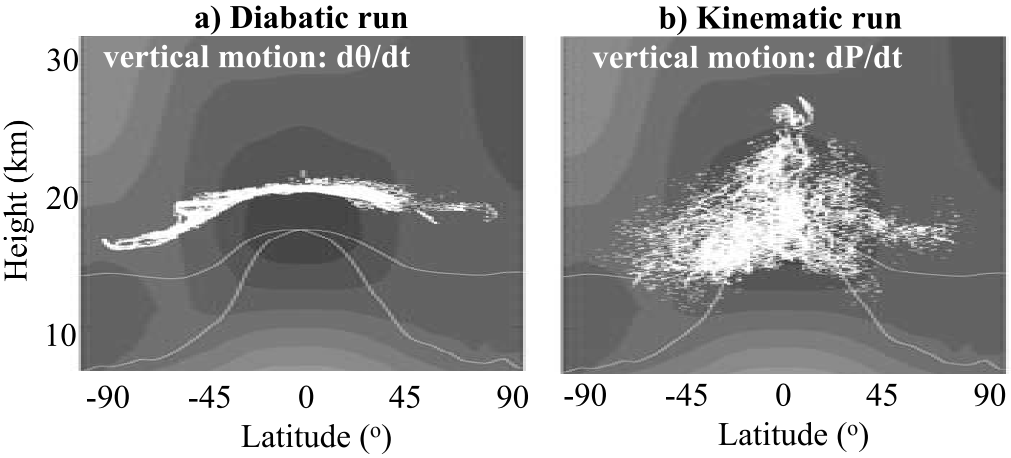

Figure 2.1. Distribution of parcels 50 days since the initiation at 20 km using back trajectory calculations from (a) diabatic run and (b) kinematic run. The wind and vertical velocity are from the Met. Office Data Assimilation System (UKMO). The lower (upper) thin white line shows the zonal mean tropopause (380 K isentrope). Zonal mean temperature is indicated by the gray scale contours and particles are shown as white dots. Adapted from *Schoeberl et al.*, [2003].

Figure 2.1 compares the impact on parcel distributions from trajectory calculations running on both isentropic (diabatic) or isobaric (kinematic) coordinates. The diabatic run yields less transport in the vertical, which is generally in better agreement with observations and theory. The kinematic run, however, results in large vertical dispersion due to noisy vertical velocity calculated from mass conservation. Therefore, in our study we perform diabatic run and noted that the diabatic velocities no longer satisfy mass continuity with the horizontal winds, which points to a self-limiting aspect of using diabatic winds in Eulerian calculations.

2.2.3 Forward vs. Backward

Of UTLS trajectory studies a predominant use is back-trajectory calculations, in which parcels are advected backwards for a few months to see if they encounter some predetermined criteria. For example, when studying stratosphere water vapor, parcels initiated at lower stratosphere (~20 km or ~440 K) are advected backwards, and only those reach to the upper troposphere will be analyzed to determine water vapor and its dehydration behavior. However, from age-of-air measurements a significant number of parcels in the lower tropical stratosphere may not be traceable back to the upper troposphere after a few months of back trajectory integration.

Compared with backward trajectories, forward-trajectories allow for longer integration period and are more straightforward in the diagnosis of age-spectra [*Schoeberl et al.*, 2003]. Forward integration provides a continuous picture of the time evolution of stratospheric constituents and allows us to investigate issues that may be difficult to address with backward trajectories. For example, in studying stratospheric water vapor back-trajectories usually disregard those parcels that cannot be traced back to the upper troposphere within a predetermined period, and thus the final parcels left are limited. On the other hand, back trajectory calculations are preferred for determining air parcel origins, in order to elucidate observations. Forward calculations, on the other hand, rely completely on the parcel movements. As time goes they will yield a statistically robust and unbiased representation of the trace gas fields. Therefore, our model runs forward, not backward.

2.2.4 Domain-Filling

The other feature about our trajectory modeling is the domain-filling strategy. The forward domain-filling model works as follows: an ensemble of parcels is initialized in the upper troposphere (typically 360-370 K isentrope) on an equal area grid that covers the tropics and mid-latitudes. The initialization altitude is selected to be just above the level of zero radiative heating in the tropics (~355-360 K), where parcels tend to ascend. Meanwhile, it is also typically below the tropical tropopause (~380 K), so parcels could go through essential dehydration when crossing the cold tropopause. It is this dehydration process that fixes the amount of water vapor, which makes the initial water vapor mixing ratio somewhat irrelevant (see Sect. 3 for details).

Parcels are advected forward for one day using reanalysis winds. At the end of the day, any parcels that have descended below a pre-determined altitude, usually 250-hPa, are removed since in most cases they have re-entered the troposphere. The upper boundary is chosen to be ~2200-K isentrope (~1 hPa or ~50 km) to cover the entire stratosphere. Parcels are initialized and added to the ensemble consecutively each day and the combined set of parcels is then run forward. This process is repeated over the entire integration period. As more and more parcels are injected into the model, the stratospheric domain is filled up with parcels – this is the concept of domain-filling used in our model.

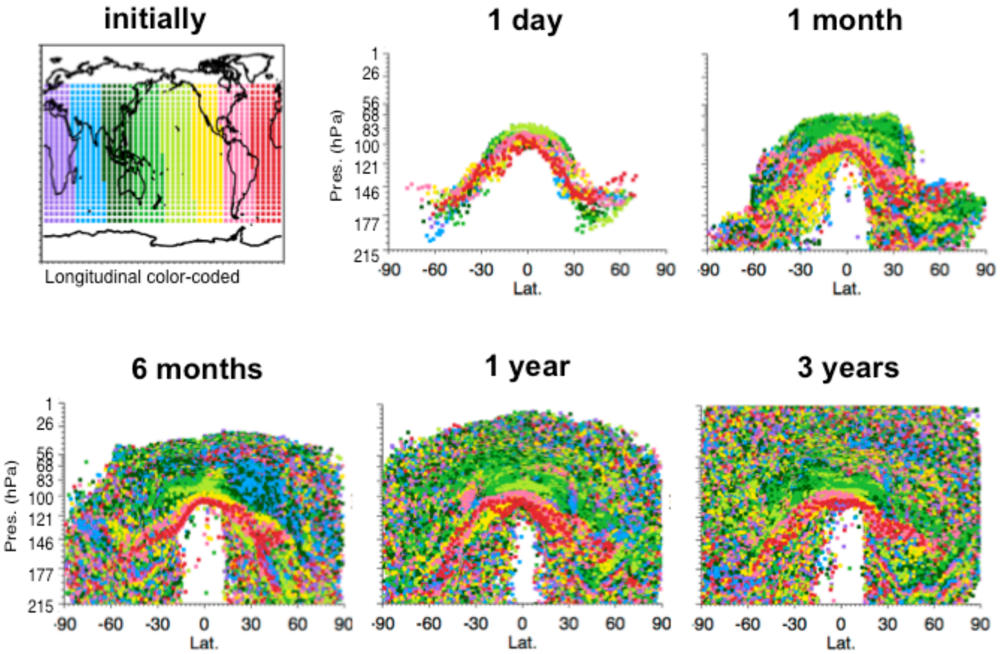

Figure 2.2. Demonstration of forward domain-filling trajectory. All parcels are longitudinally color-coded in initiation to show the regional differences of upward flow.

Figure 2.2 demonstrates the concept of domain-filling. We see that parcels gradually fill up the stratosphere domain after 1-2 years (the filling efficiency depends on the density of initiation grid). Parcels tend to cluster at lower altitudes where the vertical velocities (diabatic heating rates) are smaller. To highlight the regional differences of the ascending branch of the Brewer-Dobson circulation, all parcels are longitudinally color-coded in initiation. Due to the intense upward flow in the Tropical Western Pacific (TWP) region, parcels initiated here (green) tend to be pushed up higher than those started above the Atlantic Ocean (red).

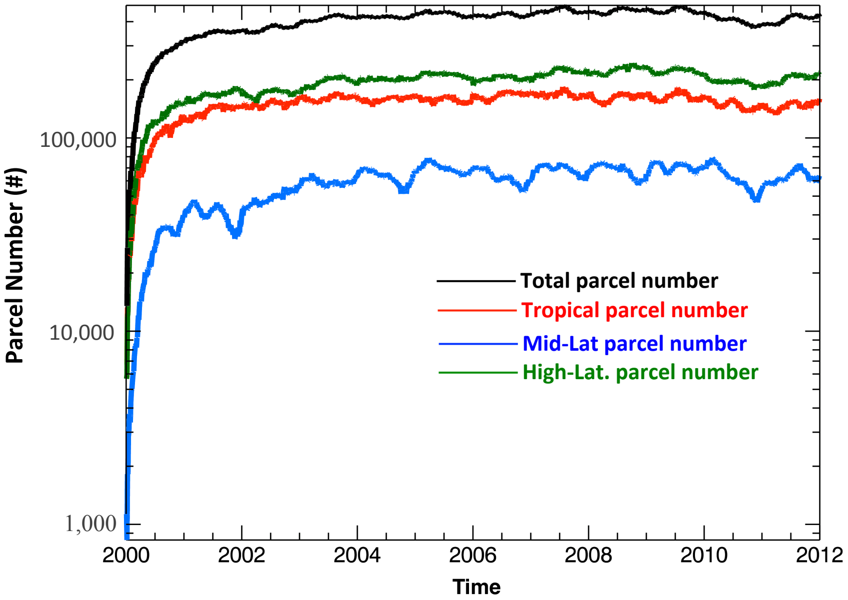

Figure 2.3. Parcel number statistics in tropical region (30^{o} N-S, red), mid-latitude region (30^{o}-60^{o} N-S, blue), high-latitude region (60^{o}-90^{o} N-S, green), and whole domain (black).

Figure 2.3 shows regional parcel statistics from a trajectory run starting from 2000 and integrated to the end of 2012. After 3-4 years the system is filled up with approximately 1 million parcels in the domain, reaching steady state with equal amount of parcels removed and injected in everyday. It is also worth mentioning that the parcel numbers are also steady in each latitudinal region, so our statistical results are robust with no regional biases.

2.2.5 Gravity Waves and Convection Moistening

Our model also includes parameterizations for gravity waves and convective injection of ice, both of which can be independently switched on or off (see *Schoeberl et al.*, 2011 for details). Briefly, the gravity wave parameterization scheme perturbs the parcels' temperature history to account for temperature fluctuations that are unresolved by the reanalyses. Our gravity wave scheme is loosely based on *Jensen and Pfister*

[2004] that modeled the effect of gravity waves and showed that they had the potential to reduce stratospheric water vapor by ~0.5 ppmv.

The convective scheme, which is based on *Dessler et al.* [2007], accounts for the rapid injection of water into the TTL by convective updrafts. This scheme first derive a spatial (horizontal) probability of convective influence as a function of pressure and the flux of outgoing longwave radiation (OLR) (*Liebmann and Smith*, [1996]), and then the measurements of height-resolved ice water content (IWC) from the Aura Microwave Limb Sounder (MLS) [*Waters et al.*, 2006] is used to determine vertical distribution of the probability. When convection impacts a parcel, we set the parcel's RH to 100 %. This means that sub-saturated parcels are hydrated and super-saturated parcels are dehydrated by convection [*Jensen et al.*, 2007].

The convection scheme can also be used to diagnose its impacts on chemical species. When convection hits a parcel, we set the parcel's O_3 and CO concentration characteristic of the boundary layer level, i.e., low O_3 (such as 0.1 ppmv) and high CO (150 ppbv), so that the resulting O_3 and CO tend to be lower and higher, respectively. Gravity wave fluctuations, however, affect only the temperature and then the H_2O, and in our model they have no impacts on chemical species.

Our work is designed to study the transport effects of tracers, which is purely dependent on the circulation and the chemistry imposed. Therefore, in this dissertation all results are from the trajectory model runs when parameterized gravity waves and convection schemes were switched off. This creates a relatively "uniform" environment when evaluating transport effects demonstrated by different tracers.

2.3 Trajectory Model Input

2.3.1 Reanalyses Input

As discussed in section 2.1, the trajectory model computes the paths of air parcels given Eulerian wind field. Depending on wind fields, the trajectory can be computed diagnostically using archived winds such as operational models or reanalyses, or prognostically using forecasting winds. For our purposes of study, the reanalyses datasets are chosen because they are combinations of model forecasts forced (corrected) by available observations, which provide high-quality analyses of the global 3-D state of the atmosphere.

The first successful operation of global reanalysis starting from 1948 was referred as NCEP/R1 [*Kalnay et al.*, 1996]. Over the last decade, the NCEP/R1 data have been widely used by the community, for which it has built the basis of historical and real time climate monitoring. More recently other notable reanalyses efforts were initiated by major operational centers around the world. They range from the ERA40 [*Uppala et al.*, 2005] by the ECMWF, the ECMWF ERA-interim reanalysis [*Dee et al.*, 2011], the JRA25 reanalysis [*Onogi et al.*, 2007] by the Japan Meteorological Agency (JMA), the Modern Era Retrospective-analysis for Research and Applications (MERRA) [*Rienecker et al.*, 2011] by the GSFC/NASA, the NCEP Climate Forecast System Reanalysis (CFSR) by NOAA [*Saha et al.*, 2010] by, and the ongoing JRA55 reanalysis.

Among those reanalyses we chose to use ERA-interim, NCEP CFSR, and MERRA because they provide relatively higher vertical resolution in the TTL region. MERRA is produced by NASA's Global Modeling and Assimilation Office (GMAO), covering the modern era of remotely sensed data from 1979 through the present. The primary focus of MERRA is to improve the assimilation of the hydrological cycle. Extensive 3D 3-hourly winds are available on 42 pressure levels at 1.25 degree resolution.

ERA-Interim (ERAi) is produced by the European Centre for Medium-Range Weather Forecasts (ECMWF) [*Dee et al.*, 2011]. ERAi uses a 12-houly 4D variational data assimilation cycle with 60 hybrid levels in the vertical from the surface to 0.1 hPa. Wind fields are extracted from the analysis available at 6-hourly interval (00:00 UT, 06:00 UT, 12:00 UT and 18:00UT).

CFSR was developed by the National Centers for Environmental Prediction (NCEP) as the first coupled atmosphere–ocean–land surface–sea ice reanalysis [*Saha et al.*, 2010]. CFSR technically only covers the period 1979–2009, but continuing output from the current (effectively identical) version of the Climate Forecast System model extends the CFSR data record to the present. CFSR reports winds 6-hourly at 00:00 UT, 06:00 UT, 12:00 UT and 18:00UT.

As mentioned in 2.2.2, our model operates on isentropic coordinates, in which the vertical wind is represented by diabatic heating rates (not pressure velocities). Therefore, we use diabatic heating rates instead of pressure velocity from the reanalyses to drive the parcels vertically. In addition to the wind that feeds the trajectory, we also use temperature to constrain the maximum abundances of water vapor in a parcel. Recall that temperature plays a crucial role in regulating water vapor (entering) into the stratosphere, therefore the accuracy of the temperature data directly affects the model results.

MERRA diabatic heating includes components of heating due to long-wave radiation, short-wave radiation, moist physics, turbulent vertical mixing, gravity wave drag, and friction. ERAi heating rates are obtained as temperature tendencies at 3 hour intervals from the twice-daily assimilation cycles starting at 00:00Z and 12:00Z. Hence they are available at 01:30Z, 04:30Z, 07:30Z, 10:30Z, 13:30Z, 16:30Z, 19:30Z and 22:30Z. ERAi diabatic heating rates include individual components of heating due to long-wave short-wave radiation and total heating rates. Heating due to moist physics is not reported separately and must be inferred as a residual [*Fueglistaler et al.,* 2009b]. In addition to total diabatic heating rates, CFSR provides heating rates due to long-wave radiation, short-wave radiation, deep convection, shallow convection, large-scale condensation, and vertical diffusion.

To summarize, we use horizontal winds (U, V) and diabatic heating rates (Q) available on either model native levels or standard pressure levels to drive the parcels. During the trajectory integration, we also use temperature (T) in the highest vertical resolution available to constrain parcel water vapor amount. Table 1 summarizes general features of those datasets.

Table 1: Summary of reanalyses datasets.

Original Reanalyses Datasets			**H (deg) (lon x lat)**	**nV (#)**	**nV (#) in TTL**	**Data Source**	**Description**
ERA interim 1979-present	Wind Component	U, V	1x1	60[1]	6	ei_an_ml	ei: ERA interim an: analysis ml: model hybrid levels[1]
		Q	1x1	60[1]	6	ei_an_ml	
	Temperature	T	1x1	60[1]	6	ei_an_ml	
NCEP CFSR 1979-2010	Wind Component	U, V	0.5x0.5[2]	37	5	pgb_h_nl	pgb: presure levels diab: diabatic heating rates h: high horizontal resolution (0.5x0.5) f: fine horizontal resolution (1x1) nl: analysis 06:6-hourly forecast
		Q	1x1	37	5	diab_f_06	
	Temperature	T	0.5x0.5	37	5	pgb_h_nl	
MERRA 1979-present	Wind Component	U, V	1.25x1.25	42	4	inst3_asm_Cp	inst: instantaneous; tavg: time average asm: assimilated state; tdt: temperature tendency; ana: direct analysis 3: 3-hourly; 6:6-hourly Cp: Reduced resolution on pressure levels Nv: Native resolution on model layers
		Q	1.25x1.25	42	4	tavg3_tdt_Cp	
	Temperature	T	2/3x1/2	72	8	inst6_ana_Nv	

[1]: These fields on hybrid levels will be interpolated to 60 standard pressure levels by using surface pressure data.

[2]: These wind component need to be re-gridded to the grid of diabatic heating rates.

It is obvious that different reanalyses datasets are provided with different resolutions temporally. For easy to use in our model, we homogenized all datasets in 6-hourly, while keeping their horizontal and vertical resolutions originally. For instance, we converted ERA interim data from hybrid sigma levels to 60 isobaric levels that correspond to the nominal pressure of the eta levels used in the forecast model (relative to a surface pressure of 1000 hPa), and we also sampled MERRA wind files from 3-hourly to 6-hourly at 00Z, 06Z, 12Z, and 18Z, and averaged MERRA diabatic heating rates every 6-hourly to be consistent with the wind fields. In addition, CFSR wind and temperature fields originally available on 0.5x0.5 degrees in longitude by latitude are interpolated into the same grids of diabatic heating rates (1x1 degrees).

After pre-processing, all reanalyses datasets are on pressure levels, and are ready to feed into the trajectory model. Figure 2.4 compares the vertical resolution of three reanalyses in pressure coordinate. The TTL region is magnified on right panel to highlight the different model levels implemented.

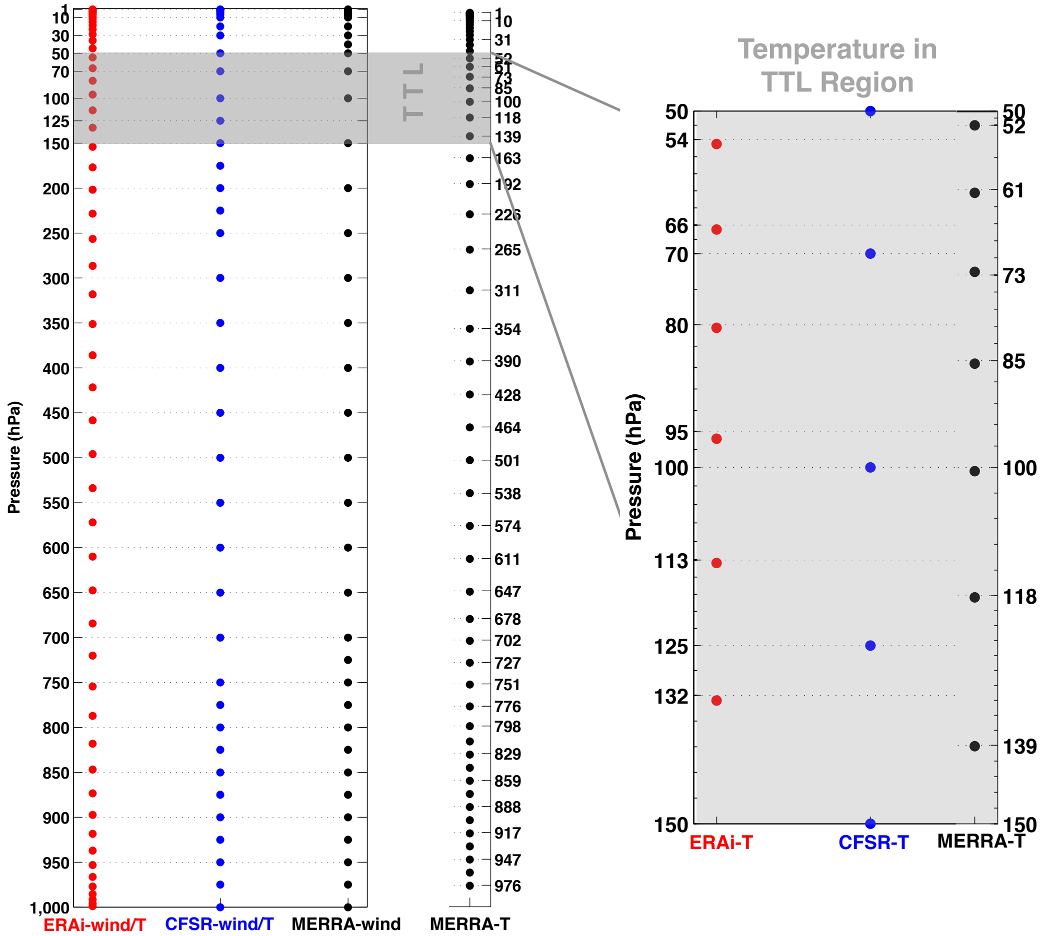

Figure 2.4. Vertical resolution of three analysis datasets. The TTL region is magnified in right panel to highlight the different resolutions in vertical.

Apparently, both MERRA and ERAi provide temperature with vertical resolutions of ~1 km in the TTL, while CFSR is slightly coarser. The performances of using three reanalyses are described in detail in Section 3, where we will see that high vertical resolution is essential for capturing the temperature minimum around the tropopause, which regulates the entry level of water vapor in the stratosphere.

The discrepencies in temperature and diabatic heating among three reanalyses, along with the simulated stratosphere H_2O produced will be addressed in detail in Sect. 3.

Here, in Fig. 2.5 and Fig. 2.6 we only briefly introduce the major differences that could have affected trajectory simulations.

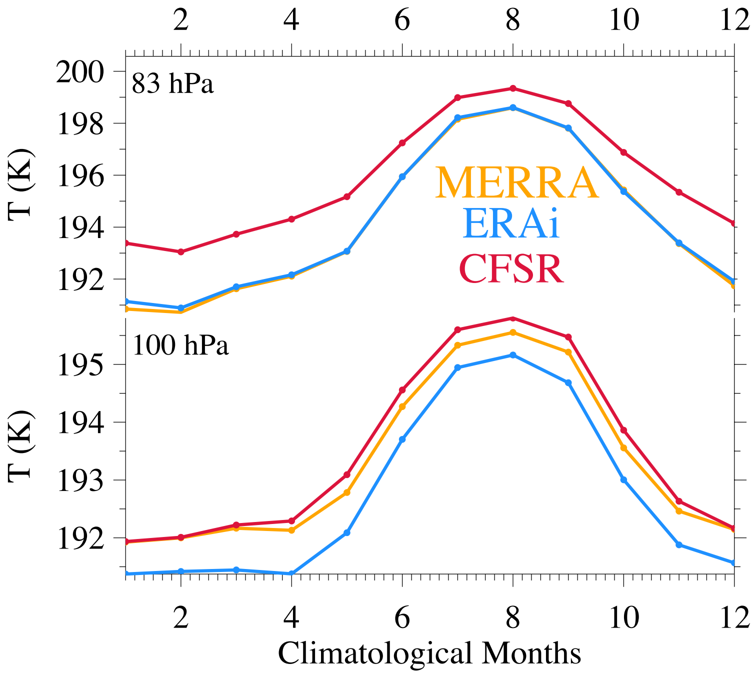

Figure 2.5. Climatological mean temperature at 100 and 83 hPa from MERRA (orange), ERAi (blue), and CFSR (red), averaged over deep tropics (15^o N-S) in 2001-2010.

Accurate temperature is critical for successful simulations of stratospheric H_2O because the entry-level value is governed by the Clausius-Clapeyron equation assuming saturation with respect to ice [*Fueglistaler et al.*, 2005; *Dessler et al.*, 2013]. Fig. 2.5 compares the climatological mean temperature at 100 and 83 hPa – the closest level to the cold-point tropopause, where air goes through essential dehydrations and then carries the correct entry-level of H_2O into the stratosphere. It shows that MERRA captures the key features of temperature in the UTLS, with the tropical minimum of 192-195 K around 100 hPa, in agreement with radiosonde observations [*Seidel et al.*, 2001]. ERAi, on the other hand, has a cold bias of at least 0.5 K and CFSR is ~0.2 K warmer. At 83 hPa, MERRA and ERAi temperature are quite close and CFSR shows a warmer bias of ~2 K during boreal winter-spring and ~1 K during summer-fall. As will be shown in Sec. 3, the cold and warm bias in ERAi and CFSR create a 0.7 ppmv lower and 1.1 ppmv higher bias in simulated water vapor around the tropopause, respectively.

Figure 2.6 compares the evolution of diabatic heating rates in the last decade averaged in the inner tropics (15° N-S). Here, diabatic heating (positive) indicates an upward mass flux across the isentropes, while diabatic cooling (negative) indicates a downward flux. The figure shows that upward motion prevails in the tropical region, which is the ascending branch of Brewer-Dobson circulation (see Fig. 1.1 and Fig. 3.1).

This figure also highlights the large differences in the simulated diabatic heat budget. For example, there is a close to zero heating, or even net diabatic cooling prevails throughout the tropics in MERRA around 150-120 hPa, indicating a deficit in MERRA's budget calculation. In trajectory calculations, parcels traveling to this region inevitably descend back to the troposphere so that no parcels initiated below this level could make it to the stratosphere (see Sect. 3), which is not the case for the real atmosphere. On the other hand, large heating exists in ERAi within the TTL (*Fueglistaler et al.*, 2009b) that could cause unrealistically strong upward motion and shorter transport timescales. See Sect. 3&4 for detailed discussions of the different diabatic heating that affects the vertical transport and residence time of H_2O and chemical species in the UTLS.

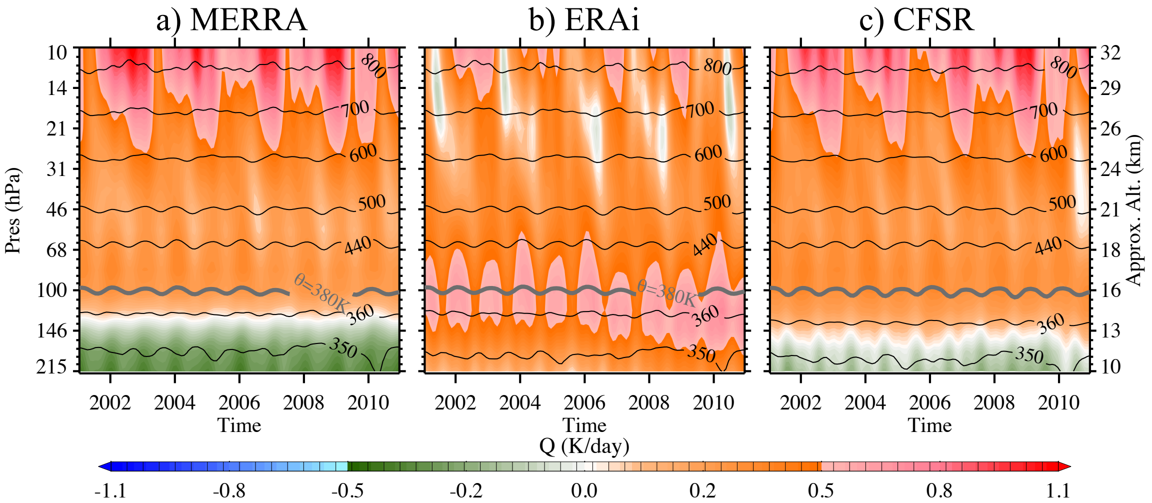

Figure 2.6. Vertical evolutions of diabatic heating rates among (a) MERRA, (b) ERAi, and (c) CFSR averaged over the last decade (2001-2010). In each panel, black lines label the potential temperature from each reanalysis; the 380-K isentrope is highlighted in thick grey line to approximate the tropopause that separates the overworld from the air below.

2.3.2 GPS Temperature Input

The reanalyses provide temperature with at most ~1 km vertical resolution around the tropopause. This resolution may not be fine enough to resolve the cold-point tropopause (CPT) well and therefore results in unrealistic dehydration patterns or biased water vapor prediction. Therefore, we also included model run using GPS temperature.

GPS provides global observations of temperature every ~60 m in the vertical (although the vertical resolution of each measurement is ~0.5 km in the upper troposphere) [*Ho et al.*, 2009]. We include GPS radio occultation (RO) data from all platforms to compensate the relatively low resolution horizontally. This includes RO from the Constellation Observing System for Meteorology, Ionosphere, and Climate (COSMIC) [*Anthes et al.*, 2008] global positioning satellite (GPS) mission, the CHAllenging Minisatellite Payload (CHAMP) satellite [*Wickert et al.*, 2001]), the Communications/Navigation Outage Forecasting System (CNOFS), the Gravity Recovery And Climate Experiment (GRACE) twin satellites [*Beyerle et al.*, 2005], the

Meteorological Operational Polar Satellite–A (MetOp-A), the Satellite de Aplicaciones Cientifico-C (SACC) satellite [*Hajj et al*., 2004], and the TerraSAR-X (TerraSAR-X). Figure 2.7 shows the profile numbers from each satellite platforms and it demonstrates that all RO profiles (black) could be twice as much as from COSMIC (crimson) alone.

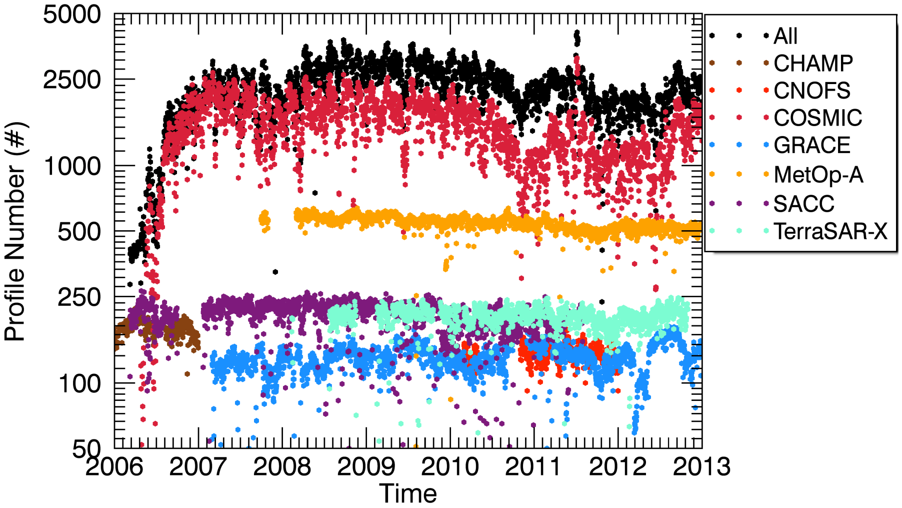

Figure 2.7. Number of GPS RO profiles from different platforms. Black shows the total profile numbers from all platforms.

We use GPS wet profile (wetPrf) products available vertically for every 100 meters. For use in our trajectory model, each day all GPS temperature profiles are binned in 200-m resolution vertically. Horizontally, we first grid data into relative coarse grids by averaging all data within adaptive searching radius of 600-1000 km (depends on the number of measurements fall into) weighted by 2-D Gaussian function, and then we linearly interpolate those coarse grids into 2.5x1.25 (longitude by latitude) finer grids to lower the possibility of trajectories encountering grids with no valid temperature.

2.3.3 Chemistry Input

Besides H_2O, O_3 and CO are also important trace gases in the UTLS that regulate the past and future climate. So one of our objectives is also to simulate $O_3$and CO transport with this trajectory domain-filling model. Trajectory modeling of O_3 and CO can provide useful tests for simplified understanding of transport and chemical processes in the UTLS, and provide complementary information to the H_2O simulations (which are primarily constrained by tropopause temperatures).

The methodology for trajectory simulations of O_3 and CO follows a similar approach to modeling H_2O. Specifically, O_3 and CO concentration carried by each parcel is altered chemically by the concentration from the previous time step and the production and loss frequencies calculated from a fully coupled chemistry climate model.

We use chemical production and loss rates output from the fourth version of the Whole Atmosphere Community Climate Model (WACCM4). The WACCM is based on the software framework of the National Center for Atmospheric Research's Community Atmospheric Model (CAM), extended vertically to the lower thermosphere. The chemical module is based upon the three-dimensional chemical transport Model for OZone And Related chemical Tracers, Version 3 (MOZART-3) [*Kinnison et al.*, 2007]. It is a fully interactive model, wherein the radiatively active gases (CO_2, H_2O, N_2O, CH_4, CFCs, NO, O_3) influence the radiative heating rates and therefore the dynamics. A finite volume dynamical core that explicitly calculates the mass fluxes in and out of a given model volume with a Lagrangian control-volume vertical discretization is applied to ensure mass conservation [*Lin*, 2004].

Recently, a new version of WACCM4 has been constructed to run with specified dynamics (SD) fields [*Lamarque et al.*, 2012], in which the WACCM4 meteorological fields are "nudged" with the SD meteorological fields such as the temperature, winds, surface pressure, etc., using the approach described in *Kunz et al*. [2011]. In this study we use the WACCM4 nudged by meteorological fields from the NASA Modern-Era Retrospective Analysis for Research and Applications (MERRA) [*Rienecker et al.*, 2011]. The vertical domain of WACCM4 extends from the surface to the lower thermosphere, with horizontal resolution of 2.5°×1.9° in longitude and latitude and 88 levels up to ~150 km. In the UTLS the vertical resolution is 1.1–1.4 km. The WACCM chemical production and loss rates and their application to our trajectory model will be discussed in detail in Sect. 4.

2.4 Validation Datasets for Trajectory Model

We will compare our model results mainly to observations of H_2O, O_3 and CO from the Aura Microwave Limb Sounder (MLS) [*Waters et al.*, 2006]. MLS measures 3500 vertical profiles per day along a sun-synchronous suborbital track having equatorial crossings at 1:40 PM and 1:40 AM local solar times. We use the MLS version 3.3 (v3.3) Level 2 products, described in the data quality and description document (http://mls.jpl.nasa.gov/data/v3-3_data_quality_document.pdf).

MLS H_2O is produced between 316 hPa to 0.1 hPa with 12 levels per decade with vertical resolution of 2.7-3.2 km in the UTLS. The measurement uncertainties (including biases) for H_2O are 20% (215 hPa) to 10% (100 hPa) at tropics and mid-latitudes, and ~50% at high latitude (>60° N-S) [*Read et al.*, 2007].

For O_3 and CO simulation, MLS observational climatology in 2005-2011 is used to set the initial abundances when parcels are initialized (~370-K isentrope), and the observations at higher levels are used to evaluate the trajectory model results. O_3 profiles are available at 12 levels per decade from 261 to 0.02 hPa and CO profiles are available between 215 and 0.0046 hPa at 6 levels per decade. The vertical resolution of O_3 in the UTLS is approximately 2.5-3 km while for CO it is ~4.5-5 km. The detailed validation for these data sets can be found in *Froidevaux et al.*, [2008], *Pumphrey et al.*, [2007], and *Livesey et al.*, [2008].

Besides using chemical production and loss from the WACCM, we also compare O_3 and CO modeled by WACCM to the trajectory model simulations, which serves as a sanity check of applying the imposed WACCM chemistry, and also as a simple comparison of Lagrangian vs. Eulerian model results.

We also compare the trajectory modeling to the CO measurements from the Atmospheric Chemistry Experiment Fourier Transform Spectrometer (ACE-FTS), which shows some systematic differences with MLS retrievals in the stratosphere (*Clerbaux et al.*, 2008; *Park et al.*, 2013). The ACE is a Canadian satellite mission primarily focused on the Arctic polar ozone loss in the winter and spring seasons. The ACE-FTS is a solar occultation instrument measuring the infrared absorption spectra that provides trace gas mixing ratios from the lower thermosphere (~5–150 km). The vertical field of view (FOV) of the instrument is ~3 km, with vertical oversampling providing an effective vertical resolution of 2–3 km; the retrievals are performed on a 1 km vertical grid [*Boone et al.*, 2005]. The sampling of ACE-FTS (resulting from the high inclination satellite orbit) provides measurements primarily over high latitudes, with limited sampling through the tropics, four times per year (February, April, August, and October) [see

Bernath, 2005]. A detailed description of the ACE CO observations can be found in *Park et al.*, [2013].

2.5 Summary

Our model is a domain-filling, forward trajectory model driven by three-dimensional winds and operates in potential temperature coordinates, where diabatic heating rates drive parcel motions across isentropic surfaces. This model is driven by three state-of-the-art reanalyses datasets: NASA MERRA, ECMEF ERA interim, and NCEP CFSR. To avoid unnecessary complexity, we homogenized all datasets in 6-hourly while keeping their own original horizontal and vertical resolution. Due to the extreme importance of temperature in our model, we chose to use the available datasets in the finest vertical resolution. Besides using reanalyses temperatures that usually have vertical resolution of 1~2 km, we also use GPS temperature that is available every 100 m vertically from the surface to ~32 km. Use of GPS temperature will give us a more detailed dehydration structure in the UTLS region (see Sect. 3.2).

For modeling chemical species, we use chemical production and loss rates from a fully coupled chemistry-climate model (WACCM). Those chemical rates represent an overall effect of the chemical sources and sinks of species, so that we don't need to consider reactions step by step. Those rates are easily to be incorporated into our trajectory model, which guarantees an easy diagnose, easy perform strategy. The details of the chemical model WACCM and its chemical production and loss rates will be discussed in detail in Sect. 4. For validation purposes, we will compare our model results with satellite observations from MLS and ACE-FTS. We will also compare our chemical products with those from WACCM, as a sanity check of the model performance.

3. TRAJECTORY MODELED WATER VAPOR AND DEHYDRATION PATTERNS IN THE UTLS

Water vapor (H_2O) is the most important greenhouse gas in the atmosphere because H_2O molecule is strongly polar in shape that results in a strongly absorbing infrared spectrum. Understanding the mechanisms that regulate it is very important for understanding past and future climate change. Of particular interest is H_2O in the UTLS because it plays a major role in the balance of planetary radiation, it influences and responds to atmospheric motions, and it plays an important role in many aspects of UTLS chemistry. For example, besides its potential effect on stratospheric ozone loss [*Vogel et al.*, 2011; *Anderson et al.*, 2012], H_2O and its feedback play an important role in regulating the global radiation budget of the troposphere [*Held and Soden*, 2000] and the stratosphere [e.g., *Forster and Shine*, 1999; *Solomon et al.*, 2010; *Dessler et al.*, 2013].

In this Section we will show H_2O simulations and dehydration patterns in the UTLS from our trajectory models driven by three different reanalyses. The different results demonstrate the differences in terms of both circulation and temperature represented in reanalyses. It will be shown that coarse vertical levels of reanalysis temperature could result in unrealistic dehydration patterns. A further update is to use GPS temperature in very fine vertical resolution, which gives us real dehydration patterns but the H2O simulation is unchanged. This, on the other hand, shows that reanalysis temperature on model native levels are already good enough for this kind of study.

3.1 H_2O Simulations

3.1.1 Modeling Generals

There are two sources for water vapor (H_2O) in the stratosphere: in situ oxidation of methane (CH_4) in the upper stratosphere and direct transport from the troposphere, which occurs in the tropical ascending branch of the Brewer-Dobson circulation [*Brewer*, 1949]. As shown in Fig. 3.1, the Brewer-Dobson circulation (BDC) transports air across the tropopause (thick grey line marks 2PVU) into the stratosphere, followed by poleward flow to the extratropics mid-latitudes and downward mass flux from the stratosphere to the troposphere at higher latitudes. In the zonally averaged sense, the Brewer-Dobson circulation is driven nonlocally by the breaking Rossby and gravity waves in the extratropical middle atmosphere. It acts as a “suction pump”, withdrawing air from the tropical upper troposphere, pushing it poleward and finally downward [*Holton et al.*, 1995].

Over the years, significant progress has been made towards understanding the details of stratospheric H_2O. It has been known that tropical tropopause temperature is the main driver of stratospheric H_2O concentration [*Brewer*, 1949]. As parcels approach and pass through the cold-point tropopause (CPT) – the altitude at which air temperature is coldest (indicated in Fig. 3.1 with white line), condensation occurs, reducing the parcel's water vapor concentration to the local saturation level [e.g., *Fueglistaler* et al., 2005]. This is the dehydration process. The bulk of evidence suggests that large-scale slow vertical ascent dominates mass transport across the tropical tropopause, and that slow ascent is required for effective dehydration.

The dehydration pattern can be understood by performing Lagrangian trajectory simulation, which tracks the temperature history of each parcel independently. Dehydration thus primarily depends on the air parcels' temperature history, and stratospheric water vapor simulations ultimately depend on accurate analysis of temperature and air parcel movement (e.g. *Mote et al.*, 1996; *Fueglistaler et al.*, 2005, 2009; *Liu et al.*, 2010; *Schoeberl and Dessler*, 2011; *Schoeberl et al.*, 2012, 2013).

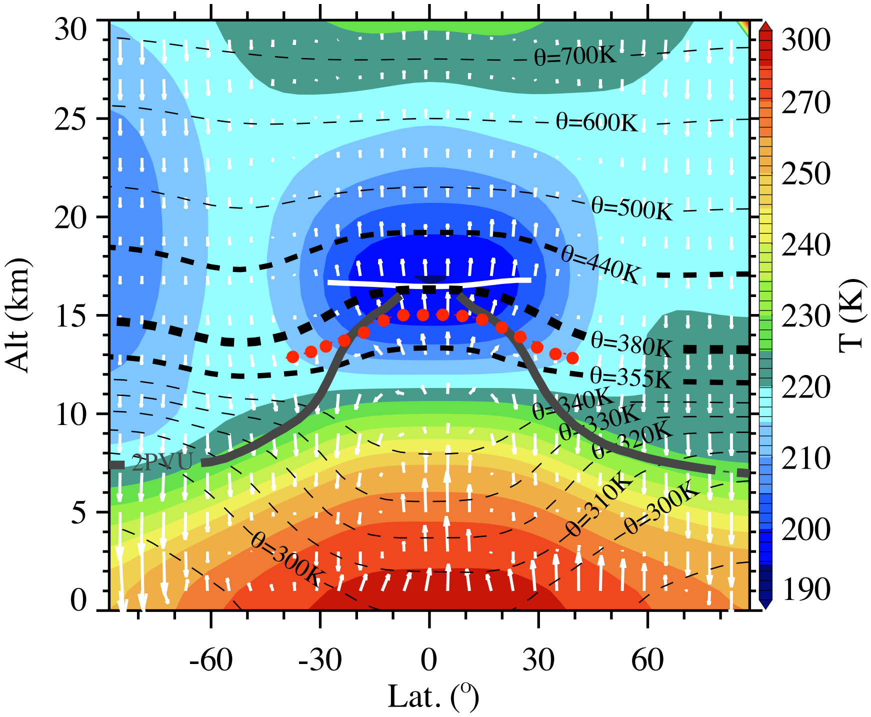

Figure 3.1. Illustration of the Brewer-Dobson circulation (BDC) in ERA interim reanalysis. The background contour color shows the zonal cross section of temperature from surface to 30 km (~10 hPa), with blue indicating the coldest temperature. Overlaid is the BDC in white vectors represented by the total diabatic heating rates. Dash lines are the potential temperature The 380-K surface is denoted by the thick line. It separates the "overworld" from the "middle" world [see Sect. 1 and *Holton et al.*, 1995]. The 355-400 K isentropes enclosed in the tropical region are generally referred as the Tropical Tropopause Layer (TTL). The level of zero net radiative heating is around the 355-K isentrope. The white line ~17 km over the tropics indicates the cold-point tropopause, where the temperature is coldest. Red dots are the parcels that we initiated in the trajectory model. See context for details.

Water vapor is unique among atmospheric trace constituents in that temperature sets an upper limit to how much H_2O can exist in the air, i.e., higher temperature potentially permit more water vapor. The Clausius-Clapeyron (C-C) equation describes this relationship mathematically, and can be estimated by

$$e_s(T) = e_s(T_0) \cdot e^{-\frac{L_v}{R_v}(\frac{1}{T}-\frac{1}{T_0})} \tag{3.1}$$

where e_s is the saturation vapor pressure, T is temperature, T_0 is a reference temperature, Lv is the latent heat of evaporation and Rv is the water vapor gas constant. The C-C equation is important because it sets an upper limit on the H_2O content for a given temperature. Once the partial pressure of H_2O reaches the saturation vapor pressure, any excess of H_2O condenses and brings the vapor pressure back down to the saturation level. This is the theoretical basis for our simulation of H_2O.

Recently, a new experimental relation that approximates the C-C equation with more accuracy was formulated by *Murphy and Koop* [2005],

$$e_{sat}^{ice} = e^{9.550426 - 5723.265/T + 3.53068\, ln(T) - 0.00728332T} \tag{3.2}$$

where T is the temperature in Kelvin and e_{sat}^{ice} is the saturation vapor pressure with respect to ice in Pascal. Because this formula holds for temperature as low as -80^{o}C, it is suitable for the purposes of our study. As the equation indicates, saturation vapor pressure in only a function of temperature, so the accuracy of temperature is of crucial importance to our modeling results. From the saturation vapor pressure, H_2O saturation mixing ratio with respect to ice is calculated as

$$[H_2O]_{sat}^{ice} = e_{sat}^{ice}/p \tag{3.3}$$

where p is the ambient pressure and [] means volume mixing ratio.

In this section, we use a forward domain-filling trajectory model (see Sect. 2) to study H_2O and the detailed dehydration behavior of air in the UTLS. We conduct diabatic runs and initiate parcels with 50 ppmv H_2O at the 370-K isentrope (red dots in Fig. 3.1), which is above the level of zero radiative heating in the tropics (355-365 K) [*Gettelman and Forster*, 2002], but is typically below the cold-point tropopause (CPT) (375–380 K). This guarantees that air parcels are situated in the ascending branch of the BDC and experience essential dehydration by passing through the CPT. Therefore, the final value of H_2O in these trajectory calculations is insensitive to the initial value, provided it is above ~20 ppmv. We continue injecting parcels into the domain everyday so that we obtain a statistically robust result (See Sect. 2)

During the trajectory integration, $[H_2O]$ is conserved along the trajectory, except when the parcel's relative humidity (RH) exceeds some critical saturation level such as 100%. At this point excess water vapor is instantly removed from the parcel to restore RH back to the critical level. As we mentioned earlier, methane oxidation is another important source of water vapor in the stratosphere, so we independently track methane in each parcel and photolyze it using photochemical loss rates supplied from the Goddard two-dimensional model [*Fleming et al.*, 2007]; loss of each methane molecule is assumed to produce two molecules of H_2O [*Wofsy et al.*, 1972; *Dessler et al.*, 1994].

We use winds and temperature from three reanalyses (MERRA, CFSR, and ERAi) to drive the trajectory model (see Chap 2). The model results are verified by comparison with satellite observations, the details of which can be found in two of our publications: *Schoeberl*, *Dessler*, *and Wang*, [2012, 2013].

3.1.2 Stratospheric H_2O and Dehydration Patterns

The global dehydration patterns from the three reanalyses are shown in Fig. 3.2. Here, we consider only the last dehydration events of parcels; that is to say, those parcels experienced no further dehydrations for at least a year. This is how we define the final dehydration points (FDPs). The dehydration patterns are similar among three reanalyses, including the large zone of dehydration over Africa, Tropical Western Pacific (TWP), and South America. MERRA also shows lower numbers of FDPs over Southeast Asia relative to the other reanalyses. Three runs all indicate a zone of FDPs over Antarctica, which is caused by the very cold temperatures within the Antarctic vortex during the Southern Hemisphere winter. This air is further dehydrated and contributes to the overall dry air in Southern Hemisphere as compared to the Northern Hemisphere (*Schoeberl and Dessler*, 2011).

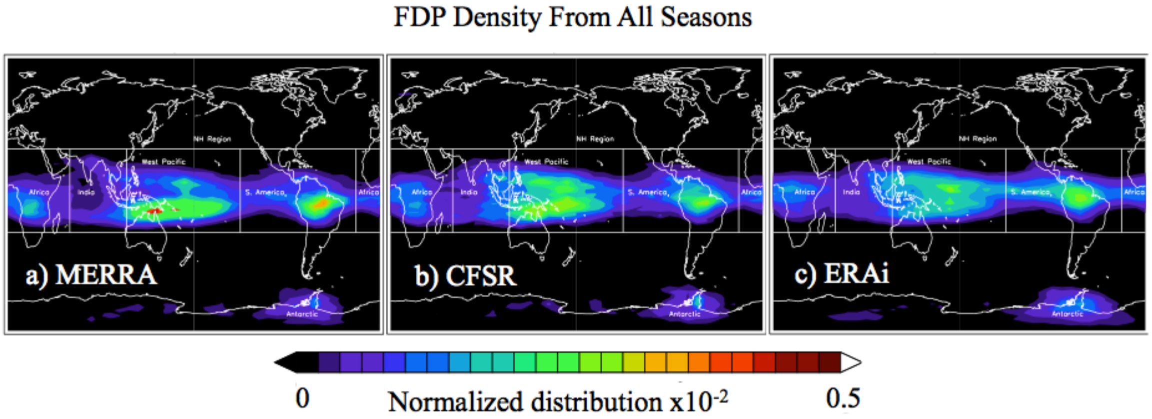

Figure 3.2. Density of final dehydration locations from the three reanalyses: (a) MERRA, (b) CFSR, and (c) ERAi. Adapted from *Schoeberl*, Dessler, *and Wang*, [2012].

Figure 3.3 shows the zonal mean [H_2O] at the end of the trajectory runs from MERRA, CFSR, and ERAi, compared to MLS observations. The differences between the simulations are less than 20%; the MERRA simulation shows the best agreement with MLS, while the CFSR run is slightly wetter and the ERAi run is drier. The differences are caused by different temperatures used in the model. The secondary dry air between 22 and 26 km centered near 25 km in the MLS data is the previous winter tape recorder signal. This has been reproduced in all simulations, except that there are some differences in the height: the MERRA run simulates it at 22.5 km, the CFSR run shows at 25 km, and ERAi modeled it at 25.5 km. Thus, MERRA has a slower tropical upward transport relative to the two other reanalyses, while ERAi is slightly faster. The above differences in temperature and vertical transport will be addressed more quantitatively in Fig. 3.4-3.6.

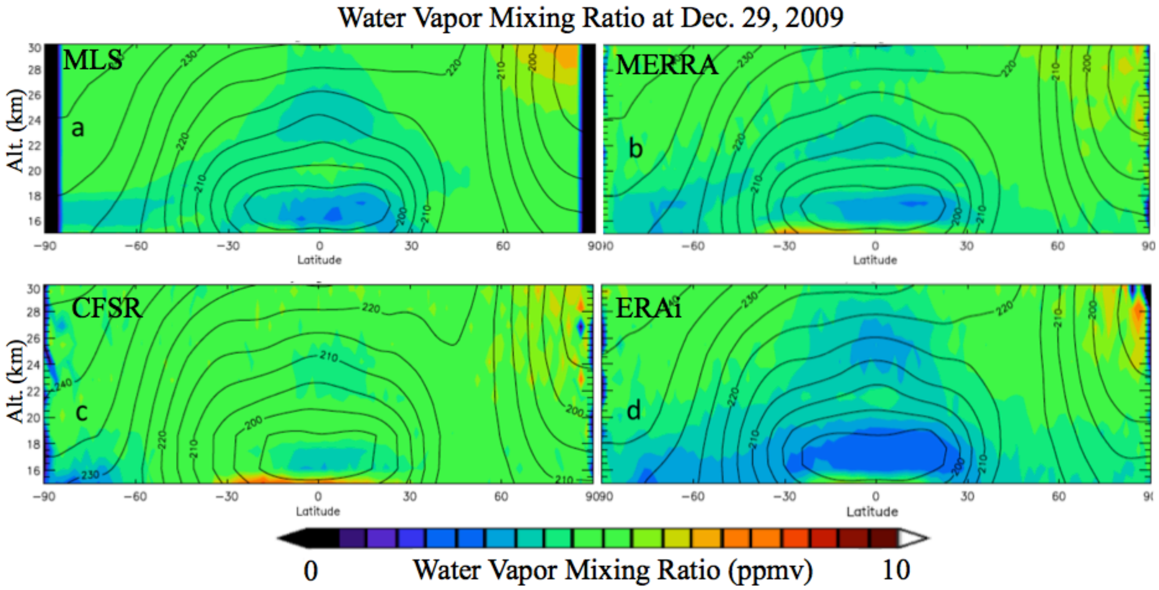

Figure 3.3. Zonal mean water vapor mixing ratio at the end of the trajectory runs from (b) MERRA, (c) CFSR, and (d) ERAi, compared to (a) MLS observations. In each panel the zonal mean temperatures are shown in black contours as references. Adapted from *Schoeberl*, Dessler, *and Wang*, [2012].

Fig. 3.4 compares the zonal cross section of temperature records averaged from 2005-2010. Panel a shows the MERRA temperature, which captures the key features of temperature in the UTLS, with the tropical minimum of 195 K around 100 hPa or the 380-K isentrope, in agreement with radiosonde observations [*Seidel et al.*, 2001]. As we have mentioned previously, accurate temperatures are critical for successful simulations of stratospheric water vapor because the entry level of H_2O is governed by the Clausius-Clapeyron equation assuming saturation with respect to ice.

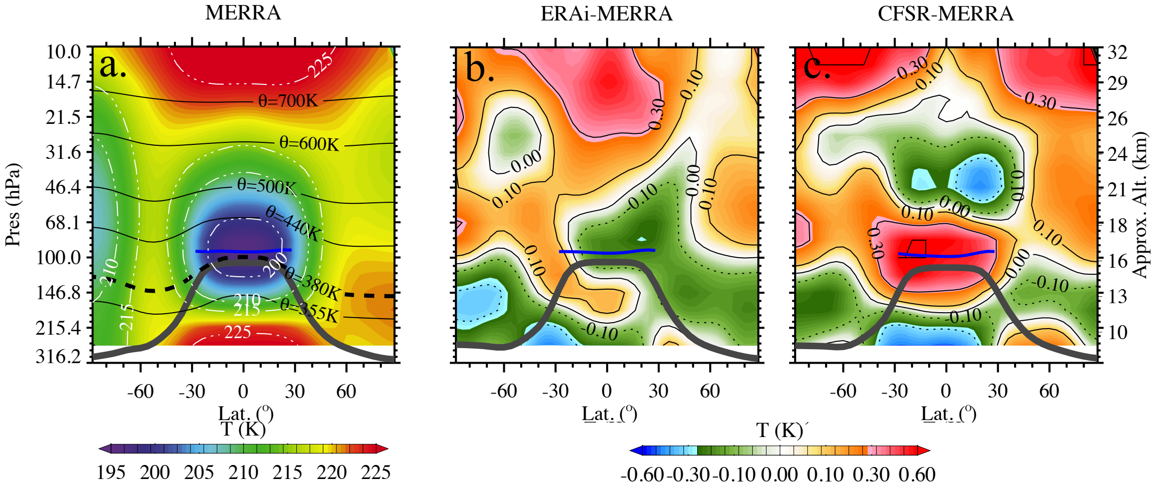

Figure 3.4. Zonal cross section of temperature among MERRA, ERAi, and CFSR averaged from 2005-2010. Panel a shows the temperature from MERRA, with dash-dotted white lines labeling the temperature and solid lines labeling the potential temperature; the 380-K isentrope is highlighted with a thick dashed line to approximate the tropopause that separates the overworld from the air below. Panel b and c are the differences between MERRA and ERAi (ERAi-MERRA), and MERRA and CFSR (CFSR-MERRA), respectively. Positive values in panel b and c means that air in ERAi and CFSR are warmer than air in MERRA; and vice versa. Thick grey lines in each panel are the lapse-rate tropopause (according to WMO definition) calculated based on their own temperature records.

Fig. 3.4b and 3.4c are the temperature difference between MERRA and ERAi (ERAi-MERRA), and MERRA and CFSR (CFSR-MERRA), respectively. Here, positive values shown in warm colors indicate warmer air compared to MERRA, and vice versa. A distinct discrepancy is evident at the tropical tropopause (around 100 hPa), where ERAi has a colder temperature of ~0.2-0.3 K and CFSR has a warmer temperature as high as ~0.7 K. These temperature differences could result in a 0.5-1.0 ppmv difference in water vapor, accounting for a 10-20% difference (see Fig. 3.5 below).

Fig. 3.5 compares the time-vertical section of tropical H_2O from the simulations with MLS observations averaged within the inner tropics (15^oN-S). This figure is also known as the "tape recorder" signal [*Mote et al*. 1996]. The tape recorder signal comes about because there are few diabatic sources and sinks for water vapor above the cold-point tropopause, and hence the "dry tongue" imprinted from the tropopause can be carried aloft for months - due to the very slow Brewer-Dobson circulation (30 m/day or ~1 K/day). Visually, this "memory" of tropopause water vapor history looks like a tape moving away from the tape head. *Schoeberl et al.* [2008] pointed out that any trace gas imprinted at the tropopause with lifetime greater than months in the lower stratosphere should produce a tape recorder signal. Therefore, we also see the CO and HCN tape signals as well [*Schoeberl et al.*, 2006; *Pumphrey et al.*, 2008].

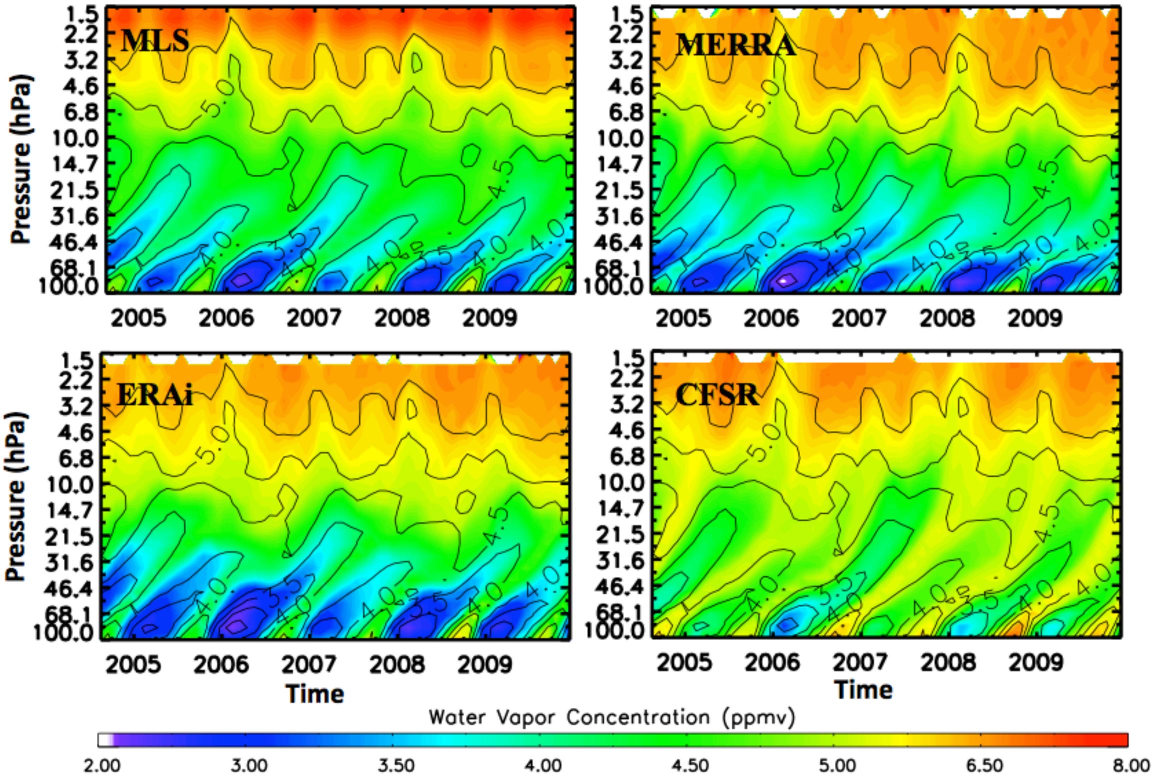

Figure 3.5. Water vapor tape recorder signal averaged over 15° N-S from August 2004 to December 2009. The black contours are MLS H_2O overlaid in each panel to emphasize the comparison in propagation of this signal.

Fig. 3.5 shows that all model runs driven by different reanalyses did a good job reproducing the tape recorder up to ~10 hPa (~30 km). Apparently, the ERAi run shows a drier stratospheric entry level of H_2O, due to the cold temperature bias displayed in Fig. 3.4b. CFSR on the other hand, shows wetter air of 0.7-1.4 ppmv due to its warm bias (Fig. 3.4c). The MLS H_2O contours are overlaid in each panel to compare the vertical propagation of the tape recorder signal. It is obvious that ERAi run creates a faster transport than the MERRA and CFSR runs, caused by the larger diabatic heating in the ERAi datasets.

The different transport time scales hinted at from three reanalyses are more clearly shown in Fig. 3.6, which compares the diabatic heating rates and thus the vertical velocities in our model. Recall that diabatic heating indicates an upward mass flux across the isentropes, while diabatic cooling indicates a downward mass flux (see Sect. 2). Deep convection preferentially occurs in the inner tropics, leading (in a time-mean zonal-mean sense) to diabatic heating (ascent) over the inner tropics and diabatic descent (cooling) over the subtropics. This figure highlights the large differences in simulated diabatic heat budgets. For example, net diabatic cooling prevails throughout the tropics in MERRA and CFSR between 200-150 hPa, while large heating exists in ERAi. Not surprisingly, the ERAi run yields much faster transport and less residence time for parcels within the UTLS.

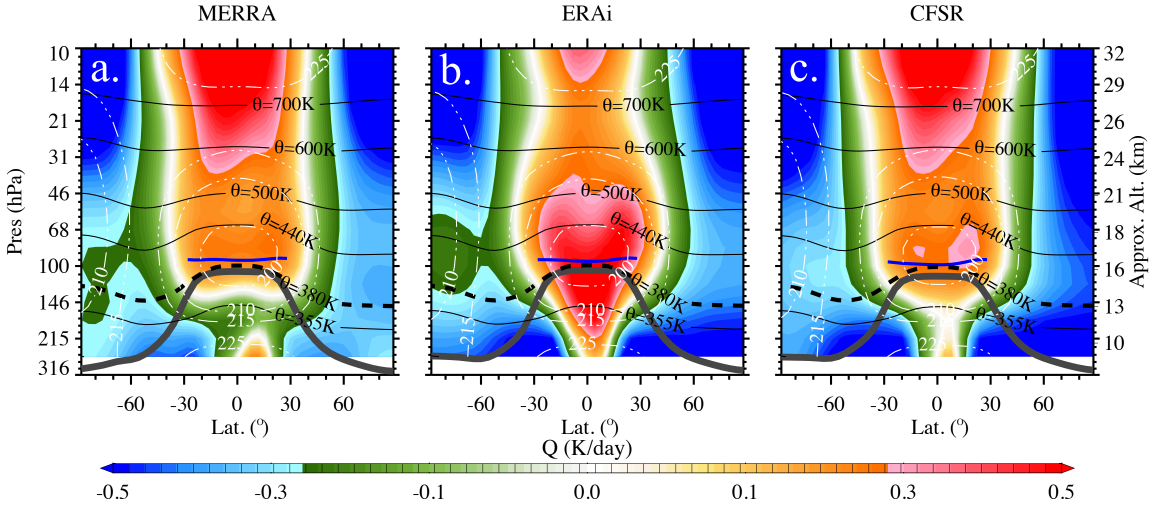

Figure 3.6. Zonal cross-section of diabatic heating rates among (a) MERRA, (b) ERAi, and (c) CFSR averaged in 2005-2010. Dash-dotted white lines label the temperature and solid black lines label the potential temperature; the 380-K isentrope is highlighted in a thick dashed line to approximate the tropopause that separates the "overworld" from the air below. Thick grey lines in each panels are the lapse-rate tropopause (according to WMO definition) calculated based on their own temperature records.

To quantify the differences between trajectory model results and the MLS observations, we can also calculate the correlation between them as a function of lags as shown in Fig. 3.7. The results show that ERAi heating rates are 30% too strong, resulting in about a 3 month lead ahead of the observations at higher altitudes; whereas MERRA heating is about 15% too weak inducing a ~2 month lag at the same altitude. It is noteworthy that although diabatic heating rates need not balance under a global average (as cross-isentropic mass fluxes must do), the presence of net negative heating rates at 220-150 hPa in MERRA and CFSR indicate a deficit in the model's diabatic heat budget simulations. Therefore, in our model parcels travelling to this region always descend back to the troposphere and are eventually removed.

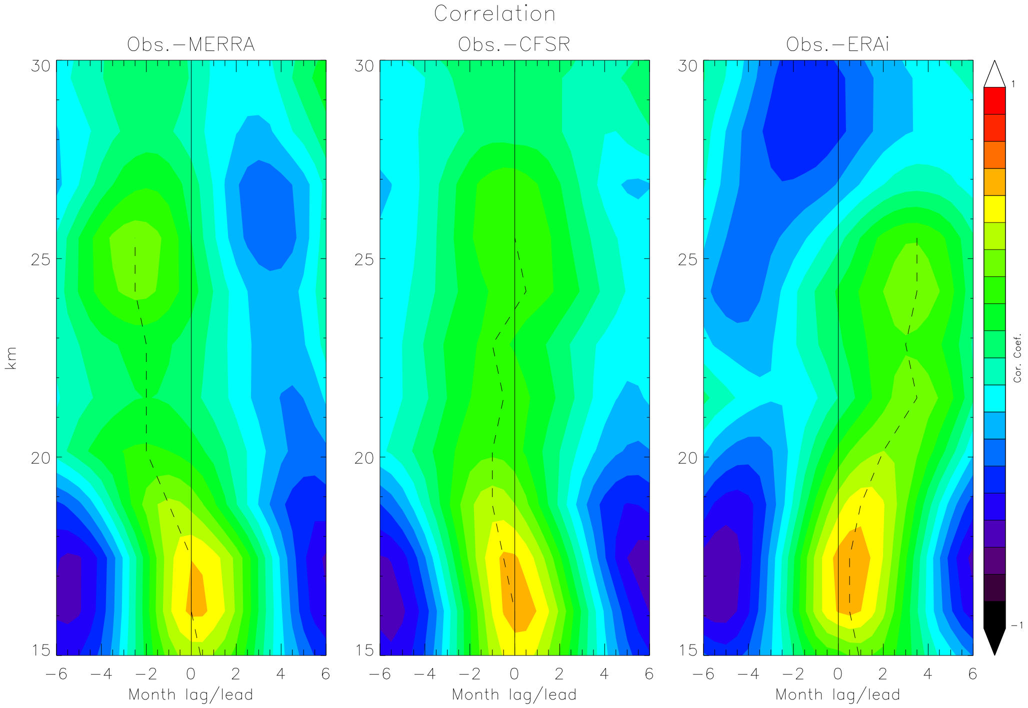

Figure 3.7. Correlation of MERRA, CFSR and ERAi results with observations after phase shifting the observations by number of months as indicated. Dashed line shows the peak correlation. Adapted from *Schoeberl et al.*, 2012.

We feel obliged to explain that the quantitative differences in modeled H_2O are tolerable as long as the general patterns are correct, because a small variation in the temperature (and pressure) field can results in large variations in H_2O. To show this we performed a sensitivity test of saturation H_2O to temperature and pressure changes around the cold-point tropopause, shown in Fig. 3.8. In panel (a) we show the saturation H_2O variations of -1.2 to 1.8 ppmv as a result of temperature deviations of ±2 K around the tropopause (typical of 192 K around 100 hPa,), which accounts for a 30-40% change of H_2O in fraction. Thus, even a small bias in reanalysis temperatures can produce a significant shift in water vapor concentration [e.g. *Randel et al.*, 2004]. Moreover, saturation H_2O is also a function of pressure. In Fig. 3.5b we demonstrate the 2-D variations of saturation H_2O as a result of change in both temperature and pressure. We can see that the combined deviations in temperature and pressure could results in 40-60% change in H_2O, i.e., ~2.3-3.0 ppmv in mixing ratio.

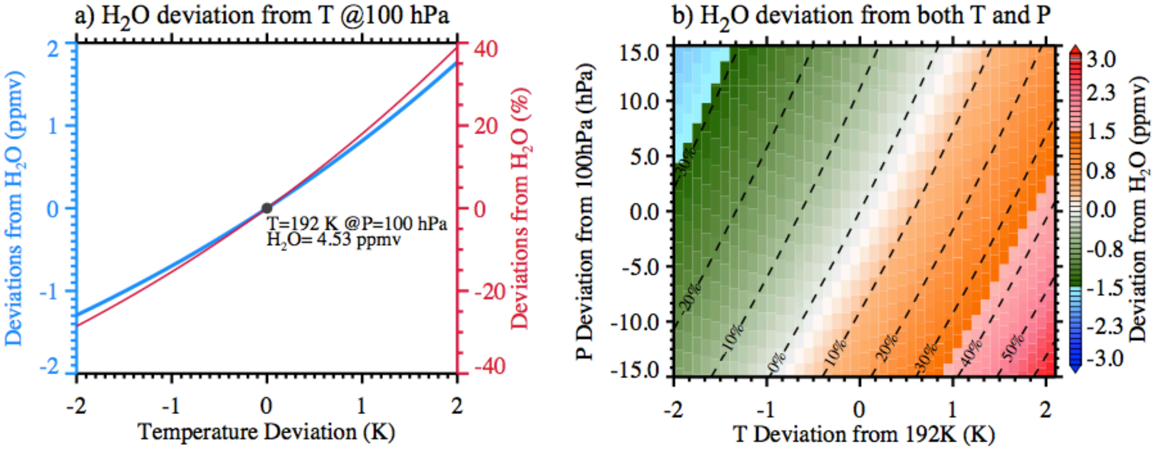

Figure 3.8. Sensitivity test of H_2O saturation mixing ratio to (a) only temperature at 100 hPa, and (b) both temperature and pressure. The temperature and pressure deviations are set to ±2 K from 192 K and ±15 hPa from 100 hPa, respectively. Those values are typical temperatures and pressures of the cold-point tropopause (see Fig. 3.1).

The temperature biases from reanalyses could be caused by many factors, such as less representation of waves or the inherent assimilation processes adopted in the reanalyses. Therefore, we emphasize that stratospheric H_2O simulation with bias of 0.5 ppmv or less is acceptable [*Schoeberl et al.*, 2013], and for climate studies usually the anomaly from removing annual cycles is even more useful [*Schoeberl et al.*, 2012, 2013; *Dessler et al.*, 2013].

The trajectory model driven by three reanalyses is able to reproduce basic features of stratospheric water vapor very well, although quantitative differences exist due to differences in temperature and diabatic heating from reanalyses [*Schoeberl and Dessler* 2011; *Schoeberl et al.*, 2012, 2013]. Regulated by temperature, dry bias in water vapor is caused by colder temperature around the cold-point tropopause (ERAi), whereas wet bias is caused by warmer temperature (CFSR). The MERRA run, however, creates H_2O most consistent with MLS observations, indicating relatively reliable temperature records from MERRA.

3.2 Dehydration Patterns Obtained Using GPS Temperature

3.2.1 The Issue: Dehydrations Cluster in Reanalyses Levels

The well-reproduced water vapor in the stratosphere tells us that the circulation in UTLS is well resolved by reanalyses. Among which, MERRA reanalysis yields the best estimates of H_2O as compared to the Aura Microwave Limb Sounder (MLS) observations [*Schoeberl et al.*, 2012, 2013]. However, the MERRA temperature in relatively coarse vertical resolution may not resolve the cold-point tropopause (CPT) well and therefore results in unrealistic dehydration patterns. For example, Fig. 3.9 shows the dehydration frequency from trajectory calculations driven by MERRA wind and temperature on native model levels [*Rienecker et al.*, 2011]. The FDP events were collected within 35° N-S – thus ignoring polar dehydrations, and that reached altitudes higher than 110 hPa for 180 days after their FDP event - thus insuring that the parcels were, for at least 6 months, stratospheric.

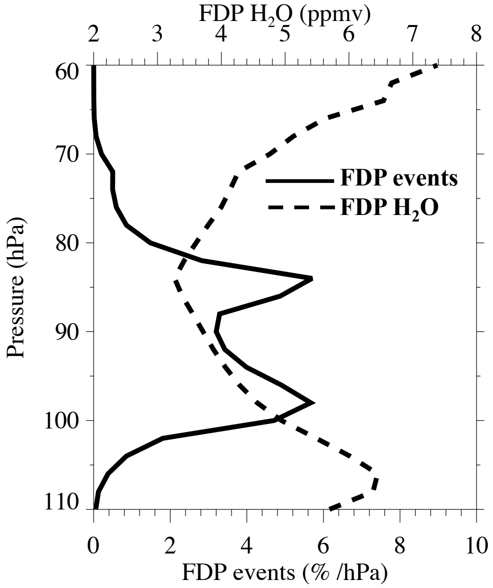

Figure 3.9. Frequency of FDP events (percent per hPa, solid line, lower x axis) and mean final saturation H_2O concentrations (ppmv) as function of pressure (dashed line, upper x axis).

As we can see that dehydration occurs almost exclusively between 70 and 110 hPa, and exhibits a bimodal distribution with distinct maxima at ~98 and ~85 hPa. The dashed line represents the average FDP saturation mixing ratio (FDP-H_2O), which reaches a minimum at the 85-hPa dehydration maximum, meaning parcels dehydrated in the vicinity of 85-hPa carry the smallest water vapor mixing ratio into the stratosphere. The relatively high FDP-H_2O at pressure levels lower than 80 hPa (just above the entry level) comes from the dehydration of parcels that avoided the tropical cold trap and are dehydrated at warmer levels of the stratosphere. Among a total of 1.3 million parcels, only ~0.7% bypassed the cold-point tropopause carrying relatively large amount of water vapor. Thus, we see no evidence that these parcels disproportionately moisten the stratosphere.

The two peak levels correspond to ~17 and ~16 km, respectively – the altitudes of the tropopause height cycle observed by *Reid and Gage* [1996], suggesting a seasonal cycle origin to the distributions. However, given the gradual transition of the tropopause through seasons, is the extremely pronounced bimodal dehydration shown in Fig. 3.9 real? Is it true that the dehydration experience a sudden decrease between the two levels? This brings up the importance of accurate temperature for trajectory simulations of H_2O in the UTLS.

In order to answer those questions, we chose to run our trajectory model with available GPS temperatures in very fine vertical resolution to constrain the water vapor simulation. We swap GPS temperatures in for MERRA temperatures to compute water vapor and the MERRA circulation (winds, heating rates) are not changed. We call a trajectory driven by MERRA wind and temperature the ***MERRA run***; and a trajectory driven by MERRA wind and GPS temperature the ***GPS run***. This naming convention will be used throughout the rest of this section.

3.2.2 Reconstruct GPT Temperature Input

The GPS temperature captures the cold tropopause temperature more accurately in unprecedentedly high vertical resolution. As stated in Sect. 2, we include GPS radio occultation (RO) data from all platforms to compensate the relatively low resolution horizontally. We use GPS wet profile (wetPrf) products available vertically for every 100 m from surface to ~34 km. Like we mentioned in Sect. 2, each day all temperature profiles are binned in 200-m vertically. Horizontally, we first grid data into relatively coarse grids by averaging all data within an adaptive searching radius of 600-1000 km (depends on the number of measurements fall into) with 2-D Gaussian function weight, and then linearly interpolate the coarse grids into 2.5x1.25 (longitude by latitude) finer grids to decrease the possibilities of trajectories encountering grids with no valid temperature. Fig. 3.10 compares the original GPS temperature profile at 100 hPa in Novermber 1, 2011, with the recovered temperature. The gridded field seems to reproduce many important features of the tropopause temperature, including the cold-trap in the tropical western pacific [*Holton et al*., 1995], etc.

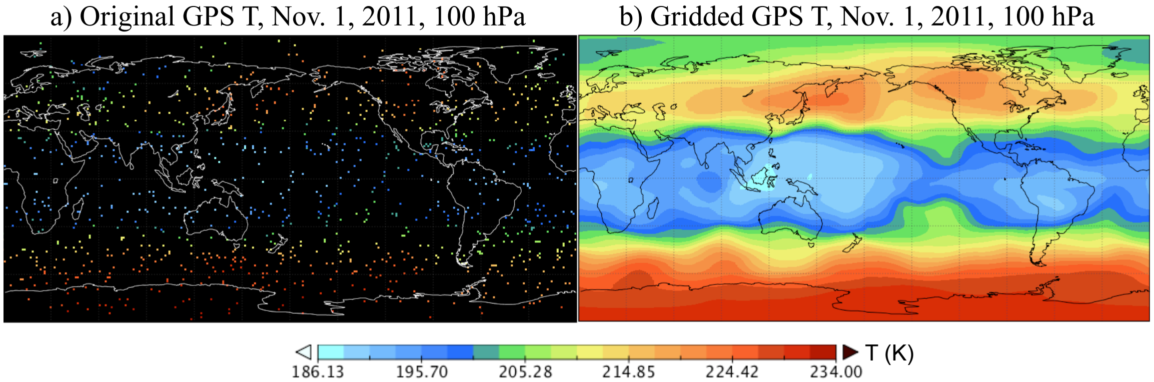

a) Original GPS T, Nov. 1, 2011, 100 hPa

b) Gridded GPS T, Nov. 1, 2011, 100 hPa

Figure 3.10. (a) Snapshot of temperature from MERRA and gridded GPS at 100 hPa on 01/01/2007, and (b) the tropical average temperature profile difference (MERRA-GPS) averaged from (18^{o}S-18^{o}N) from July 2006 to December 2012. Dash-dotted line shows the zero line for reference. Positive difference means MERRA temperature is higher than that of GPS; and vice versa.

Fig. 3.11 compares two snapshots (Jan. 1, 2007 and Jul. 1, 2007) of GPS gridded temperature and the MERRA records. It demonstrates that the gridding strategy adopted is able to reproduce temperature field in good agreement with that from reanalysis, although some detailed structure might be lost from extensive interpolation and averaging.

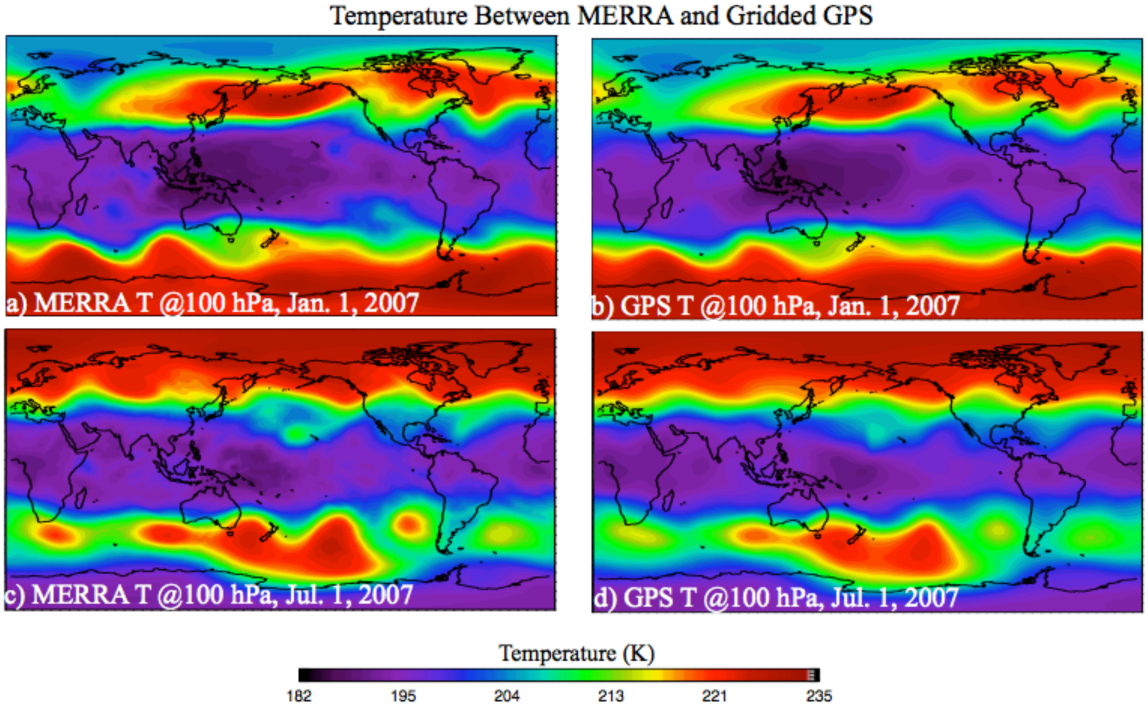

Figure 3.11. Snapshot of gridded GPS temperature at 100 hPa compared with MERRA temperature on January 01, 2007 (a, b) and July 01, 2007 (c, d).

Fig. 3.12 shows the temperature profile difference between MERRA and GPS (MERRA-GPS, black like), averaged over the deep tropics (10° N-S) during the GPS period. Here we interpolate all datasets into the same vertical grids to do a parallel comparison. Apparently MERRA has a warm bias around the tropopause of 0.1-0.4 K, potentially corresponding to 0.08-0.42 ppmv moist bias in entry level stratospheric water vapor assuming 100% saturation. In order to prove that our gridded GPS temperature is good enough, we also included the temperature difference between ERAi and GPS (ERAi-GPS, blue in Fig. 3.12), to be compared with the analysis performed by *Fueglistaler et al.*, [2013] in their Figure 19. There, they compared the COSMIC temperature with ERAi temperature. In Fig. 3.12 the three closest levels (146.4, 93.8, 68.1 hPa) noted in blue (with temperature differences) are compared with the levels (153, 96, 67 hPa) examined in *Fueglistaler et al.*, [2013] noted in red. As shown the comparisons are very close, which demonstrates that our gridded GPS temperatures are suitable for use within the model.

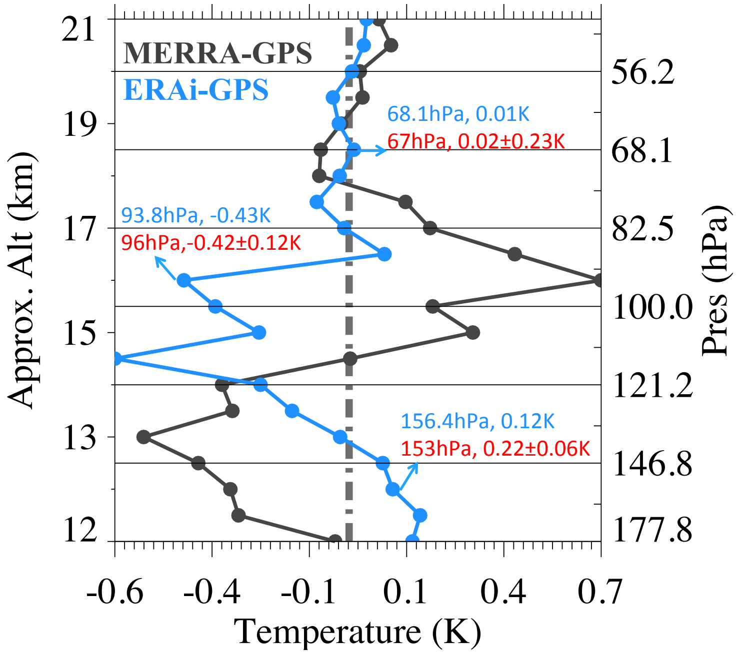

Figure 3.12. Temperature differences between MERRA and GPS (MERRA-GPS, black), and between ERAi and GPS (ERAi-GPS, blue), averaged over the deep tropics (10° N-S) during the GPS period. Dash-dotted line shows the zero line for reference. Positive difference means reanalyses is warmer than that of GPS; and vice versa. Three levels (153, 96, 67 hPa) examined in *Fueglistaler et al.*, [2013] with temperature differences of ERAi to COSMIC, noted in red, for comparison with our calculated differences.

3.2.3 Dehydration Patterns Obtained Using GPS Temperature

Driven by the MERRA winds and GPS temperature, the FDP frequency and associated H_2O in addition to the previous results are shown in Figure 3.13. Recall that during the trajectory calculations, interpolating MERRA temperature linearly yields H_2O in agreement with that from the MLS observations (*Schoeberl and Dessler* 2011, *Schoeberl et al.*, 2012), but the dehydrations are constrained by the MERRA fixed model levels so a bimodal FDP frequency is found (black line). Using GPS temperature in high vertical resolution, dehydration events show single peak around the cold tropopause (blue solid line) and the FDP-H_2O (blue dashed line) is in agreement with that of the linear interpolation (black dashed line). The GPS run yields a realistic FDP pattern and reasonable FDP-H_2O.

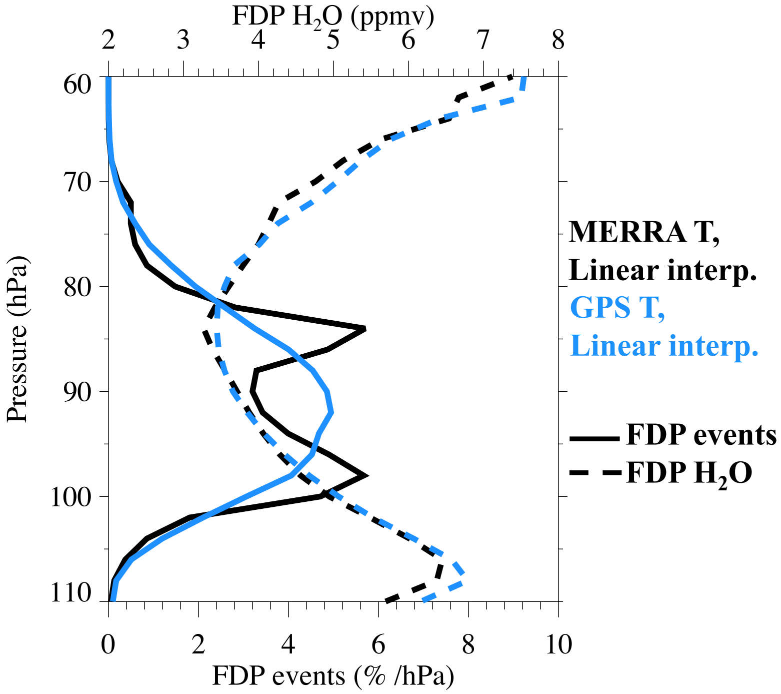

Figure 3.13. Annual average vertical distributions of FDP events (percent per hPa, solid lines, lower x axis) and FDP saturation mixing ratios (FDP-H_2O in ppmv, dashed lines, upper x axis) from trajectory simulations with linear interpolation on MERRA temperature (black) and linear interpolation on GPS temperature (blue). The black lines repeat from Fig. 3.9.

Questions still remain: Are there tremendous differences in latitudinal or longitudinal structures of FDPs between MERRA and GPS runs? Will it vary with seasons or affect stratospheric water vapor predictions? What is the main cause of the difference? Does the difference really matter?

Figure 3.14 compares the horizontal view of final dehydration patterns from the MERRA run (left, constrained by MERRA temperature) and the GPS run (right, constrained by GPS temperature), respectively. FDP occurrence frequency is normalized in each panel by their respective range so as to facilitate comparison. The annual distribution of FDPs in Fig. 3.14a-b show consistent patterns between two calculations, with distinct enhancements over northern South America, South Africa, and the tropical Western Pacific (TWP), following the longitudinal structure of the cold-point tropopause [e.g., *Highwood and Hoskins*, 1998; *Randel et al.*, 2003]. These are also the regions experiencing frequent deep convection, and the low temperatures associated with convection drive dehydration (although we do not parameterize convection in the model).

Fig. 3.14c-d shows the latitudinal variation of FDP occurrence through the year between two runs. Overall, FDP events tend to occur preferentially in the Summer Hemisphere. The FDP occurrence is elevated throughout the year in the TWP, with dual maxima seen at 10^{o}N and 10^{o}S corresponding to the two different phases of the seasonal cycle. FDP events over South America and Africa also exhibit a strong seasonal cycle, being most prominent in boreal winter (DJF) and vanishing entirely during boreal summer (JJA). The FDP saturation mixing ratio (FDP-H_2O, not shown here) shows minima approximately collocating with the FDP occurrence maxima, as expected since FDP frequency should be the highest where saturation mixing ratios are generally the lowest.

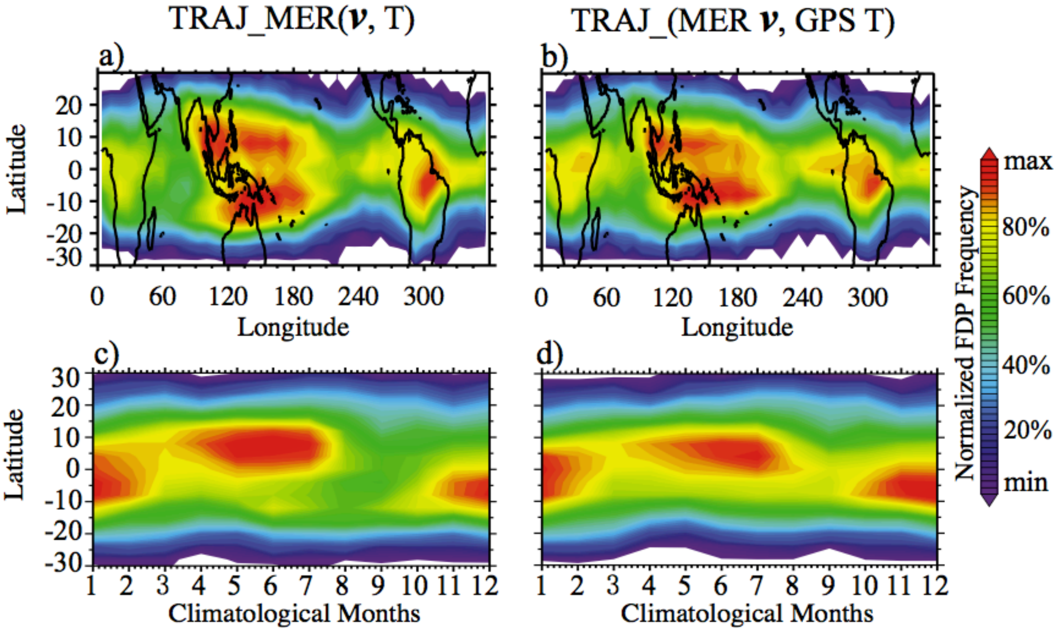

Figure 3.14. FDP events in map view (panel a, b) and latitudinal evolution view (panel c, d) from trajectory simulations by using MERRA temperature (left column) and GPS temperature (right column). All panels are plotted in their own range and color coded at the same percentiles (0, 20%, …, and 100%) to compare the patterns.

The vertical cross section of FDP occurrences in Fig. 3.15a-b (zonal) and Fig. 3.15c-d (longitudinal), however, show obvious discrepancies between the two runs, with the bi-modal feature of using MERRA temperature standing out in contrast to the single mode feature of using GPS temperature. This has already been shown previously in Fig. 3.9 but here with more specific structures. In Fig. 3.15a and 3.15c the FDP enhancements centered at 85 hPa and 98 hPa, corresponding to the most frequent CPT altitudes during DJF and JJA, respectively. Coincidently, MERRA temperature has two fixed levels – 100 and 85.4 hPa that represent the variations of CPT during these two seasons. However, MERRA does not have temperature in finer vertical resolution between 85.4 and 100 hPa that covers the variations of most frequent CPT during MAM and SON, which makes the enhanced FDP regions showing a discontinuous transition from DJF to MAM and from

JJA to SON (Fig. 3.15e). Using GPS temperature, however, yields smoother and continuous transitions (Fig. 3.15f).

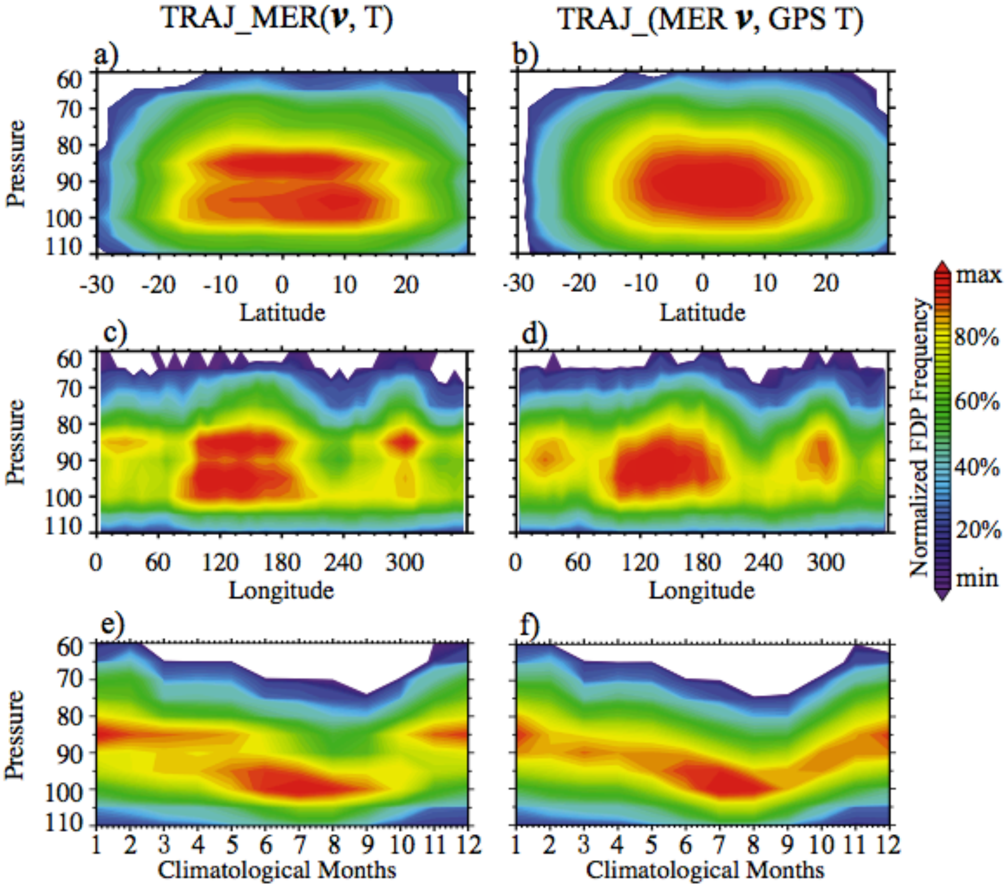

Figure 3.15. Comparing the latitudinal (panel a, b), longitudinal (panel c, d), and the evolutional (panel e, f) view of the vertical distributions of FDP events from trajectory simulations by using MERRA temperature (left column) and GPS temperature (right column). Color bar follows the same convention as in Fig. 3.14.

The reason for bimodal and discontinuous feature from MERRA run is demonstrated in Fig. 3.16, which compares the seasonal variations of the cold-point tropopause (CPT, panel a-d) in MERRA and GPS temperature and the FDP patterns divided into seasons from the two runs (panel e-h). The upper row in Fig. 3.16 shows that MERRA CPT (black discrete bars) can only be found at 4 fixed native model levels

(118.3, 100.5, 85.4, and 72.6 hPa) within the TTL due to limited vertical resolution, whereas GPS CPT (blue continuous bars) exhibits smoother fine-scale variations. Accordingly, FDP frequencies from MERRA run (black lines in panel e-h) show consistent peaks following MERRA *discrete* CPT altitudes.

Compared with GPS temperature, MERRA temperature in native levels of 85.4 hPa and 100.5 hPa ***coincide with*** the most prominent CPT altitudes during DJF and JJA, respectively (panel a, c). Thus, the FDP frequency (panel e, g) shows single over-represented peaks in each season. During MAM and SON, however, the most pronounced CPT in the real atmosphere falls within the two levels, where MERRA has no temperature records. Therefore, instead of having a single sharp CPT during DJF and JJA, the CPT resolved in MERRA temperature during MAM and SON can be *equivalently found at the two closest levels* (panel b and d, CPT shows comparable fractions) where air dehydrates most frequently. This is why the dehydration shows bi-modal feature in *both* MAM and SON but in DJF and JJA it shows a single peak. This under-represented CPT between 100 and 85 hPa in MERRA is therefore responsible for the discontinuity in FDPs shown in Fig. 3.15. Thus, all those make the final results bimodal inevitably. As a reference we also plotted the FDP variations from the GPS run (blue lines in lower row), which always produces a single peak following smoother evolutions of the CPT.

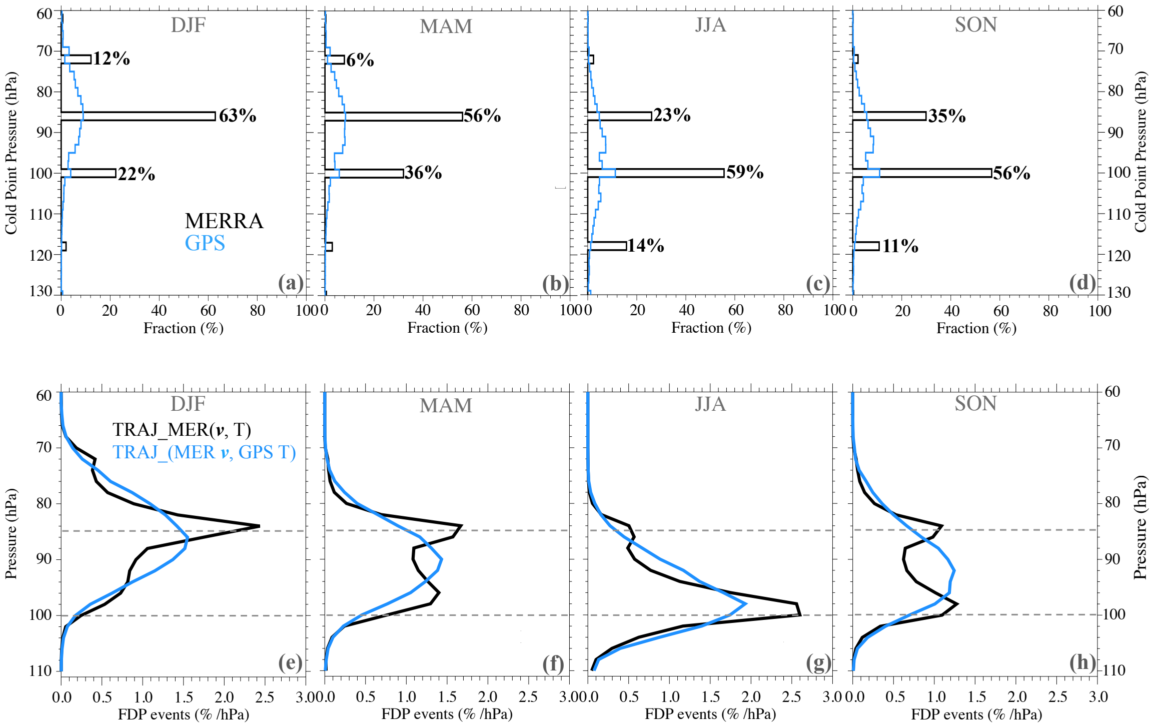

Figure 3.16. Seasonal variations of cold-point tropopause (CPT) in MERRA (black) and GPS (blue) temperature (upper row, panel a-d) and the FDP events (percent per hPa, lower row, panel e-h) from trajectory simulations using MERRA temperature (black) and GPS temperature (blue). Each season shows the fraction with respect to the total number of FDP events, so that the sum of the FDP frequencies equals that in Fig. 3.12. Two dashed lines in panels e-h are the two discrete MERRA levels (85.4 and 100.5 hPa).

Based on the discussion above, we understood that the limited two discrete levels (85.4 and 100.5 hPa) in MERRA temperature contribute to the bimodal and discontinuous dehydration patterns. To summarize, during DJF and JJA, CPT is overly represented in MERRA's two native model levels, respectively. This creates single sharp peaks of FDPs in each season. During MAM and SON, however, CPT is equivalently over-represented in MERRA's two native model levels, which creates double peaks of FDPs in each season. These factors contribute to the annual bi-model feature of FDPs from the MERRA run.

3.2.4 Water Vapor Obtained Using GPS Temperature

Previous results demonstrate that using GPS temperature in high vertical resolution yields more realistic FDP patterns around the cold tropopause. However, no distinct differences exist in the FDP saturation mixing ratio (FDP-H_2O) (Fig. 3.13 dashed blue and black lines). A more interesting question is whether the different dehydration occurrences tremendously affect the stratospheric H_2O field predicted from trajectory simulations.

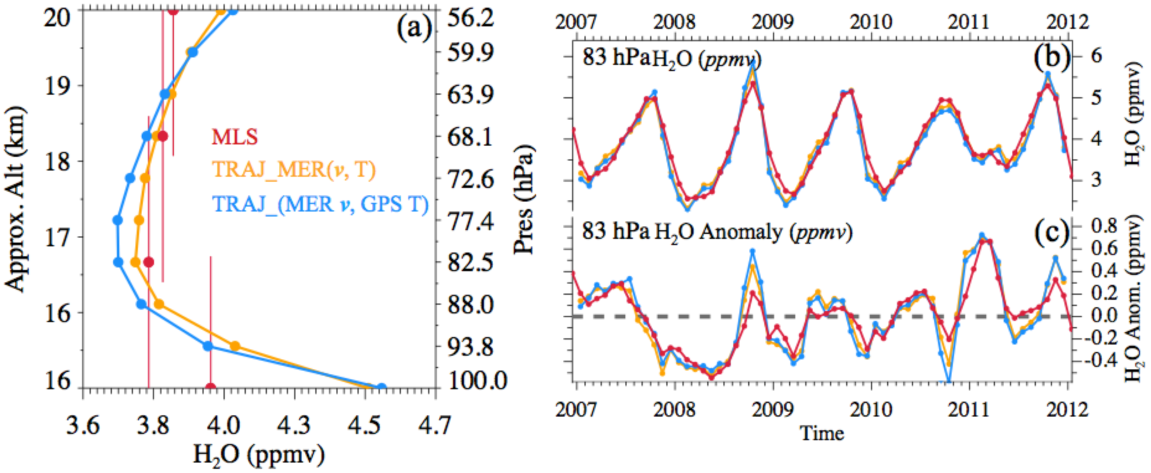

Figure 3.17. Comparisons of (a) vertical profiles, (b) time series, and (c) time series of anomalies of stratospheric H_2O averaged over the tropics during 2007-2012 from MLS (red) and the trajectory simulations using MERRA temperature (orange) and GPS temperature (blue), respectively. The solid vertical lines in red are shown to emphasize the vertical resolutions (in kilometers) at each of the MLS retrieval pressure levels.

Fig. 3.17 compares the stratospheric H_2O predicted from trajectory calculations by using both MERRA (orange) and GPS (blue) temperature with MLS observed H_2O (red). Apparently, both the MERRA run and the GPS run yield slightly drier air around the tropopause, which could result from no convective moistening of air in the trajectory calculations. The even drier air from the GPS run is well expected because GPS temperature is about 0.1-0.4 K lower than that of MERRA (see Fig. 3.12). However, compared to the H_2O abundances within this layer, the differences are only about 1-3%. The 83-hPa time series of H_2O (Fig. 3.17b) and its anomaly (Fig. 3.17c) also demonstrates consistent results between the two runs. Therefore, we are confident that the MERRA run yields reasonably good results and MERRA temperature (in native model levels) is as good as GPS temperature (in high vertical resolution) for this type of study.

Fig. 3.18 compares the climatological tape recorder signal produced by the two runs and the differences between them. Drier air was imprinted at the tropopause from the GPS run since DJF, resulting in dry biased tape signal throughout the entire upward transportation (panel b). Generally, the MERRA run yields up to 0.15-ppmv warmer air, in agreement with the temperature bias in MERRA. However, the prominent difference also exists in MAM and SON at about 90 hPa, which comes from the fact that CPT during these two seasons is not well resolved by MERRA temperature. Other than that, both the MERRA run and the GPS run did a decent job in reproducing the "memory" effect of stratospheric H_2O.

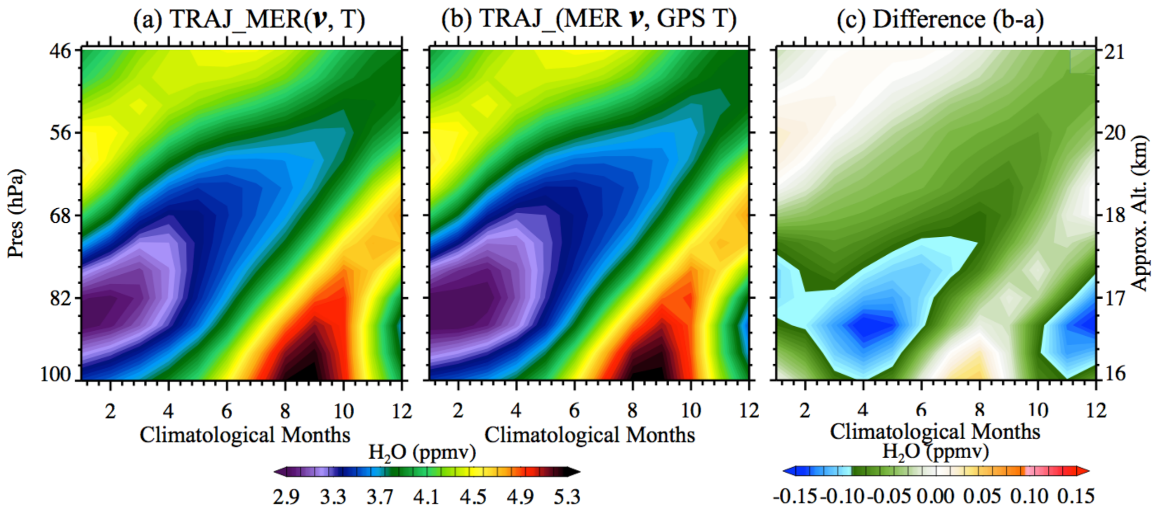

Figure 3.18. Tape recorder signal from trajectory simulations using (a) MERRA temperature and (b) GPS temperature and (c) their difference.

3.3 Summary

The Trajectory model driven by three reanalyses (MERRA, ERAi, and CFSR) is able to reproduce basic features of stratospheric water vapor very well, although quantitative differences exist due to somewhat different temperature and diabatic heating in reanalyses [*Schoeberl and Dessler* 2011; *Schoeberl et al.*, 2012, 2013]. Regulated by temperature, a dry bias in water vapor is caused by colder temperature around the cold-point tropopause (ERAi), whereas a wet bias is caused by warmer temperature (CFSR). The CFSR tropical tropopause temperatures are warmer than MERRA leading to ~0.7-1.1 ppmv more water vapor at the tropopause, whereas the ERAi is cold biased relative to other reanalyses, producing 0.5-0.8 ppmv less water vapor.

Besides temperature, another important factor that controls the vertical transport of predicted water vapor in our model is the vertical velocity (dictated by diabaitc heating rates). The ERAi run creates a faster transport than the MERRA and CFSR runs (Fig. 3.5), caused by the larger diabatic heating in ERAi datasets (Fig. 3.6). A time-lag analysis by *Schoeberl et al.* [2012] shows that ERAi heating rates are 30% too strong, results in about a 3 month lead ahead of the observations in higher altitudes; whereas MERRA heating is about 15% too weak causing a ~2 month lag at the same altitude.

During the trajectory integration, using MERRA temperature results in a bimodal FDP distributions due to limited model levels in MERRA (Fig. 3.9, 3.13), although the predicted stratospheric H_2O agrees with observations [*Schoeberl and Dessler* 2011; *Schoeberl et al.*, 2012, 2013]. Using GPS RO temperature in very fine vertical resolution, however, creates more realistic dehydration patterns (Fig. 3.13-3.15) while keeping the predicted stratospheric H_2O correct (Fig. 3.17-3.18). This is because the GPS high-resolution temperature resolves the variability of finescale structure of the cold-point tropopause (CPT) very well (Fig. 3.16a-d).

The FDP bimodal patterns of using MERRA temperature are caused by the limitation of two discrete levels (100.5 and 85.4 hPa) representing seasonal variations of cold-point tropopause (Fig. 3.16). Nevertheless, the predicted stratospheric water vapor has no evident discrepancies between the MERRA run and the GPS run (Fig. 3.17-3.18), indicating that MERRA temperature in model native levels are good enough for simulating stratospheric water vapor with zeroth order physics (or simply the ice formation processes). Therefore, for this type of study it is not necessary to use temperature records with higher resolution like GPS. However, MERRA temperature could provide accurate simulations over an even longer period so for long term studies MERRA temperature is qualified enough.

4. TRAJECTORY MODELED CHEMICAL TRACERS AND THE INDICATED UPWELLING IN THE UTLS

Ozone (O_3) is radiatively important in our climate system due to its greenhouse effect. O_3 abundances in the UTLS vary in a wide dynamic range, and are influenced by a variety of chemical and dynamical processes. Carbon monoxide (CO) is produced near the Earth's surface through combustion processes and it can be transported upward to tropopause via deep convection. CO is insoluble in the atmosphere, which makes it distinct in understanding the transport pathways. In the UTLS, both O_3 and CO experience drastic changes in concentrations. The strong vertical gradients of species reflect the large contrasts of their stratospheric vs. tropospheric sources and sinks [e.g., *Gettelman et al.*, 2011]. Therefore, a pair of tropospheric-stratospheric tracers (O_3 vs. CO) can be used to identify the chemical transport behavior and explore the tracer variability in the UTLS, which are the main objectives of this study.

In this section we will explain the chemical parameterizations adopted in our model. It will be shown that this simple parameterization is quite useful in trajectory modeling of chemical species, and the results agree very well with the satellite observations. More interestingly, this model enables to dig into the question as to what is the main driver of chemical variability around the tropopause. Is it horizontal in-mixing or vertical upwelling? This question will be addressed in detail in the last part of this section.

4.1 Chemical Continuity Equation

To understand the chemistry of the UTLS, we start with the continuity equation. For a unit volume of air in the UTLS, the continuity equation for a constituent χ is expressed as

$$\frac{\partial[\chi]}{\partial t} = \left(P_\chi - LF_\chi \cdot [\chi]\right) + (-\nabla \cdot \vec{\boldsymbol{V}}[\chi]) \qquad (4.1)$$

Here, the abundance of constituent χ is usually in number density with unit of molecules per cubic centimeter (molecules cm^{-3}) or in volume mixing ratio (VMR) with no unit. The VMR of χ is the fraction of molecules in a given volume of air molecules, so it is dimensionless and never exceed 1. In chemistry, the VMR is usually expressed as parts per million by volume (ppmv) or parts per billion by volume (ppbv).

The continuity equation expresses local tendencies of χ in abundances per unit time, so each term in the right hand side of Eqn. (4.1) has units of molecules cm^{-3} per unit time or VMR per unit time, and they represent the sources and sinks of χ occurring in the unit volume per unit time.

The first term (first parenthesis) shows the net chemical change of χ, where P_χ is the photochemical production rate and ($LF_\chi \cdot [\chi]$) is the loss rate. P_χ represents the amount of χ produced per unit volume per time, and it always indicates sources of χ, leading to a positive change. The photochemical loss term is written as the product of loss frequency LF_χ (in units of inverse time) and the abundance of χ, indicating the sinks of χ and leading to a negative change. A linear chemical loss is adopted because the rate of destruction of χ is generally proportional to its abundance. The second term on the right is the divergence of the flux of χ – it represents the net transport of χ in and out of the unit volume per unit time, indicating either sources or sinks, and then can be either positive or negative. In total if the sources and sinks balance, then there is no net change in the abundance of χ, so $(\partial[\chi])/\partial t = 0$.

Depending on the location, time of year, and species in question, the continuity equation might be dominated by either the chemical production/loss or transport term. For example, above 10 hPa (~30 km, well into the stratosphere) the photochemical term is much larger than the transport ($\nabla \cdot (\vec{\boldsymbol{V}}[\chi])$ term for ozone and its abundance will be dominated by chemical production and loss, and less affected by transport. In the lower stratosphere, however, chemical transport acts efficiently to re-distribute chemical abundances, so transport is even more important [see section 4.3.3, 4.4, and 4.5 for more details].

4.2 O_3 and CO Chemistry in the UTLS

Due to the structure of the UTLS and the complex dynamics of the region (e.g. transport across the tropopause), O_3 and CO chemistry in the UTLS is neither purely tropospheric nor purely stratospheric. In this section, important reactions and reaction types that lead to O_3 and CO formation or destruction in both the troposphere and the stratosphere are presented.

4.2.1 O_3 Chemistry

The Chapman cycle [*Chapman*, 1930] was proposed in 1930 to understand the origin of ozone layer in the stratosphere. It postulated that the ozone layer originates from the photolysis of atmospheric O_2 with the following four reactions.

$$O_2 + h\nu \xrightarrow{\lambda<240\ nm} O(^3P) + O(^3P) \qquad (R1, \textbf{slow})$$
$$O(^3P) + O_2 \xrightarrow{M} O_3 \qquad (R2, \textbf{fast})$$
$$O_3 + h\nu \xrightarrow{\lambda<320\ nm} O_2 + O(^3P) \qquad (R3, \textbf{fast})$$

$$O_3 + O \longrightarrow 2O_2 \qquad (R4, \textbf{slow})$$

Here, (*R1*) is slow photolysis with photons of wavelengths less than 240 nm. Photolysis of O_2 yields two O atoms in groud-level triplet state $O(^3P)$, which is highly reactive due to their two unpaired electrons. They react fast with O_2 to form O_3 (*R2*) and then O_3 keeps photolyzing with lower-energy photons (due to weaker bonds) to regenerate O_2 and O atoms (*R3*). Because of the rapid cycle between O and O_3 by reactions (*R2*) and (*R3*), it is convenient to define the sum of the two as a chemical family, the odd oxygen, i.e., O_x=O_3+O, which is produced by (*R1*) and consumed by the last reaction (*R4*).

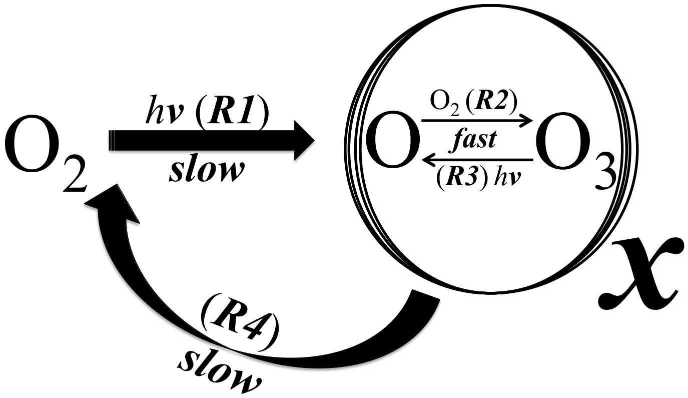

Figure 4.1 The Chapman reactions.

Using typical values for the middle latitude lower stratosphere, the lifetime for O atoms is ~0.002s [*Dessler*, 2000], i.e., it constantly being formed by photolysis of O_2 (*R1*, slow) and O_3 (*R3*, fast). The lifetime for O_3 molecules, however, is ~1000 seconds – much longer than that of O atoms. Hence, the O_x molecules, considered as a group, change slowly when O and O_3 are constantly being swapped. The abundance of O_3 is then controlled by the slow production (*R1*) and loss (*R4*) of O_x rather than by the fast production (*R2*) and loss (*R3*) of O_3. Given this, the abundances of O_3 can only change on time scales comparable to or longer than the lifetime of O_x, so conceptually it offers advantages in considering O and O_3 together as a group – the odd oxygen family.

Assuming chemical steady states, the ratio of $[O]/[O_3]$ ranges from 10^{-7} in the lower stratosphere to 10^{-2} in the upper stratosphere [*Dessler*, 2000]; i.e., virtually all of O_x is in the form of O_3 in the UTLS. This is why we applied O_x instead of O_3 production/loss in our model (see section 4.3 and 4.4).

The Chapman cycle didn't tell the full story behind the atmospheric ozone budget because it overestimates ozone by a factor of 2 or more, even though it successfully reproduced the general pattern. Considering the fact that the source from (*R1*) is well constrained by spectroscopic data, the direct conclusion would be that there must be additional sinks for O_3 that are not accounted for by the Chapman model. In fact, a close look at the Chapman cycle reveals that it only involves oxygen-containing species. A few catalytic loss cycles involving radicals HO_x [*Hampson*, 1964; *Hunt*, 1966], NO_x [*Crutzen*, 1971; Johnston, 1971], and ClO_x [*Molina and Rowland*, 1974; *Farman et al.*, 1985], which serve as essential sinks for $O_{3,}$ were discovered in the 1950s-1970s. Furthermore, the annual decrease of O_3 in the Antarctic vortex during springtime (September-November) [*Farman et al.*, 1985] makes the ozone loss not just a chemical problem but also a dynamic issue, which bewildered the science community for years.

The above highlights the complex nature of ozone, which is not captured by the simple Chapman model. In fact, people have studied those complexities chemically and dynamically for nearly a century. For our trajectory simulations, a convenient way of imposing the chemistry would be to take the ozone production and loss rates (well simulated by fully coupled chemical model) as simplified chemical module, applying to our trajectory calculations (see Sect. 3 and section 4.3, 4.4 below).

4.2.2 CO Chemistry

Carbon monoxide (CO) in the UTLS experiences less complex processes than O_3. CO is produced near the Earth's surface from the oxidation of hydrocarbons (primarily isoprene and methane) and through combustion processes such as fossil fuel and biomass burning. Its concentration is highly variable in the troposphere, ranging between 50 and 100 ppbv in uncontaminated air and increasing to at least 500 ppbv in urban or biomass-burning plumes [*Sachse et al.*, 1988; *Barnes et al.*, 2003].

Tropospheric CO can be transported into the stratosphere through deep convective penetration and large-scale diabatic uplifting (the ascending branch of the Brewer-Dobson circulation). The latter forms the famous CO "tape recorder" signal as observed by the Aura MLS [*Schoeberl et al.*, 2006].

CO can also be produced within the stratosphere as an end product of the oxidation of methane, which is initiated by reactions with either OH, atomic chlorine (Cl), or atomic oxygen in its first excited states $O(^1D)$ [summarized in *Minschwaner et al.*, 2010],

$$CH_4 + OH \rightarrow CO + products \qquad (R5)$$

$$CH_4 + Cl \rightarrow CO + products \qquad (R6)$$

$$CH_4 + O(^1D) \rightarrow CO + products \qquad (R7)$$

CO is destroyed via reaction by OH to form CO_2 [*Seiler and Junge*, 1969; *Pressman and Warneck*, 1970; *Logan et al.*, 1981],

$$OH + CO \rightarrow CO_2 + H \qquad (R8)$$

OH radical is the most efficient CO oxidant in the stratosphere. It results from the interaction of photochemically generated, excited oxygen atoms with water vapor.

The combined effects of CH_4 oxidaiton, OH removal, in addition with the transport timescale make CO showing gradual decreasing/increasing in the lower/upper UTLS. This is discussed in detail in section 4.4.3.

4.3 O_3 and CO Chemistry Hinted by Production and Loss Rates

4.3.1 O_3 Production and Loss

Now that we understand the continuity equation and the chemistry of ozone and CO, we are ready to explore the chemistry in a fully coupled chemistry climate model – the WACCM (see Sect. 2 for details of this model). Like we said, the most convenient way to understand the chemistry is to look at the chemical production and loss rates from WACCM since they represent the total net effect of chemical change explicitly hinted at from many complicated chemical and dynamical effects.

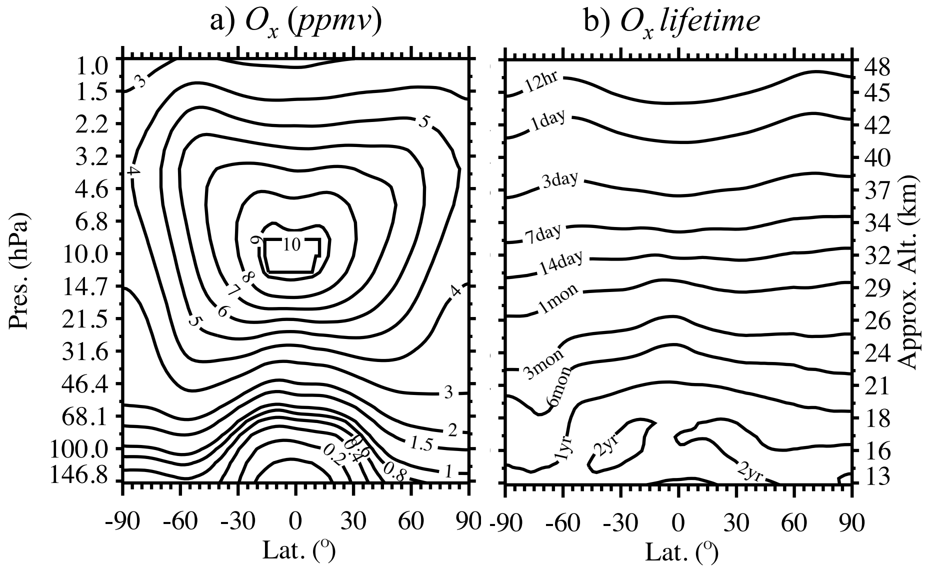

Figure 4.2. Annually zonal (a) O_x in ppmv and (b) O_x lifetime from WACCM averaged in 2005-2011. The O_x lifetime is estimated from loss rates by $[O_x]/L_{Ox}$.

Fig. 4.2 shows the WACCM simulated O_x morphology and its lifetime estimated from loss rates. In section 4.2 we explained in detail the benefit of using the odd oxygen family instead of only O_3, so from here on use O_3 and O_x interchangeably.

Fig. 4.2a shows that O_3 has the largest vertical gradient around 100-50 hPa (16-22 km). In this region, O_3 abundance jumps from a few hundred ppbv to a few ppmv. As we can see, the highest O_3 shows at tropical 10 hPa (~30 km) with ~10 ppmv, due to the competing effect of intense photolization of O_2 molecules by energetic ultraviolet radiation and a sufficient supply of O_2. Fig. 4.2b shows the lifetime of O_3 estimated from the loss rates. Apparently, O_3 has a longer lifetime in the lower stratosphere, due to both chemical and transport effects. As one goes to higher altitude, the O_3 lifetime becomes shorter. Between about 10-2 hPa (~30-40 km) the O_3 lifetime is comparable or longer than a day, so O_3 will not vary significantly during a day, therefore we say the system is in diurnal steady state. Above 2-hPa (~40 km) where the O_3 lifetime is shorter than one day – the diurnal cycle of photolysis rate, so O_3 vary during a day and displays a diurnal cycle. This is where the system reaches photochemical steady states.

Fig. 4.2 also tells us that the high abundances of O_3 in extratropical lower stratosphere cannot come from poleward and downward transport of the tropical O_3 maximum zone (30-40 km), because the lifetime of O_3 in this photochemically controlled zone is too short and it does not live long enough to be transported away further. This also serves as the finding of the overturning circulation in the stratosphere [*Brewer*, 1949].

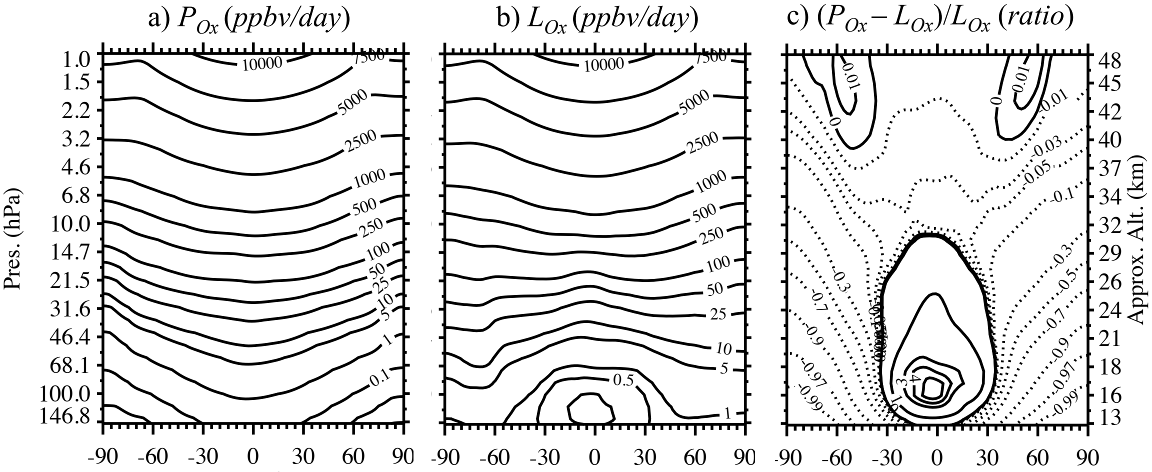

Figure 4.3. WACCM O_x (a) production rate (P_{Ox}) in ppbv/day, (b) loss rate (L_{Ox}) in ppbv/day, and (c) ratio of net rate ($P_{Ox} - L_{Ox}$) to loss rate (L_{Ox}) averaged over 2005-2011. In panel c the negative numbers are dashed to highlight the net chemical decrease and positive numbers indicate net chemical increase. Closer to zero contours indicate comparable amount of production and loss; contour lines of +1, +2, +3, etc… indicate production is 1, 2, 3 times greater than loss; contour lines of ~ -1 (lower polar stratosphere region) indicate zero production.

Fig. 4.3 shows the annual zonal mean of P_{O_x}, L_{O_x}, and the ratio of net rate ($P_{O_x} - L_{O_x}$) to loss rate (L_{O_x}) from WACCM averaged over 2005-2011. The O_x production in the stratosphere is almost entirely due to the photolysis of O_2, so $P_{O_x} \approx 2J_{O_2}[O_2]$, i.e., each O_2 molecule photolyzed produces two O_x molecules. In Fig.

4.3a P_{O_x} is greater in the tropics over higher altitudes, due to more sunlight received. P_{O_x} increases with altitude over most of the stratosphere because the photolysis rate (proportional to solar radiation) increases faster with altitude than [O_2] decreases, so the net effect is increasing. Fig. 4.3b shows that the loss rate of O_x also increases with altitude, due to the increasing abundances of O and the O_x-destroying radicals such as ClO, N_2O, OH, etc., in the stratosphere (refer to section 4.2 for details).

Fig. 4.3c shows the O_x annual zonal mean ratio of net rate ($P_{O_x} - L_{O_x}$) to the loss rate L_{O_x}, so positive numbers indicate net chemical increase and negatives indicate net decrease; while values close to zero imply balanced production and loss. It tells us that annually averaged production and loss rates are generally not equal. From 150 to 10 hPa O_x production exceeds loss in the tropics yielding a net increase, whereas a net decrease of O_3 occurs in mid- to high latitudes due to exceeds of loss to production. Transport of O_3 from the tropics to higher latitudes closes the budget and ensures a close to zero of annually averaged change of lower stratosphere O_3. Between 10-2 hPa (~30-40 km) the instantaneous production and loss of O_x become comparable. Here the lifetime of O_x is comparable to, or longer than, one day (see Fig. 4.2b) and the system is in diurnal steady state, so no significant diurnal variations of O_3 will be found. Above 2 hPa (~40 km) the system gradually reaches photochemical steady state with rapid production being balanced by rapid destruction, where the lifetime of O_x is less than one day (Fig. 4.1b) so that the abundance approximately becomes P_{O_x}/LF.

4.3.2 CO Production and Loss

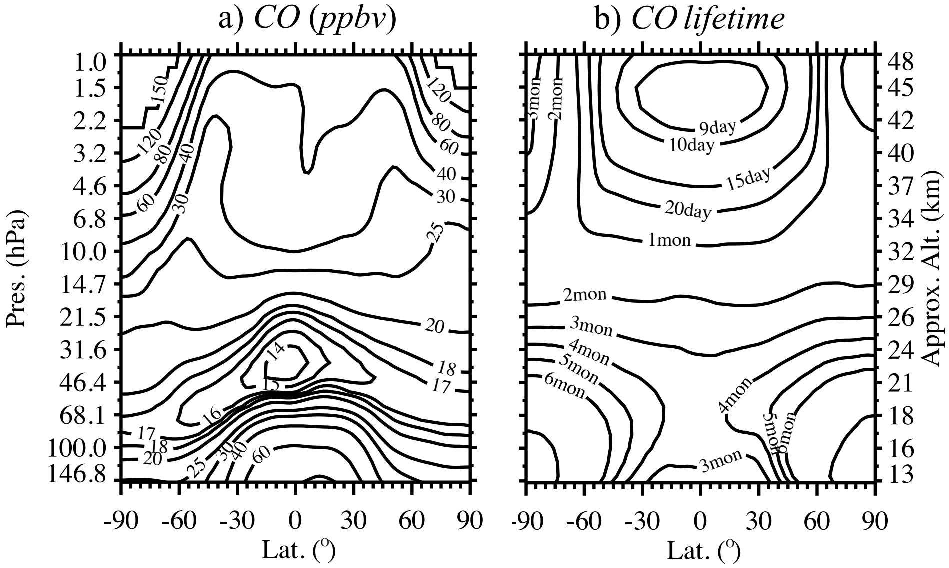

Figure 4.4. Annually zonal (a) CO in ppbv and (b) CO lifetime from WACCM averaged in 2005-2011. The CO lifetime is estimated from loss rates by $[CO]/L_{CO}$.

Fig. 4.4a shows the WACCM simulated CO morphology. Similar to O_3, CO also has its largest vertical gradient around 100-50 hPa (16-22 km), where CO experiences fundamental removal by reaction with radical OH (reaction *R8*). Fig. 4.4b depicts the CO lifetime estimated from loss rates. CO has a relatively longer lifetime in the UTLS due to transport effect – that's why it serves as a good tracer for studying transport. Whereas in the upper stratosphere, at low and mid latitudes, a minimum lifetime on the order of 10–15 days occurs at low and mid- latitudes.

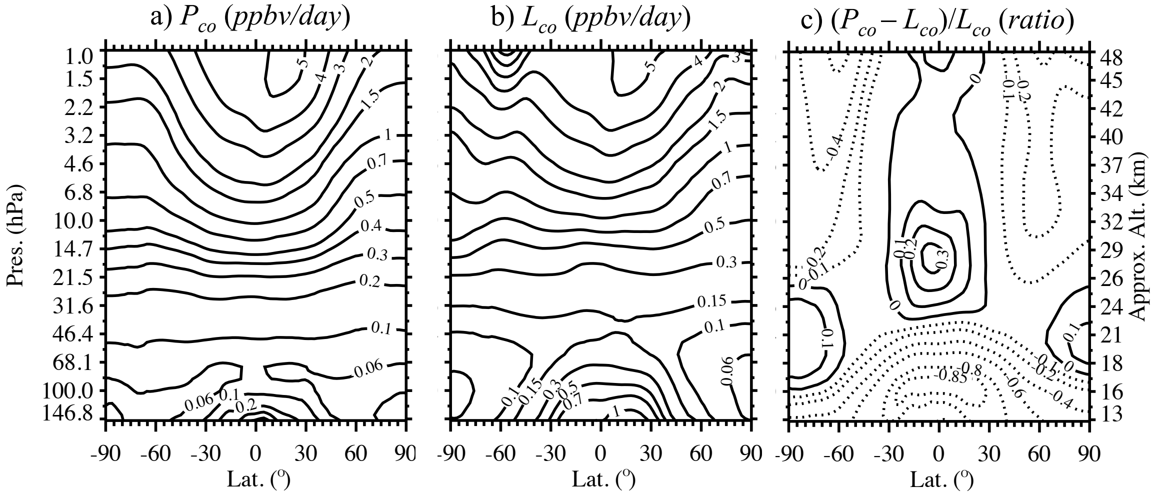

Figure 4.5. WACCM CO (a) production rate (P_{CO}) in ppbv/day, (b) loss rate (L_{CO}) in ppbv/day, and (c) ratio of net rate ($P_{CO} - L_{CO}$) to loss rate (L_{CO}) averaged over 2005-2011. In panel c the negative numbers are dashed to highlight the net chemical decrease and positive numbers indicate net chemical increase. Contours near zero indicate comparable amounts of production and loss; contour lines of close to -1 (in lower tropical stratosphere region) indicate close to zero production.

Fig. 4.5 shows the annually zonal mean of P_{CO}, L_{CO}, and the ratio of net rate ($P_{co} - L_{co}$) to L_{co} from WACCM averaged in 2005-2011. The production of CO increases with altitude in most of the stratosphere due to the combined effect of methane (CH_4) oxidation and carbon dioxide (CO_2) photodissociation. The loss rate of CO is large in the tropical lower stratosphere, where CO is predominantly removed by oxidation with OH [e.g., *Levy*, 1971; *Crutzen*, 1973]. Fig. 4.5c demonstrates that CO acts like a tropospheric source gas (major source of CO from biomass burning, forest fires, and other forms of combustions in the troposphere), with a net chemical decrease ($P_{CO} < L_{CO}$) in the UTLS, due to both OH removal and lack of sources. However, in the tropical middle stratosphere (~30 hPa) and above, the CH_4 oxidation and CO_2 photodissociation dominate yielding a net increase of CO.

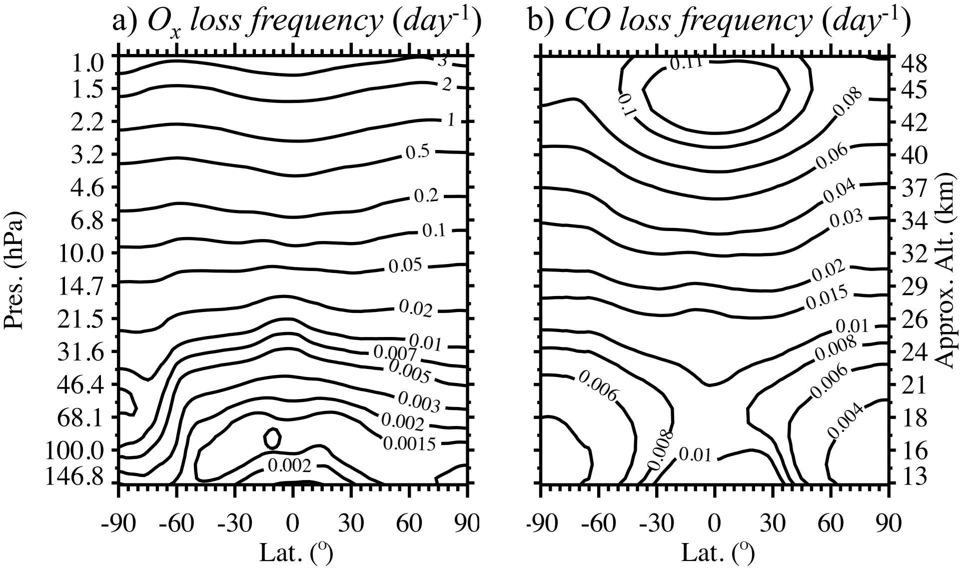

Figure 4.6. Annually zonal (a) O_x loss frequency and (b) CO loss frequency averaged from WACCM in 2005-2011. The loss frequency is estimated from chemical abundances and its loss rate, i.e., $LF_{O_x} = L_{O_x}/\ [O_x]$ and $LF_{CO} = L_{CO}/\ [CO]$.

Fig. 4.6 shows the loss frequency of O_x and CO estimated from WACCM by dividing loss rates (VMR day^{-1}) by the abundance (VMR), so the unit is day^{-1}. For O_x, The loss frequencies increase with height from the lower to upper stratosphere, indicating the fractions of current O_x to be lost. Note the similarities between this plot and Fig 4.2b (O_x lifetime). The CO loss frequency increases with altitude in most of the stratosphere. Compared to O_x loss frequency, CO loss frequency has much weaker gradients. The loss frequencies will be used in our trajectory model as the fractional loss of chemical species (see section 4.4).

4.3.3 Evaluating Transport from Production and Loss Rates

Above 30 km chemistry is much faster than the transport of O_x, yielding very large production and loss rates of similar magnitude, so that the net change is rather small. Under this backgroud state we can assume O_x is in ***steady states (ss)***. In other words, at this altitude $\partial[O_x]/\partial t \approx 0$. Therefore, we have

$$0 = \frac{\partial[O_x]_{SS}}{\partial t} = P_{O_x} - LF_{O_x}[O_x]_{SS} \tag{4.2}$$

i.e., $P_{O_x} = LF_{O_x}[O_x]_{SS}$, then

$$[O_x]_{SS} = \frac{P_{O_x}}{LF_{O_x}} = \frac{P_{O_x}}{\frac{LO_x}{[O_x]}} = \frac{P_{O_x}}{LO_x} \cdot [O_x] \tag{4.3}$$

Steady state indicates that the rate at which O_3 is being produced is equal to the rate at which it is being destroyed. It allows us to determine theoretically what the O_3 abundance would be if only photochemical processes were operating. The calculated concentrations can be compared to measurements of ozone in the atmosphere to test the accuracy of the photochemical steady-state approximation.

In the upper stratosphere, we find that observed ozone concentrations are consistent with photochemical steady-state to within the reaction rate uncertainties used in the calculations. In the lower stratosphere over the midlatitudes, we find that observed ozone concentrations are significantly higher than predicted by the photochemical steady-state calculation. This is because the time for photochemical loss is longer than the time for transport processes to bring air with high concentrations of ozone into the region. Thus, observed ozone levels remain elevated above what would be predicted from simple production/loss steady-state calculations.

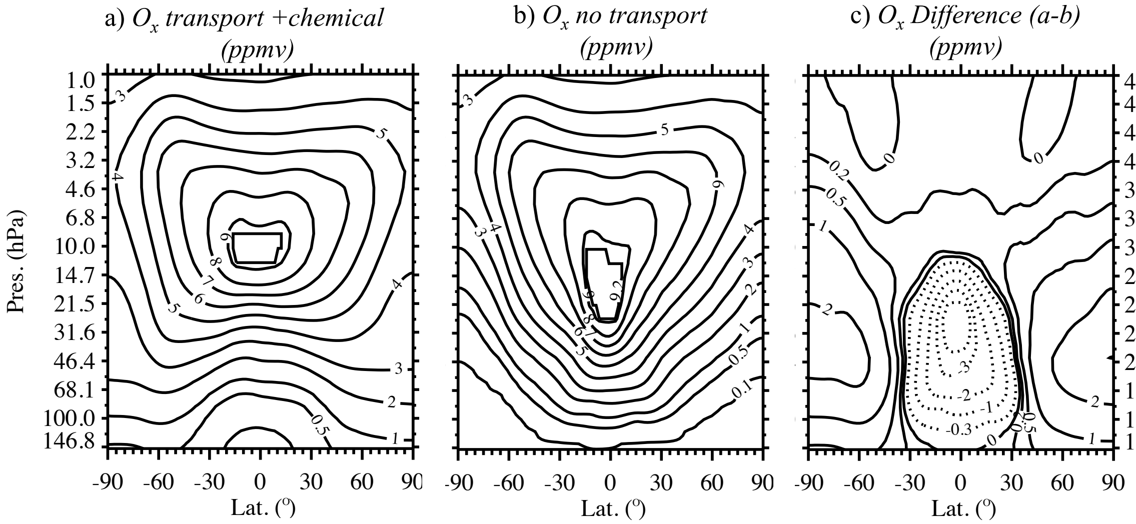

Figure 4.7. Zonally averaged (a) real atmospheric O_x ($[O_x]$), (b) O_x from pure chemical process ignoring transport process ($[O_x]_{ss}$), and (c) the differences of $[O_x]$–$[O_x]_{ss}$.

We can now address questions surrounding the difference between real O_3 and only transported O_3. Fig. 4.7 illustrates the transport effect influencing O_3 shown in WACCM. Fig. 4.7a (repeated from Fig. 4.2a) is the WACCM simulated O_3 including both chemical and transport effects (*the Transport case),* and it is close to the real observations. Fig. 4.7b shows the O_3 morphology under the ideal case when assuming steady states without transport effects (*the NoTransport case*). Fig. 4.7c shows the difference between the two. We can see that in the tropical lower and mid-stratosphere, (Transport–NoTransport) < 0, meaning the transport process tends to lower the abundances of O_x, i.e., a net transport of O_x out of this region. In mid-high latitude, (Transport–NoTransport) > 0, meaning transport of O_x tends to increase local abundances, i.e., a net transport of O_x into this region.

The transport effect can also be evaluated from the photochemical replacement time (PRT), which is defined as the time it *would* take to generate the observed chemical abundances at a specific location, under the existing production rate with no loss processes.

$$\tau = \frac{[\chi]}{P_\chi} \tag{4.4}$$

where $[\chi]$ is the concentration of a chemical species in ppbv and P_χ is the chemical production rate in ppbv/day. It is a convenient measure that helps us to determine whether photochemistry or transport is the controlling factor in determining the chemical budget at a particular location.

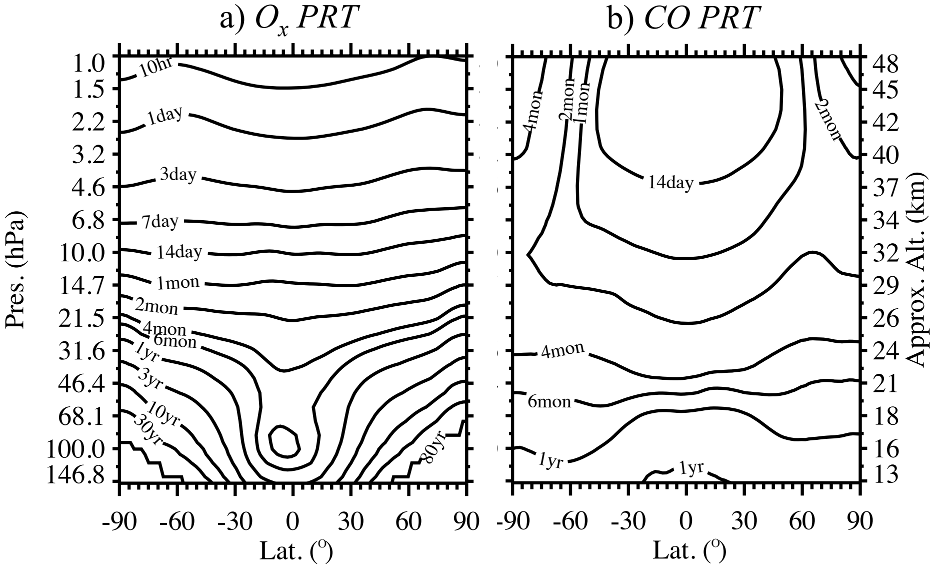

Figure 4.8. Annually zonal photochemical replacement time (PRT) for (a) O_x and (b) CO. The PRT is estimated from chemical abundances and its production rate, i.e., $PRT\chi=[\chi]/P\chi$.

Fig. 4.8 shows the PRT for both O_3 and CO. In the lower stratosphere where PRT constants are long (for both species), the chemical concentrations are strongly influenced by the transport of air into and out of that location. The transport process acts like a storing shelter that protects the chemicals from photolysis destruction. The large ozone concentrations in the lower stratosphere are a result of net transport downward and poleward from the more active photochemical region in the middle and upper stratosphere in the tropics. Again, this transport cycle is associated with the Brewer-Dobson circulation.

4.4 Trajectory Modeling of O_3 and CO in the UTLS

4.4.1 Modeling Methodology

The above shows the O_3 and CO chemistry represented in chemical production and loss rates in a Eulerian model (WACCM). The Eulerian model provides us a series of snapshots of modeled fields, which allows us to observe many interesting features of chemical species in a fixed frame. The question is that once there are some interesting features occurring, it is impossible to explore its history and future evolutions. The trajectory model, on the other hand, is able to trace parcels backward or forward for as long as needed, so it is extremely useful in transport studies. The Lagrangian (trajectory) modeling can be considered as a complimentary tool besides the Eulerian modeling.

The methodology for the trajectory simulations of O_3 and CO follows the method we used in simulating H_2O, wherein the parcels are initialized at 370-K isentrope, below the tropical tropopause, using climatological O_3 and CO from the MLS (monthly means averaged over 2005-2011) to provide approximate entry level values in the upper troposphere. The 370 K level is chosen as the initialization level because it is above the level of zero net heating rates and parcels there tend to ascend to the stratosphere.

To account for chemical changes along the trajectories, we use chemical production and loss rates (see section 4.3) output from WACCM. We treat each trajectory as a dimensionless, massless box, and it carries various chemical species. An air parcel moves with the local wind so that there is no mass exchange between the parcel and surroundings. Specifically, the O_3 and CO net change in each parcel is applied continuously with WACCM chemistry. Fig. (4.9) illustrates the basic idea. Parcel was initiated at $\vec{\boldsymbol{r}}_0$ carrying mixing ratio χ_0 observed by the MLS. At time t_1, parcels move to $\vec{\boldsymbol{r}}_1$following the wind, and we calculate the mixing ratio $\chi_1$as the results of chemical net change (P_1-L_1) at $\vec{\boldsymbol{r}}_1$ added on previous concentration χ_0. This process repeats throughout the whole integration time for each parcel.

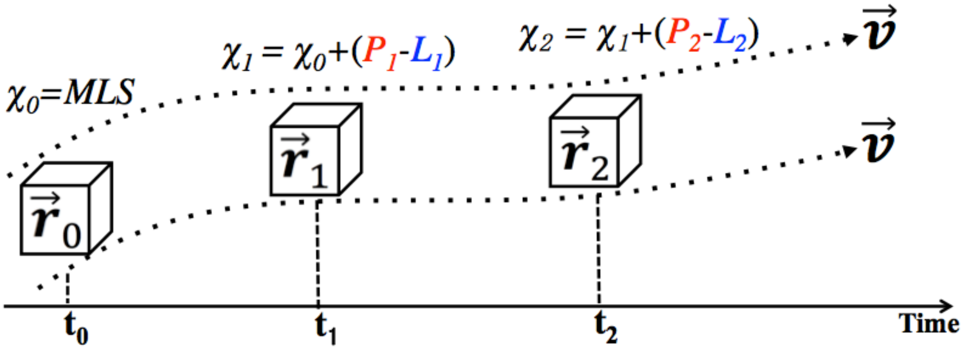

Figure 4.9. Illustration of applying the chemical production (red) and loss (blue) to the trajectories.

To be specific, the O_3 and CO concentration carried by each parcel is modified from the previous time step using the production and loss frequencies calculated from WACCM, as indicated in continuity equation,

$$[\chi]_{current} = [\chi]_{previous} + \left(P_\chi - LF_\chi \cdot [\chi]_{previous}\right) \cdot \Delta t \qquad (4.5)$$

Here, χ represents either O_3 or CO. Compare to Eqn. (4.1) we can see that the transport term – flow into and out of a box, is zero because the frame of reference is now the traveling box. Getting rid of the transport term is a major advantage of the Lagrangian trajectory model.

Eqn. (4.5) expresses that current chemical concentrations $[\chi]_{current}$ in volume mixing ratio (VMR) are determined by concentrations in previous time step $[\chi]_{previous}$ and the net change, derived from the production minus loss occurring in each time step. The production rate P_χ in VMR per unit time is obtained from WACCM. The loss rate $\left(LF_\chi \cdot [\chi]_{previous}\right)$ in VMR per unit time is calculated as a product of loss frequency LF_χ (per unit time) times the chemical concentration (VMR), representing a linear chemical loss. The loss frequencies are estimated from WACCM by dividing the model loss rate L_χ by the chemical concentration $[\chi]$, i.e., $LF_\chi = L_\chi/[\chi]$. In our simulation P_χ and LF_χ are calculated from WACCM as a function of latitude, altitude, and time (climatological months).

Like we explained in Sect. 2, upwelling across the tropical tropopause in the trajectory model is determined by the reanalysis diabatic heating rates (Q), and our simulations of O_3 and CO are sensitive to the imposed upwelling (as shown below). There is substantial uncertainty in the detailed magnitude and spatial structure of Q, as seen in the differences among separate reanalysis results (*Schoeberl et al., 2012*; *Randel and Jensen*, 2013; *Wright and Fueglistaler*, 2013; also refer Fig. 2.6 in Sect. 2 and Fig. 3.7 in Sect. 3). Fig. 4.10 illustrates the differences in Q in the tropics (15° N-S) based on several reanalysis data sets, highlighting large differences in the UTLS. Given this uncertainty, we tested the sensitivity of our calculations to variations in the heating rates by comparing results based on the MERRA (*Rienecker et al.*, 2011) and the ERA Interim reanalysis (*Dee et al.*, 2011).

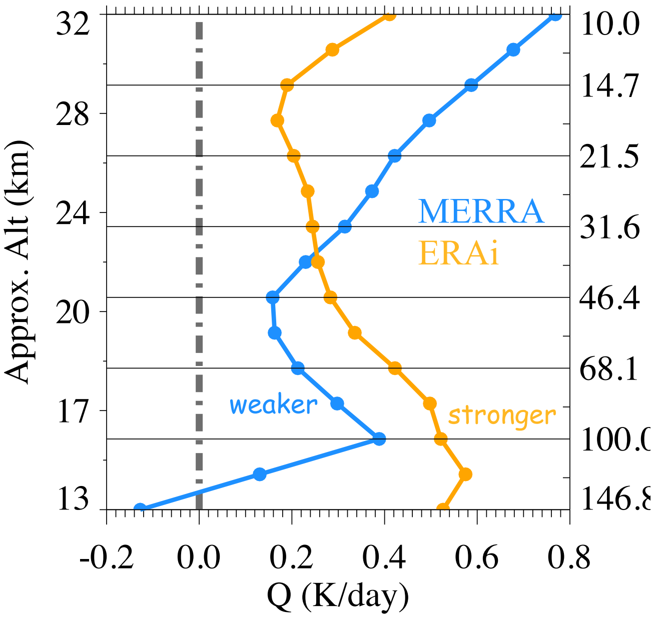

Figure 4.10. Comparison of diabatic heating rates averaged over the deep tropics (18^o N-S) in 2000-2010 from different reanalysis data sets: MER (MERRA, blue) and ERAi (ECMWF ERA interim, orange).

Having circulation (horizontal winds and vertical velocities deduced from Q) of reanalyses and chemistry from WACCM ready, we are ready to put them together into our trajectory models. Below we highlight the sensitivity of the resulting O_3 and CO simulations to the different circulations imposed. We use "TRAJ_MER" and "TRAJ_ERAi" to represent trajectory results driven by MERRA and ERAi circulation, respectively. To evaluate the results, we compare them with O_3 and CO from MLS observation and WACCM Eulerian model.

4.4.2 Ozone Results

Fig. 4.11 shows the zonal mean cross section of O_3 during December-February (DJF) and June-August (JJA) from the trajectory model driven by MERRA reanalysis (denoted as "TRAJ_MER"), compared to both the MLS observations and the WACCM results.

Because O_3 above 10 hPa is in photochemical steady-state (see section 4.3) we focus on O_3 below 10 hPa. Overall trajectory simulations agree with results from both observation and chemical model. The enhanced O_3 production due to photolysis at 30 km (~10 hPa) shifts from south during DJF towards north during JJA, following the seasonal variations of photolysis rates. The normalized distribution patterns from trajectory model show correlation coefficients of 0.97-0.98 with MLS in both seasons.

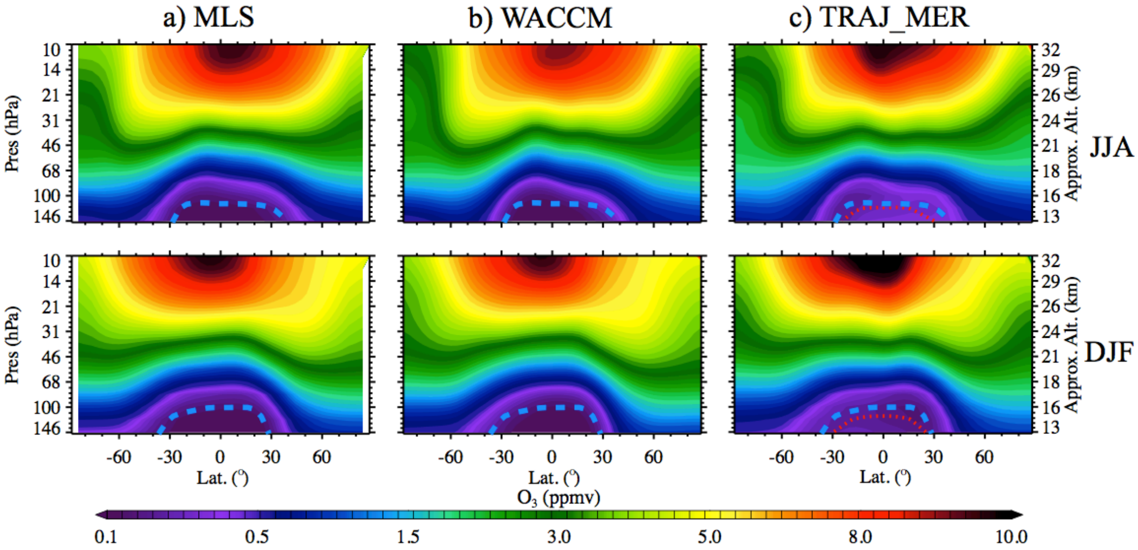

Figure 4.11. Trajectory modeled O_3 driven by MERRA reanalysis wind (column c, TRAJ_MER) in boreal winter (DJF, lower row) and summer (JJA, upper row), compared to both MLS observations (column a) and WACCM output (column b). The dashed blue curve marks the tropopause, and the dashed red line in column c marks the 370-K isentrope where parcels are initialized.

Fig. 4.11 verifies our understanding of ozone that in the upper stratosphere, the seasonal variability of ozone concentrations is driven by the seasonal variation in temperature acting through temperature dependent photochemistry. In the lower stratosphere, photochemistry is much slower owing to reduced UV flux. This makes the time scale for ozone loss longer than the time to move air from one place to another. This means that in the lower stratosphere, the amount of ozone at any one place depends on where the air came from and how much ozone was contained in that air. In another word, variability at these altitudes is more dependent on transport processes than on photochemical ones, so transport of ozone by large-scale circulations becomes important (as shown in Fig. 4.7c).

Vertical profiles of O_3 averaged over the deep tropics (18^{o} N-S) from 2005 to 2011 are shown in Fig. 4.12a. The trajectory model driven by MERRA shows reasonable agreement with MLS data (and WACCM) in the lower stratosphere, while the results based on ERAi (denoted as “TRAJ_ERAi”) show smaller O_3 values. Above 24 km where photochemical processes dominate, different trajectory runs yield similar results and they both agree with MLS and WACCM data. Note that the MERRA and ERAi simulations use identical O_3 initial values at 370 K, so that the differences in Fig. 412a are primarily a result of differences in upward circulation (Fig. 4.10). The mean differences in ozone in the lower stratosphere can be explained as a result of the different heating rates imposed. The ERAi heating rates are higher than MERRA up to 20 km (Fig. 4.10; *Schoeberl et al.*, 2013). Due to positive vertical gradient in O_3 the stronger circulation moves air with lower O_3 upward, creating a lower relative concentration compared to MERRA.

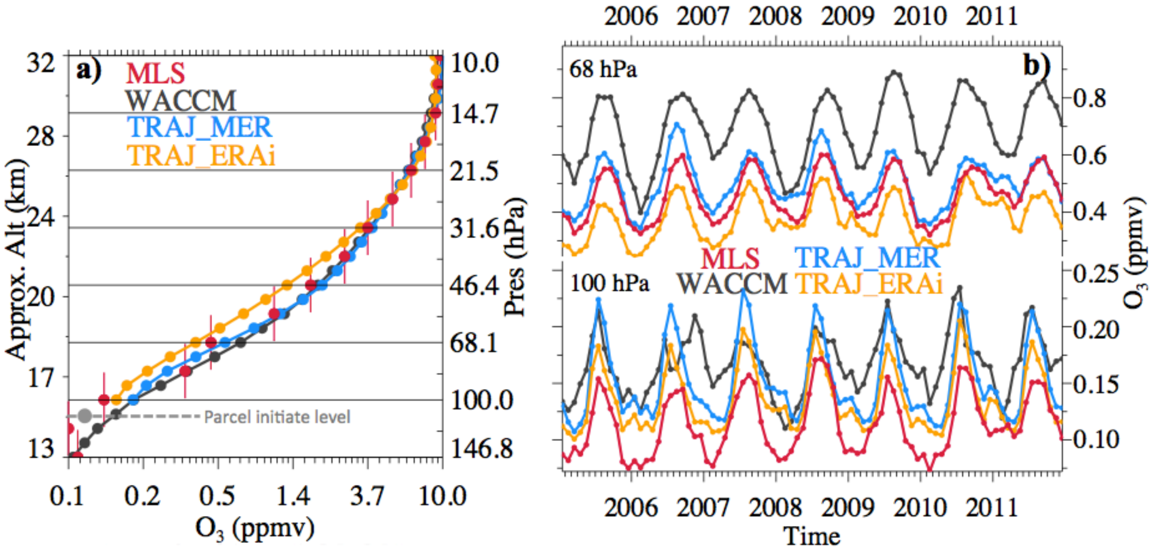

Figure 4.12. Tropical (a) vertical profile and (b) time series (100 hPa, bottom panel; 68 hPa, upper panel) of MLS (red), WACCM (black), and trajectory modeled O_3 driven by MERRA wind (blue, TRAJ_MER) and ERAi wind (orange, TRAJ_ERAi), averaged over the deep tropics (18^o N-S) from 2005 to 2011. In panel (a) the grey dot highlights the O_3 concentration initialized to parcels, and the 370-K isentrope is marked in gray dashed line to emphasize the initialization level. Vertical bars in red (panel a) indicate the MLS vertical resolutions in kilometers at each of the MLS retrieval pressure levels.

Monthly time series of O_3 at 100 hPa and 68 hPa averaged over the deep tropics (18^o N-S) are shown in Fig. 4.12b. At 100 hPa our results are slightly higher (0.04-0.08 ppmv) than the MLS, which is not surprising because MLS O_3 at this level has a 20-30% (0.04-0.06 ppmv) uncertainty. There is a strong annual cycle in ozone at these levels related to the seasonal variations in tropical upwelling (*Randel et al.*, 2007; *Abalos et al.*, 2012, 2013a), and this behavior is reproduced by the trajectory model, showing reasonable agreement in amplitude with the MLS observations and WACCM results. There are somewhat larger differences in annual cycle amplitude at 68 hPa, with the MERRA trajectory results showing better agreement with MLS, whereas WACCM shows O_3 about 40-70% higher.

For trajectory results, even though the absolute value slightly differ from that of the MLS, the departure from mean indeed show better consistency with MLS, i.e., the annual cycle of O_3 is well resolved in our model. However, WACCM O_3 shows larger peak-to-peak amplitude.

The simulated and observed latitudinal structure of zonal mean O_3 in the lower stratosphere (68 hPa) throughout the seasonal cycle is shown in Fig. 4.13. The overall variations are reasonably well simulated by the trajectory model, although low biases are found compared to MLS and WACCM over middle-to-high latitudes in both hemispheres. The development of the Antarctic ozone hole is evident in the very low ozone values polewards of 60^o S in October – starting from August, the South Pole undergoes exceptional depletion of O_3 from ~2.3 ppmv to as low as ~0.1 ppmv in October. This is simulated in the trajectory model based on the strong chemical ozone losses in this region derived from WACCM.

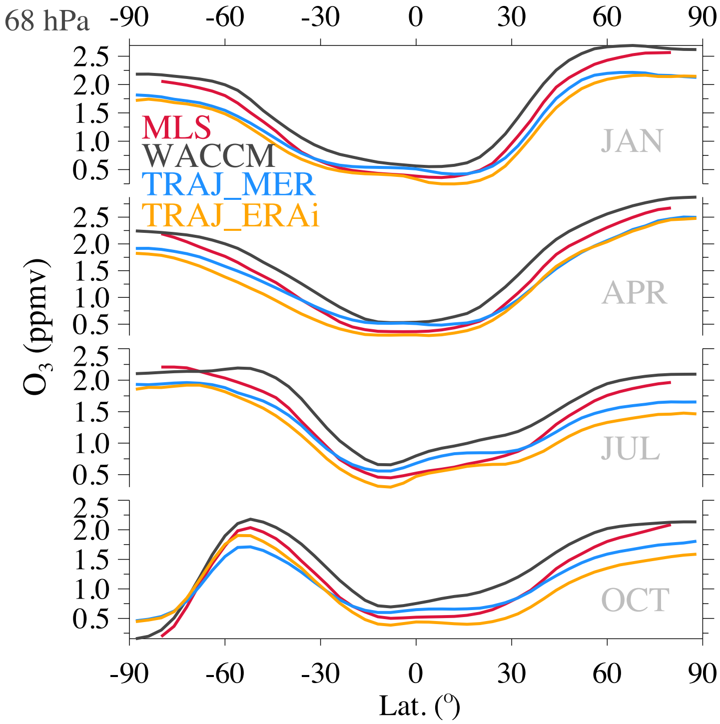

Figure 4.13. Zonal mean of O_3 at 68-hPa during January (JAN), April (APR), July (JUL), and October (OCT) averaged in 2005-2011 from MLS (red), WACCM (black), and trajectory driven by MERRA wind (blue, TRAJ_MER) and ERAi wind (orange, TRAJ_ERAi). In October (Antarctic spring time), the South Pole undergoes exceptional depletion of O_3.

Fig. 4.14 compares the horizontal structure of boreal summer (JJA) O_3 at 83 hPa from MLS data and the trajectory results driven by MERRA. The trajectory simulation shows a reasonable simulation of the spatial patterns compared to MLS (and WACCM; not shown), with a clear minimum inside the Asian monsoon anticyclone linked to upward transport of ozone-poor air from lower levels [*Park et al.*, 2009]. There is also relatively low O_3 centered near 15° S linked to the slow ascending air from the troposphere in this region.

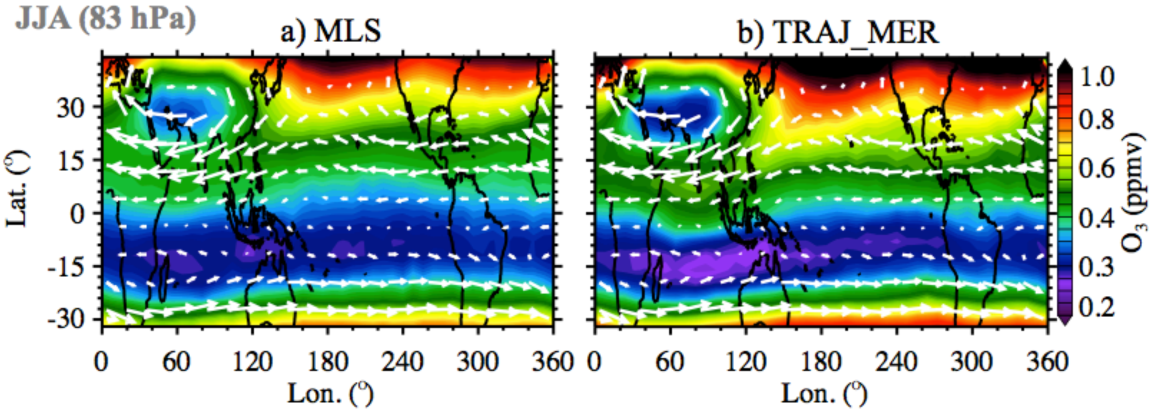

Figure 4.14. Summertime (JJA) tropical O_3 distributions at 83 hPa averaged from 2005 to 2011 between MLS and MERRA driven (TRAJ_MER) trajectory simulations. Horizontal wind vectors from the MERRA reanalysis are overlaid to emphasis the Asian summer monsoon anticyclone.

The trajectory model is also able to capture the spatial behavior of polar ozone. Fig. 4.15 shows a comparison of high latitude O_3 in northern hemisphere (NH) during winter (DJF) and in southern hemisphere (SH) during spring (September) between MLS and trajectory modeling driven by MERRA winds. During NH winter, O_3 rich air (>2.2 ppmv) occurs within the polar vortex (denoted with the 25 PVU isopleth in Fig. 7a-b), and the trajectory model captures the observed isolation from middle latitudes. WACCM shows similar pattern (not shown here) but with 0.4 ppmv higher O_3 on average in the vortex. During SH springtime, the Antarctic ozone hole (denoted with the 195 K isotherm in Fig. 4.15c-d) is reasonably well reproduced in the trajectory model based on imposed WACCM chemistry. The trajectory model also captures the spatial structure of the zonal wave ozone maximum near 50° S (the so-called 'ozone croissant'), linked to the descending branch of the BD circulation, although the magnitude is weaker than observed (see also Fig. 4.13). The weaker extra-vortex high in ozone in the trajectory model may be related to the weaker overall circulation in MERRA compared to observations (*Schoeberl et al.*, 2013). WACCM results, on the other hand, shows O_3 ~0.3 ppmv higher here, probably due to the vertical transport, too.

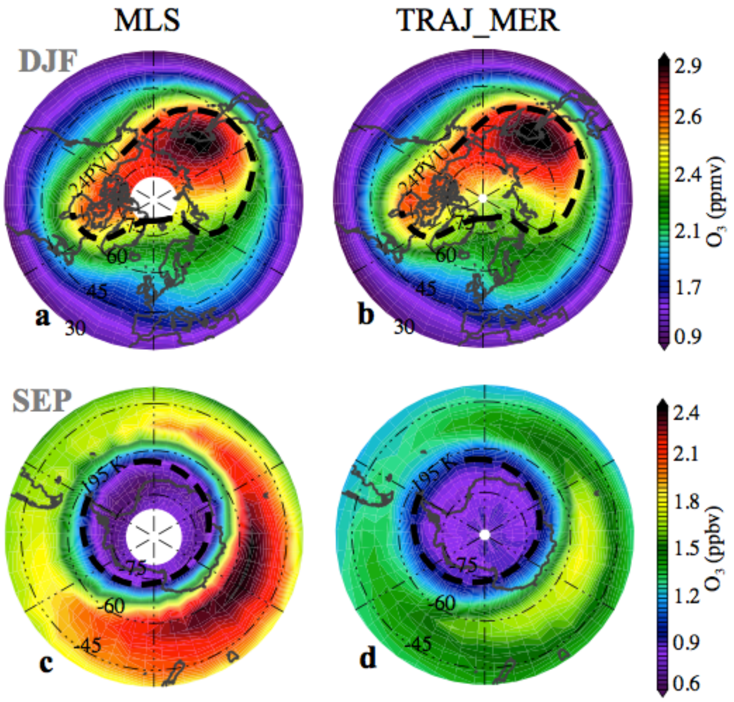

Figure 4.15. Polar O_3 distributions shown in MLS (left column) and trajectory results driven by MERRA (TRAJ_MER, right column) during North Hemisphere winter (DJF, panel a and b) and South Hemisphere spring (September, SEP, panel c and d) at 68 hPa. The 24-PVU potential vortices (panel a-b) and the 195-K temperature (panel c-d) are overlaid in black dashed lines for both seasons, respectively.

4.4.3 CO Results

Figure 4.16 shows that zonal mean cross sections of CO from ACE-FTS, WACCM, and the trajectory model agree well in the lower stratosphere. CO is a maximum in the tropical upper troposphere, and decreases with altitude to a minimum near 22 km. Above this altitude, CO increases again.

This is because in the tropical UTLS CO production from CH_4 oxidation is negligible due to slow destruction of CH_4 (lifetime is on the order of years). Here the primary sink for CO is reaction with OH. As CO-rich air is brought up through the TTL, it is slowly destroyed by OH (timescale of a few months). Meanwhile, the upwelling in this altitude is also quite slow (~2-3 km in a few months), so that the CO decreases with height for the first 5 km or so above the tropopause.

Above about 25 km, however, CH_4 can be oxidized fast by OH, Cl, and O (^{1}D) to make CO (section 4.2 *R5*-*R7*), so CO shows an increase with height. Although the OH destruction reaction continues to operate on CO, this is more than balanced out by increasing production from CH_4.

Fig. 4.16 also shows a distinctly high CO mixing ratios in the polar middle and upper stratosphere regions in ACE-FTS observation, which results from the downward transport of CO from the mesosphere (from photodisassociation of CO_2) mostly occur during winter at high latitudes; this behavior is also seen (to a weaker degree) in WACCM, but is not simulated in the trajectory model, which does not include mesospheric processes.

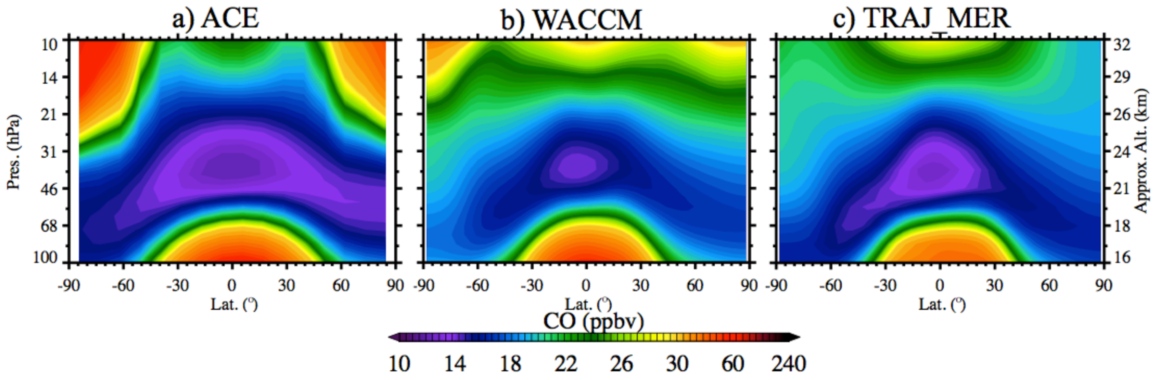

Figure 4.16. Zonal mean cross sections of CO from (a) ACE-FTS, (b) WACCM, and (c) trajectory model driven by MERRA reanalysis (TRAJ_MER).

The photodisassociation of carbon dioxide (CO_2) is a major source of CO in the mesosphere (see below reaction *R9*). As a results primarily of CO2 photodisassociation, there exist a large reservoir of CO in the upper mesosphere and lower thermosphere (75-100 km) that can be transported downward to lower altitudes, for example, during periods of strong descent at high latitudes during winter [*Solomon et al.*, 1985; *Allen et al.*, 2000]

$$CO_2 + h\nu \rightarrow CO + O \qquad (R9)$$

To demonstrate how the CO rich air in mesosphere affects the stratosphere and why the trajectory simulation fails in the upper stratosphere, here we compare annual evolutions of WACCM and trajectory CO extended to 0.01 hPa (~80 km, close to the top of mesosphere). The downward transport primarily happens in high latitude, so in Fig. 4.17 we only compare the polar region. On the left (Fig. 4.17a, c), WACCM CO increases by an order of magnitude from the stratosphere to the mesosphere, with enhancements due to photodissociation of CO_2 follow the variations of solar radiation. Then the consecutive downward motion brings large amount of CO down to the polar stratosphere, inducing a sharp gradient in CO concentrations (*Solomon, et al.*, 1985). On the right (Fig. 4.17b, d), lack of a large reservoir of CO in the trajectory mesosphere and lower thermosphere makes the downward intrusion of CO rich air to the upper stratosphere impossible, which creates unrealistic gradients and low concentrations in CO. This is why the discrepancies exist in CO trajectory simulations. Even though, in lower to middle stratosphere trajectory model still produces reasonably good results.

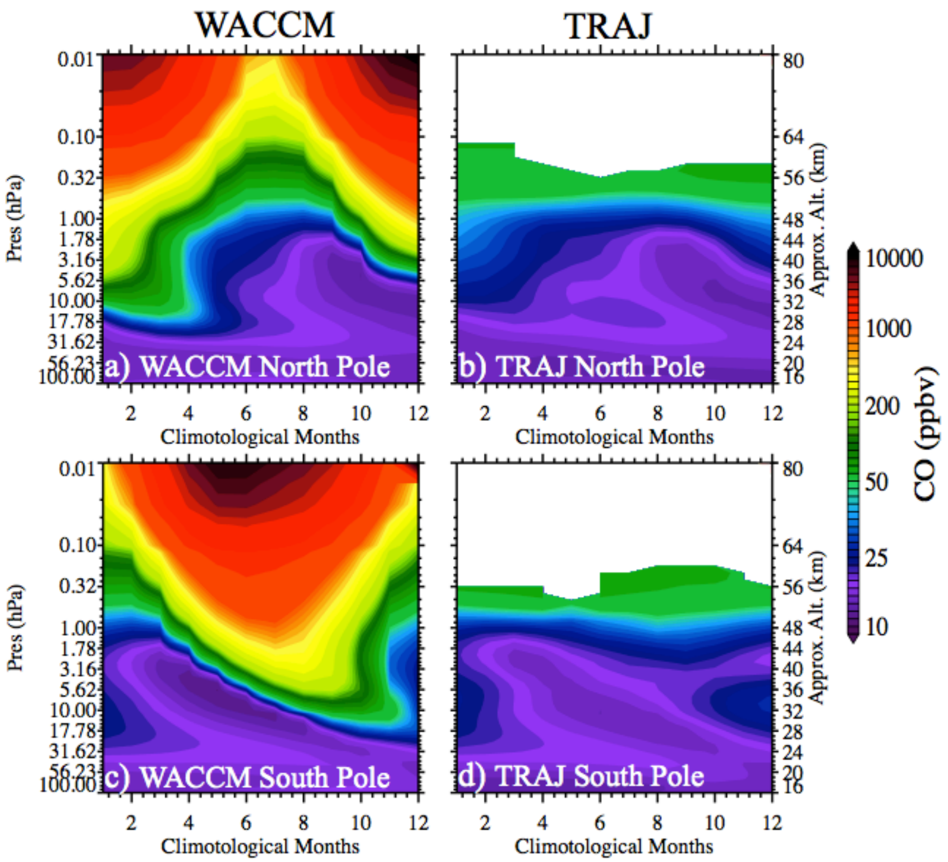

Figure 4.17. Seasonal evolutions of CO from WACCM (a, c) compared to that from trajectory modeling (c, d) in both North Pole (upper row) and South Pole (lower row). The vertical scale is extended to 0.01 hPa (~80 km) to highlight the lack of transports of mesosphere CO rich air to the stratosphere.

Figure 4.18 shows the CO vertical profiles and time series averaged in the deep tropics (15^o N-S). The vertical profiles in Fig. 4.18a show broad-scale agreements, although there are differences among the trajectory models (with ERAi driven results larger than those driven by MERRA) and also between the ACE-FTS and MLS observations. Time series of CO at 100 hPa (Fig. 4.18b) show a semi-annual cycle linked to initialized variations in the upper troposphere (*Liu et al.*, 2007), with approximate agreement among the models and observations (with slightly larger values in the MLS data). The variability changes to an annual cycle at 68 hPa, as a response to variations in tropical upwelling. At 68 hPa there are relatively larger differences in the seasonal cycle of CO between the MERRA and ERAi trajectory calculations, with the ERAi results showing better agreement with MLS and ACE-FTS data.

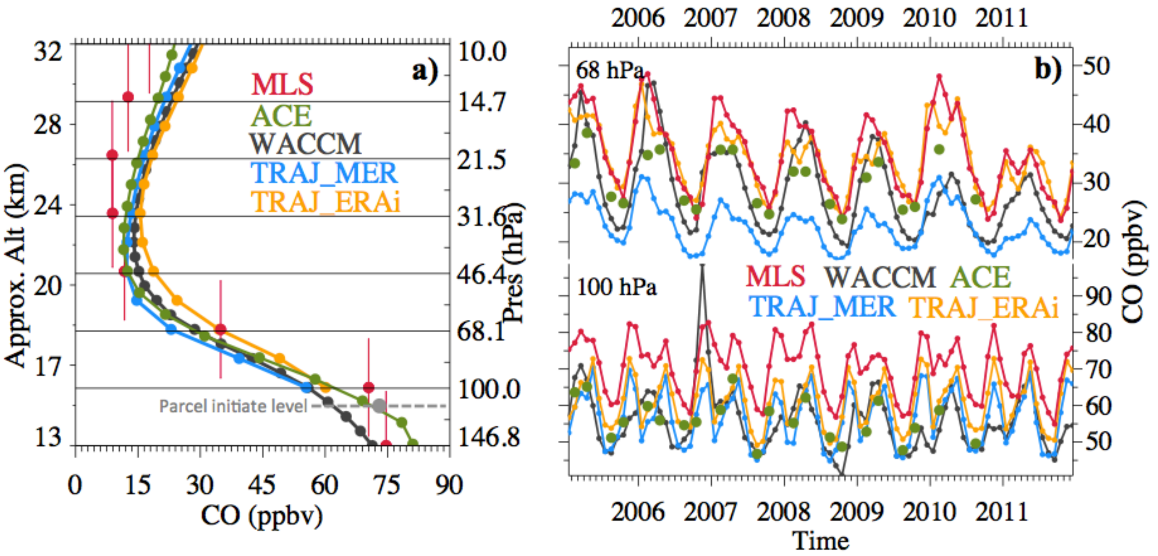

Figure 4.18. Tropical (a) vertical profile and (b) time series (100 hPa, bottom panel; 68 hPa, upper panel) of MLS (red), WACCM (black), ACE (green), and trajectory modeled CO driven by MERRA wind (blue, TRAJ_MER) and ERAi wind (orange, TRAJ_ERAi), averaged over 18° N-S from 2005 to 2011. In panel (a) the grey dot highlights the O_3 concentration initialized to parcels, and the 370-K isentrope is marked in gray dashed line to emphasize the initialization level. Vertical bars in red (panel a) indicate the MLS vertical resolutions in kilometers at each of the MLS retrieval pressure levels.

A further diagnostic to evaluate the model simulations is made by plotting monthly tropical (15° N-S) averages of O_3 vs. CO in the lower stratosphere (68 hPa), as shown in Fig. 4.19. This includes the observations from MLS, together with trajectory model simulations driven by both MERRA and ERAi, which shows the sensitivity to different Q (see also Fig. 4.10), and also the WACCM model results as a reference.

There is an overall anti-correlation between O_3 and CO in Fig. 4.18, mainly representing the out-of-phase annual cycles seen in Figs. 4.12b and 4.18b. The anti-correlation is caused by the different signs of vertical gradients in O_3 ($\nabla > 0$) and CO

($\nabla < 0$). The comparisons in Fig. 4.18 show that stronger upwelling in the ERAi simulation yields slightly lower values of O_3 (<0.3 ppmv) and higher values of CO (>30 ppbv), and vice versa.

This tracer-upwelling relation is quite easy to understand when we combine upwelling (Fig. 4.10) with chemical change ratio (Fig. 4.3c and Fig. 4.5c) together. Stronger upwelling (ERAi) results in faster transport, i.e., parcels' residence time (τ) within the UTLS is shorter. Remember that O_3 in the UTLS region experiences net increase (Fig. 4.3c), so shorter residence time τ means less increase (or "gain") of O_3, therefore the trajectory modeling driven by ERAi yields lower O_3. Similarly, weaker upwelling (MERRA) makes parcels transport within the UTLS slower, so they stay longer. Recall that CO in the UTLS experience net decrease (removed by OH and no extra source, Fig. 4.5c), thus, longer stay helps parcel decrease more, yielding lower CO. This result keeps reminding us the dominant role of tropical upwelling in controlling species with strong vertical gradients near the tropical tropopause.

The slopes for MLS, WACCM, MERRA driven trajectory, and ERAi driven trajectory are -66.1, -41.2, -37.3, and -52.0, respectively, which shows that the best overall fit to the observations at 68 hPa is from ERAi driven trajectory results. WACCM results, on the other hand, show overall 30-50% higher O_3 and 20% lower CO, probably due to the less accurate vertical motion in WACCM [*Abalos et al.*, 2013a].

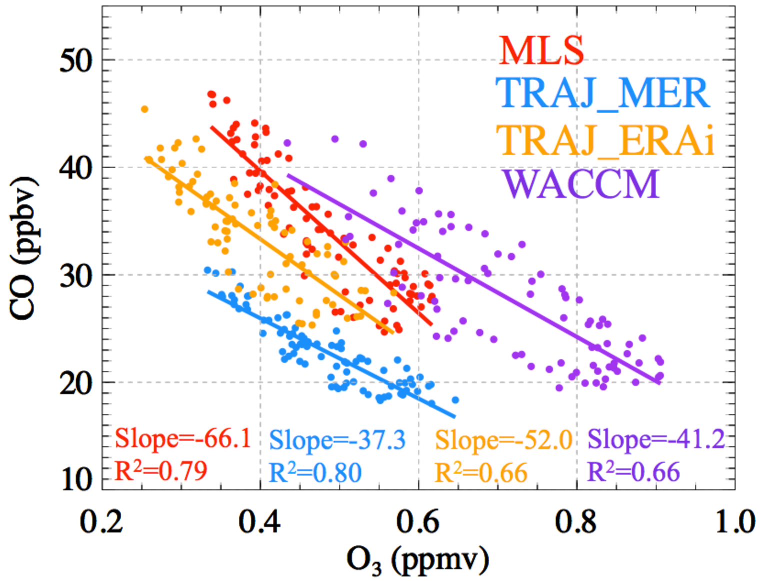

Figure 4.19. Monthly variations of O_3 vs. CO in the tropical lower stratosphere (15^o N-S, 68 hPa) from MLS (red) and trajectory modeling driven by MERRA wind (blue, TRAJ_MER) and ERAi wind (orange, TRAJ_ERAi), and WACCM (purple). The slopes are -66.1, -37.3, -52.0 (ppbv/ppmv), respectively.

The DJF and JJA seasonal distributions of CO at 68 hPa from the ERAi trajectory model are compared to MLS data in Fig. 4.20. In both seasons the trajectory model shows spatial patterns consistent with MLS data. During DJF the patterns show a center of high CO over Central America and enhancements over South East Asia, extending to the tropical western Pacific (largely attributable to fossil fuel emissions, *Jiang et al.*, 2007). The trajectory model also captures the well-known CO maximum linked to the Asian monsoon anticyclone during JJA, which is substantially stronger at the 100 hPa level [e.g, *Randel and Park*, 2006; *Park et al.*, 2009; *Randel et al.*, 2010].

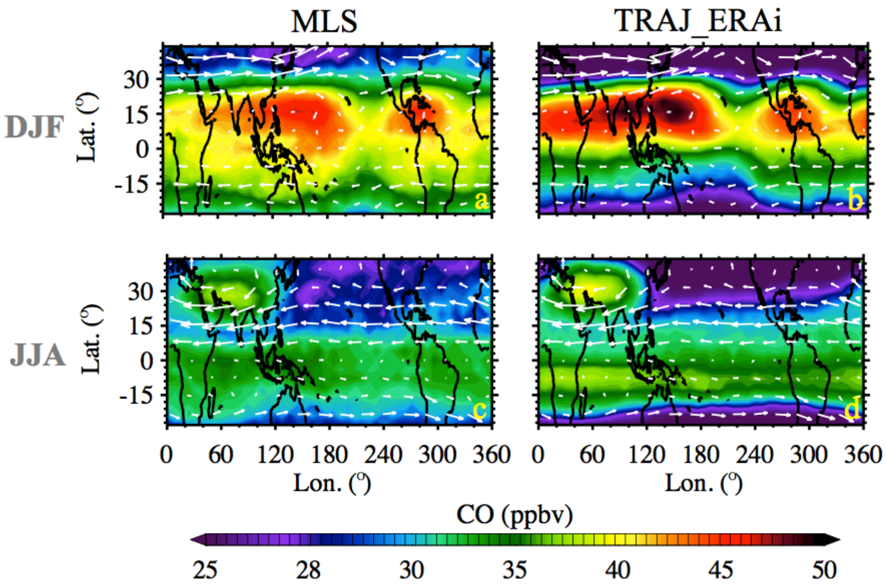

Figure 4.20. Comparison of CO at 68 hPa (~ 20 km) during DJF (top row, a and b) and JJA (bottom row, c and d) between MLS (left) and trajectory modeling driven by ERAi wind (right, TRAJ_ERAi). Horizontal wind vectors from ERAi are overlaid as reference.

Overall, the large-scale seasonal behavior of CO simulated by the trajectory model is in agreement with both observations (MLS and ACE-FTS) and Eulerian chemical model (WACCM), although the results are sensitive to the tropical upwelling speed.

4.5 Interannual Variability of Tracers in the Tropical Lower Stratosphere (LS)

4.5.1 Tracer-Tracer Relation

The coherent seasonal variations in O_3 and CO in the tropical LS demonstrate that transport processes have a large impact on the chemical concentrations in this region. The Eulerian-mean calculations of *Abalos et al.* [2012, 2013a] show that tropical upwelling is the main driver of the annual cycles in O_3 and CO above the tropical tropopause. Our Lagrangian trajectory model results (Figs. 4.12b and 4.18b) also show that the annual cycles of O_3 and CO above the tropopause (especially around 70 hPa) are strongly influenced by the tropical upwelling (Brewer-Dobson) circulation.

We further explore interannual variations in the chemical tracers and links to changes in the upwelling circulation. Fig. 4.21 shows the interannual anomalies (by removing the annual cycle) in O_3 and CO concentrations in the tropical lower stratosphere from MLS observations and from trajectory calculations, and in addition anomalies in diabatic heating rates (upwelling) from reanalysis at 68 hPa. While there are significant differences in time-mean diabatic heating rates between MERRA and ERAi (Fig. 4.10), interannual changes in Q (Fig. 4.21c) show good agreement. Fig. 4.21 shows that interannual anomalies in O_3 and CO are strongly anti-correlated (due to oppositely signed vertical gradient) and closely linked to interannual changes in diabatic heating. Furthermore, Fig. 4.21 shows that trajectory calculations driven by both MERRA and ERAi are able to simulate the observed interannual anomalies in O_3 and CO, in spite of significant differences for the background seasonal cycle (Fig. 4.12b and 4.18b).

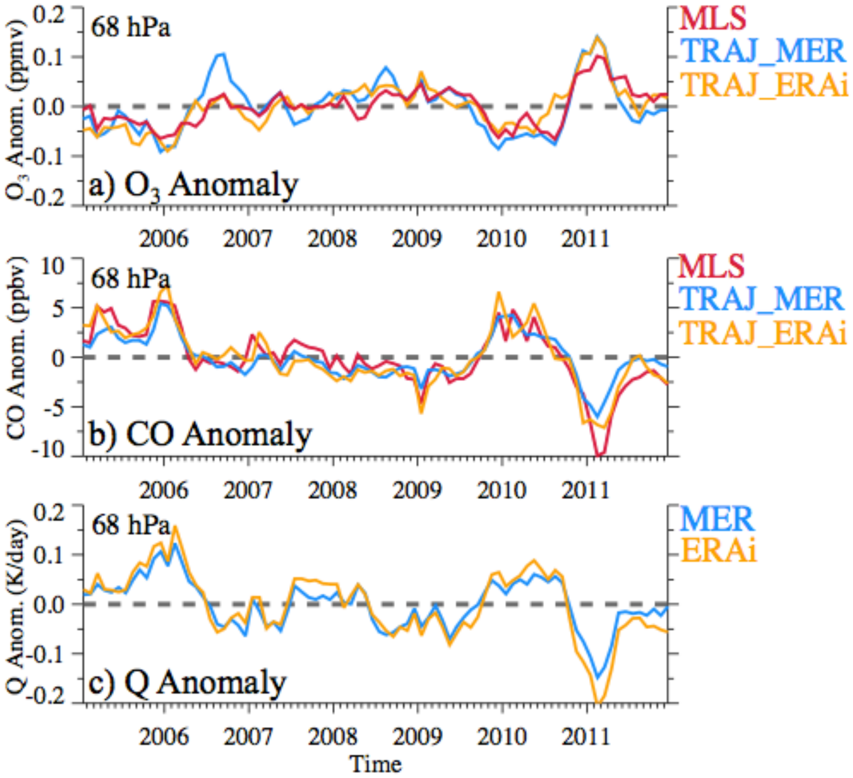

Figure 4.21. Interannual anomalies of (a) O_3 and (b) CO from MLS (red) and trajectory simulations driven by MERRA (blue, TRAJ_MER) and ERAi (orange, TRAJ_ERAi) in the tropical (15° N-S) lower stratosphere (68 hPa), consistent with (c) the variations of total diabatic heating rates from MERRA (blue) and ERAi (orange), which serves in our model as the vertical velocity.

Taking the results from MERRA run as an example, the close relationship between anomalies in diabatic heating and O_3 is quantified in Fig. 4.22a, which shows strong anti-correlation due to different signs of vertical gradient, with explained variance r^2=0.79 and slope $\Delta O_3/\Delta Q$ = -0.91±0.10 (ppmv)/(K/day). Similar strong correlation is found for CO and Q anomalies (Fig. 4.22b), with explained variance r^2=0.76 and slope of 41.41±5.09 (ppbv)/(K/day). These strong relationships between diabatic heating (Q) and tracer anomalies highlight the dominant role of tropical upwelling in controlling species with strong vertical gradients near the tropical tropopause.

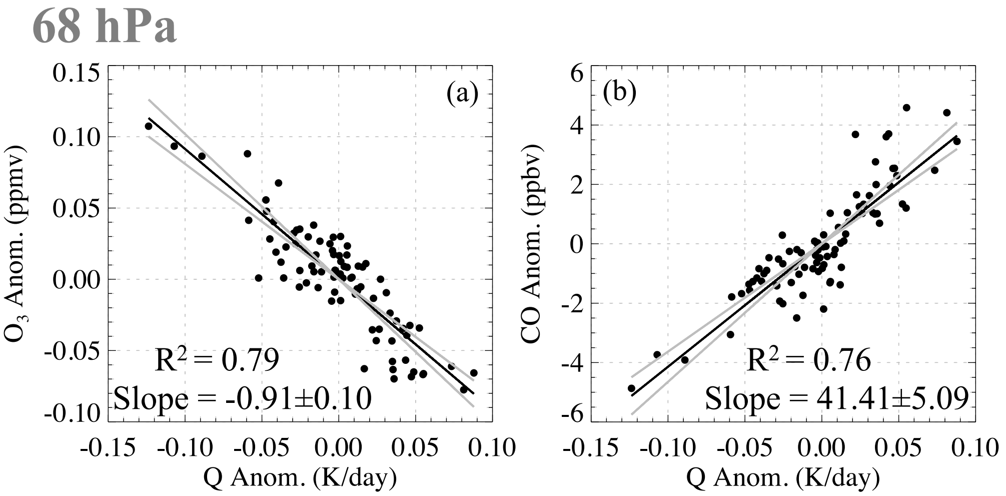

Figure 4.22. Scatter plots of the anomalies of (a) O_3 vs. Q and (b) CO vs. Q. The dots are monthly variations and the black lines show the linear fit.

Fig. 4.21 and 4.22 highlights strong anti-correlations between O_3 and CO anomalies, which is further demonstrated in Fig. 4.23. Following the zonal mean tracer mixing ratio continuity equations in the Transformed Eulerian Mean (TEM) formalism [*Andrews et al.*, 1987], we have

$$\frac{\partial \bar{\chi}}{\partial t} = -\bar{v}^* \frac{\partial \bar{\chi}}{\partial \phi} - \bar{w}^* \frac{\partial \bar{\chi}}{\partial z} + \nabla \cdot \boldsymbol{M} + P - L \qquad (4.6)$$

Here, $\bar{\chi}$ is the zonal mean mixing ratio of the tracer; $\bar{v}^*$is the mean meridional velocity; $\bar{w}^*$is the vertical component of the residual circulation; $\nabla \cdot \boldsymbol{M}$ is the eddy transport term; (P-L) is the net chemical change. Averaging over the tropics, it states that the changes in tracer concentrations arise from the combined effects of meridional and vertical advection by the residual mean circulation (i.e., mean meridional transport and upwelling acting on the background vertical gradient), eddy transport, and chemical sources/sinks.

Assuming the idealized case when upwelling dominates tracer transports, i.e., meridional advection, eddy transport, and chemical sources/sinks are negligible, then Eqn. (4.6) can be expressed as

$$\frac{\partial \bar{\chi}}{\partial t} \approx -\bar{w}^* \frac{\partial \bar{\chi}}{\partial z} \qquad (4.7)$$

Abalos et al. [2012] have shown that the ratio of tendencies for two tracers (χ_1, χ_2) is closely related to the ratio of the respective background gradients:

$$\frac{\partial \bar{\chi}_1}{\partial t} / \frac{\partial \bar{\chi}_2}{\partial t} = \frac{\partial \bar{\chi}_1}{\partial z} / \frac{\partial \bar{\chi}_2}{\partial z} \sim constant \qquad (4.8)$$

i.e., the ratio of chemical tendencies should be related by the ratios of their respective background vertical gradients, which can also be treated as constant.

Integrating this equation in time for monthly O_3 and CO anomalies gives the relationship:

$$\Delta\overline{O_3} / \Delta\overline{CO} \approx \frac{\partial \overline{O_3}}{\partial z} / \frac{\partial \overline{CO}}{\partial z} \qquad (4.9)$$

i.e. the ratio of monthly anomalies approximately follows the ratio of background vertical gradients for the idealized situation where vertical transport is dominant. For the case of CO and O_3 in the tropics near 68 hPa, the MERRA trajectory results yields a background gradient ratio of ~ -30.6 (ppbv/km)/(ppmv/km) for (dCO/dz) / (dO_3/dz). A linear fit of the observed CO/O_3 anomalies (Fig. 4.22c) gives a ratio of -41.0±4.6 (ppbv/ppmv), which is close to the idealized result (slightly outside of the two-sigma uncertainty). This approximate agreement with highly idealized theory provides further evidence for the control of tropical lower stratosphere O_3 and CO by variations in upwelling.

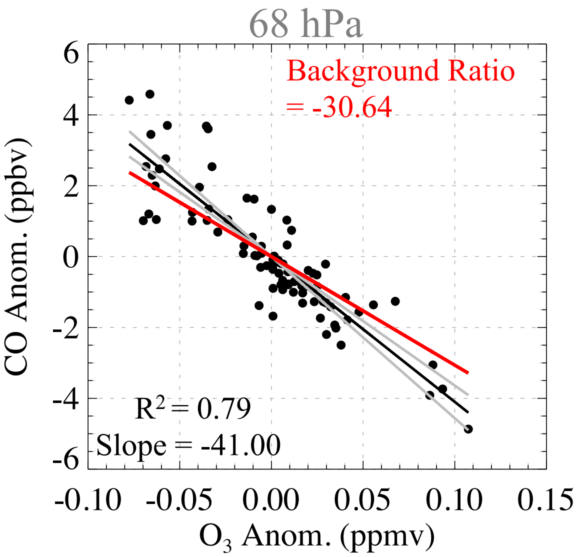

Figure 4.23. Scatter plots of the anomalies of CO vs. O_3. The dots are monthly variations and the black lines show the linear fit, i.e. the left-hand side of (4.9). The red line is the theoretically estimated slope using simplified relation in Eq. (4.9), i.e., the right-hand side.

4.5.2 Tracer-Temperature Relation

Besides tracer variations, *Randel et al*. [2002] and *Abalos et al*. [2012] also showed that the temperature annual cycle (peaking near 70 hPa) and tropical upwelling are closely related. It is also known that the tropical atmospheric circulation does not respond directly to vertically integrated heating, which approximately corresponds to total surface precipitation in convective regions, but to the vertical gradient of diabatic heating. In order to quantify the relations of tracers to tropical upwelling we use the similar method in *Abalos et al*. [2012] and section 4.5.1 to evaluate the relations of tracer to the vertical gradients of diabatic heating above the tropopause using trajectory pure Lagrangian results.

Following the zonal mean thermodynamic equation in the Transformed Eulerian Mean (TEM) formalism [*Andrews et al*., 1987],

$$\frac{\partial \bar{T}}{\partial t} = -\bar{v}^* \frac{1}{a}\frac{\partial \bar{T}}{\partial \phi} - \bar{w}^* S + \bar{Q} + \left\{ -\frac{1}{e^{-\frac{z}{H}}}\frac{\partial}{\partial z}[e^{-\frac{z}{H}}(\overline{v'T'}\frac{\frac{\partial \bar{T}}{\partial \phi}}{a \cdot S} + \overline{w'T'})] \right\} \qquad (4.10)$$

Here, $\bar{T}$ is the zonal mean temperature tendency; $\bar{w}*$ is the vertical component of the residual circulation; $\bar{Q}$ is the zonal mean diabatic heating rates. $S = \frac{\partial \bar{T}}{\partial z} + \frac{\kappa}{H}\bar{T}$ is the static stability parameter in functions of scale height H, temperature vertical gradients, and $\kappa = R_d/c_p$ with dry air constant *Rd* and heat capacity c_p. In the middle atmosphere a scale height of 7 km is a good approximation. The big term within braces is the eddy term. The rest of the notations are the same as in *Andrews et al.* [1987].

Now, assuming idealized case where vertical velocity and diabatic heating rates dominate the thermodynamic equation so that meridional advection and eddy transport terms can be ignored, it yields a simplified relation

$$\frac{\partial \bar{T}}{\partial t} = -\bar{w}^* S + \bar{Q} \qquad (4.11)$$

Eqn. (4.11) can be expressed in terms of potential temperature and diabatic heating rates as

$$-\bar{\boldsymbol{v}} \cdot \nabla\bar{\theta} = -\bar{w}^* S' \qquad (4.12)$$

when combining

$$\bar{T} = \bar{\theta} e^{-\frac{\kappa z}{H}} \qquad (4.13)$$

$$\bar{Q} = \frac{d\bar{\theta}}{dt} e^{-\frac{\kappa z}{H}} \qquad (4.14)$$

where $S' = S \cdot e^{\frac{\kappa z}{H}}$, and subscripts *t* and *z* refer to local derivative with respect to *t* and *z*, respectively. $-\bar{\boldsymbol{v}} \cdot \nabla\bar{\theta} = -(\frac{d\bar{\theta}}{\partial t} - \frac{\partial\bar{\theta}}{\partial t}) = -(\bar{Q} \cdot e^{\frac{\kappa z}{H}} - \frac{\partial\bar{\theta}}{\partial t})$ is the advection term of potential temperature. Given the above approximation this term only has a vertical term, which is directly related to the vertical gradients of diabatic heating rates. So we simply call it the diabatic heating term in this equation. Noted that Eqn. 4.14 is the first law of thermodynamics, and $\frac{d\bar{\theta}}{dt}$ is used in trajectory model as the cross-isentrope vertical velocity.

Equation (4.12) directly relates both diabatic heating rates with static stability to vertical transport. Combing with Eqn. (4.7), we have a new set of dominating equations.

$$\begin{cases} -\bar{\boldsymbol{v}} \cdot \nabla\bar{\theta} = -\bar{w}^{*}S' \\ \bar{\chi}_t = -\bar{w}^{*}\bar{\chi}_z \end{cases} \tag{4.15}$$

From Eqn. (4.16), if vertical transport dominates the below relation holds

$$-\bar{\boldsymbol{v}} \cdot \frac{\nabla\bar{\theta}}{\bar{\chi}_t} = \frac{S'}{\bar{\chi}_z} \sim constant \tag{4.16}$$

which means that in the transport dominated region the ratio of heating gradients to chemical tendencies should be related to the ratios of stability to the chemical vertical gradients. Given that the static stability and tracer vertical gradients are nearly stationary on interannual timescales, the ratio can be considered as constant.

Fig. 4.24 proves that equation (4.16) holds also for Lagrangian results and the tropical upwelling is indeed the dominant control of chemical mixing ratios. For example, Fig. 4.24a shows that from a long-term perspective every 1 K increase in heating rates vertically will result in ~11.69 ppbv increase of O_3 within a month; and under transport-dominant approximation the theoretical increase of O_3 would be 11.60 ppbv – very close to what the data shows, and therefore upwelling motion played a very important role in determining the O_3 concentrations. The same story holds for the variations of CO and diabatic heating rates.

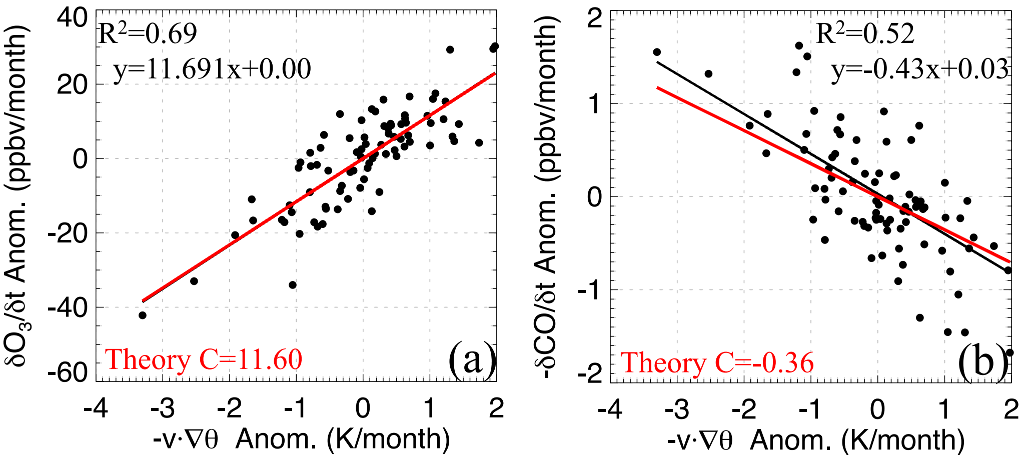

Figure 4.24. Scatter diagrams of O_3 (a) and CO (b) tendencies versus diabatic heating at 68 hPa. The dots are monthly variations and the black lines show the linear fit, i.e., the left-hand side of Eqn. (4.16). The red lines are the theoretically estimated slopes of simplified relation in Eq. (4.16), i.e., the right-hand side.

Overall the trajectory modeled chemical tendencies show strong correlation to the variations of diabatic heating rates and tracer-to-tracer tendencies are also closely related. Those relations can be accounted for very well in a highly idealized approximation where upwelling is the dominant mechanism for seasonal variability. Different from the trajectory analysis performed by *Konopka et al.* [2009, 2010] and *Ploeger et al.* [2012], our trajectory model is purely Lagrangian calculations – each trajectory is completely independent of its surrounding parcels, and the only mixing only occurs at the end when they are gridded. The fact that our Lagrangian results are consistent with Eulerian analysis by *Randel et al.* [2007] and *Abalos et al.* [2012] proves that horizontal in-mixing (horizontal transport) is unlikely responsible for seasonal cycle of ozone but upwelling is. Therefore we propose further discussion of Konopka and Ploeger's study.

4.6 Summary

This Section focuses on the chemical simulations of using trajectory model. Contents in this section have been submitted to ACP, currently in public discussion. The chemical production and loss rates from fully coupled chemical climate model summarize the chemical behaviors without digging into many details of chemical and dynamical aspect of the atmosphere. They are easy to understand and easy to use. It tells us that O_3 experience net increase within the UTLS (Fig. 4.3c), whereas CO experiences net decrease (Fig. 4.5c)

The trajectory simulations of O_3 and CO from imposed WACCM chemistry are complementary to modeling H_2O (mainly controlled by tropopause temperature) in that O_3 and CO rely on both initial conditions and chemical production and loss rates, and are sensitive to transport. Initial conditions based on observations provide entry values of chemical species into the lower stratosphere; after that the chemical production and loss control the net changes of concentrations along the trajectories.

Trajectory modeled O_3 and CO in the tropical lower stratosphere largely depend on the strength of upwelling (and to a lesser degree on the amount of mixing with extratropics [*Abalos et al.*, 2013a]). Stronger upwelling is linked to faster transport, which results in less time for chemical production (for O_3) or loss (for CO), leading to lower values of O_3 and higher values of CO. The comparisons of MERRA and ERAi simulations (which have very different tropical upwelling rates, e.g. Fig. 4.10) clearly demonstrate this sensitivity.

Although better agreement with observations of CO in the tropical lower stratosphere are found using ERAi data, there is reason to suspect that the ERAi diabatic heating in this region may be too high [*Ploeger et al.*, 2012]. In any case, the trajectory modeled O_3 shows reasonable simulation of the large-scale seasonal structure compared to both MLS and WACCM, including both the tropics and the Polar Regions. The trajectory modeled CO in the tropical stratosphere is more sensitive to the MERRA vs. ERAi differences, likely because of the shorter photochemical lifetime of CO in the lower stratosphere compared to O_3.

The annual cycles in O_3 and CO in the tropical lower stratosphere are reproduced in the trajectory model simulations, and the magnitude of variations provides a useful test of the imposed circulation. The variability of O_3 and CO shows significant correlations with fluctuations in diabatic heating, for both seasonal and interannual time scales. These close relationships support the concept that tropical upwelling plays a key role in regulating variability for chemical species with strong vertical gradients in the lower stratosphere (and explains the observed compact relationships among interannual anomalies in diabatic heating, O_3 and CO seen in Figs. 4.21-4.22). For the idealized situation where upwelling dominates tracer transports, the tracer ratios can be expressed as ratios of the background vertical gradients, and the observed O_3 and CO changes are in approximate agreement with this expectation (Fig. 4.23). The similar conclusion could be reached for the tracer vs. temperature, too, as shown in Fig. 4.24.

The discussions above linking seasonal or interannual changes in O_3 and CO with chemical changes along slower or faster upward trajectories is a Lagrangian perspective on transport (appropriate for our Lagrangian trajectory model). In contrast, the discussions linking O_3 and CO variations at particular pressure levels to a varying circulation acting on background vertical gradients is an Eulerian perspective. These two perspectives are complementary and do not contradict each other; *Abalos et al.* [2013b] have recently shown the equivalence of Lagrangian and Eulerian transport calculations in the tropical lower stratosphere, highlighting that each can provide useful information.

Our simulations with O_3 and CO have demonstrated the viability of the domain-filling forward trajectory model for simulating species with relatively simple chemistry in the UTLS, and extension to other species would be straightforward. There are several potential applications for such a trajectory model, including describing parcel histories that characterize different transport pathways, and evaluating the importance of tropical-extratropical exchanges. For example, trajectories can allow tracing the sources of CO-rich air in the summertime Asian monsoon region, and quantifying the fate of the parcels after breakup of the anticyclone. The model can also allow detailed comparisons of transport based on different and new reanalysis data sets, or idealized studies of the chemical responses to UTLS circulation in a changing climate.

5. SUMMARY AND FUTURE WORK

5.1 Summary of Results

The domain-filling, forward trajectory model is useful for studying the transport of water vapor (H_2O) and chemical trace gases (such as O_3 and CO) in the UTLS. It is easy to use, easy to diagnose, and the Lagrangian perspective makes it exceptionally useful in studying transport processes within the UTLS.

The modeling of H_2O is mainly controlled by tropopause temperature, so that the final value of H_2O in trajectory calculations is insensitive to the initial condition provided is it above ~20 ppmv. Besides temperature, the model results are also sensitive to the upward motion implied by diabatic heating rates. We performed trajectory runs driven by three state-of-the-art reanalyses (MERRA, ERAi, and NCEP CFSR) and found that they can all reproduce basic features of stratospheric water vapor, but with quantitative differences mainly caused by somewhat different temperatures and diabatic heating in reanalyses (Sect. 2&3). It turns out that the cold biased ERAi temperature creates ~0.5-0.8 ppmv drier air, whereas the warm biased CFSR temperature creates a 0.7-1.1 ppmv wetter air around the tropopause. The ~30% too strong heating rates in ERAi yields a faster transport of the water vapor – approximately 3 months ahead of the observation; the slower transport implied from MERRA or CFSR run yields a ~2 month lag at higher altitude.

During the trajectory integration, using reanalysis temperature results in a bimodal FDP (final dehydration points) distribution due to limited model levels in reanalysis, although the predicted stratospheric H_2O agrees with observations [*Schoeberl and Dessler* 2011; *Schoeberl et al.*, 2012, 2013]. Instead of using reanalysis temperature, using GPS RO temperature in very fine vertical resolution gives a more realistic dehydration pattern while keeping the predicted stratospheric H_2O correct (Sect. 3).

The O_3 and CO simulations rely on initial conditions, chemical production and loss rates, and are sensitive to transport. Initial conditions based on observations provide entry values of chemical species into the lower stratosphere; after that the chemical production and loss control the net changes of concentration along the trajectories. Trajectory modeled O_3 and CO in the tropical lower stratosphere largely depend on the strength of upwelling (and to a lesser degree on the amount of mixing with extratropics [*Abalos et al.*, 2013a]). Stronger upwelling is linked to faster transport, which results in less time for chemical production (for O_3) or loss (for CO), leading to lower values of O_3 and higher values of CO. The comparisons of MERRA and ERAi simulations (which have very different tropical upwelling rates) clearly demonstrate this sensitivity. We also conducted a sensitivity study of increasing MERRA diabatic heating rates (Q) by constant factors, and the best overall fit to the observations is 1.5 times the MERRA Q values (see Fig. 5.1 below), which further supports the theory.

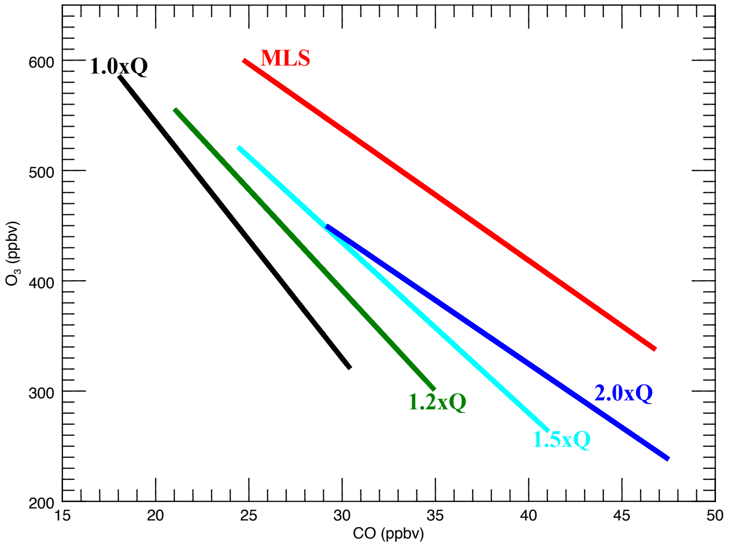

Figure 5.1. Monthly variations of O_3 vs. CO in the tropical lower stratosphere (15^o N-S, 68 hPa) from MLS (red) and trajectory modeling driven by MERRA winds and original (black), 1.2 times (green), 1.5 times (cyan), and 2.0 times (blue) of diabatic heating rates.

The variability of O_3 and CO shows significant correlations with fluctuations in diabatic heating, for both seasonal and interannual time scales. These close relationships support the concept that tropical upwelling plays a key role in regulating variability for chemical species with strong vertical gradients in the lower stratosphere (and explains the observed compact relationships among interannual anomalies in diabatic heating, O_3 and CO). For the idealized situation where upwelling dominates tracer transports, the tracer ratios can be expressed as ratios of the background vertical gradients, and the observed O_3 and CO changes are in approximate agreement with this expectation.

5.2 Future Work

5.2.1 Tracer Transport in the Middleworld

a) Diagnose of Tracer Transport in The Lowermost Stratosphere

Our model is able to reproduce trace gases such as H_2O, O_3, and CO in the UTLS very well. The results in Sect. 3 and 4 have been mostly focused on the stratospheric overworld, where air is stratospheric at all latitudes and faster and seasonally dependent meridional transport occurs. The other important part of the UTLS is essentially the stratospheric middlewrold (lowermost stratosphere, LMS), where downward max flux prevails and tropospheric air and stratospheric air exchange rapidly via adiabatic motion. Here, the recycling of stratospheric air back into the TTL is potentially important (e.g., *Sherwood*, 2000; *Read et al.*, 2008; *Konopka et al.*, 2009).

Transport in the lowermost stratosphere requires consideration of the details of synoptic-scale and small-scale processes and how they link to the overworld. With the unique feature of determining the history and future evolutions of air mass, trajectory model serves as a perfect tool in studying the budget of trace gases in the TTL and the LMS. Like we have shown in Sect. 4, we can learn more about origin of the seasonal cycle of tracers. We can also determine the fractions of air descending from the overworld back to the LMS, the fluxes of air transported quasi-horizontally between the tropical upper troposphere and the LMS. With these we can determine when and where transport occurs and what is the dominating mechanism that affects the fluxes.

b) Asian Monsoon Affects the Stratosphere – Tracer Perspective

The relative abundances of H_2O, O_3, and CO are unique during the summertime Asian Monsoon region: H_2O tends to be high due to relatively warm temperature; CO tends to be high due to transport from polluted boundary layer; and O_3 tends to be low due to isolation from the O_3-rich stratosphere. Those all indicate an isolation of the Asian Monsoon from the wider stratosphere, and accordingly, this region can be treated as another important path for pollutants transport into the stratosphere [*Randel et al.*, 2010].

Combining the trajectory modeling of those tracers, we hope to gain an insight into the air moving through the Asian Monsoon and hopefully to understand how the Asian Monsoon affects the stratosphere quantitatively. For example, trajectories can allow the sources of CO-rich air to be traced in the summertime Asian monsoon region (Sect. 4). Quantifying the fate of the parcels after anticyclone breakup is also possible. This compliments the earlier study by *Bergman et al.* [2013] that used back trajectories to follow the Monsoon flow to the surface.

5.2.2 Modeling TTL Cirrus Cloud Formation

Dehydration has been explored carefully and thoroughly in our work [Sect. 3; *Schoeberl et al.*, 2011; *Schoeberl et al.*, 2012, 2013]. Since cloud is a direct product of freezing, we intend to include a simple microphysical scheme that allows ice condensation (freezing and forming clouds) and evaporation (back to vapor) occurring in the model. Because of the limited water vapor and very low temperature in the TTL, clouds formed from large-scale freezing and drying should be very thin, with ice limited by local water vapor availability [*Wang and Dessler*, 2012]. Those ice clouds in the TTL are referred to as TTL cirrus that frequently extend hundreds to more than a thousand kilometers horizontally and persist for hours or even days [*Winker and Trepte*, 1998; *McFarquhar et al.*, 2000; *Dinh et al.*, 2010]. TTL cirrus can thus profoundly impact the radiative budget of the TTL [e.g., *Rosenfield et al.*, 1998; *Jensen et al.*, 1996].

Previously *Jensen and Pfister* [2004] used a one-dimensional trajectory model to simulate ice cloud formation in the TTL. In their model a very detailed microphysical scheme is applied, which includes the wave perturbation, the crystal growing speed, crystal size distributions, etc. Since dehydration is primarily responsible for cloud formation in the TTL, is the detailed microphysics important? We propose to include a simple scheme allowing cloud formation in our model to determine if the microphysics in the TTL and stratosphere is indeed of great importance.

The adjusted model work as follows: along the trajectory calculations, instead of simply removing excess water vapor instantaneously, we transfer them gradually into ice with a selected e-folding time of τ_C, whereas in the sub-saturated case ice is evaporates with an e-folding time of τ_E, to contribute vapor abundances. The e-folding time for condensation is a measure of how fast the excess vapor condenses. It is easy to understand: shorter τ_C results in faster vapor condensation, and more ice can be formed. This enables us to keep track of both water vapor and ice within the parcel and the ice could serve as an indication of where and when clouds form. We consider those trajectories that have ice content greater than 0.1 *ppmv* as "detectable clouds". In verification, we compare the cloud measurements by the Cloud-Aerosol Lidar and Infrared Pathfinder Satellite Observations (CALIPSO).

Fig. 5.2 shows the cloud observation by CALIPSO and simulation by our model at two altitudes from 2007 to 2011. In each panel, we scaled the cloud count from 0 to 1 with minimum count to be 0 and maximum count to be 1. We can see that the general pattern is quite similar between the two. During boreal winter, our model predicts clouds in three of the most enhanced regions close to that of the CALIPSO observation. During boreal summer, clouds mostly occur in the Asian monsoon and the South Pole (where the clouds are called Polar Stratospheric Cloud).

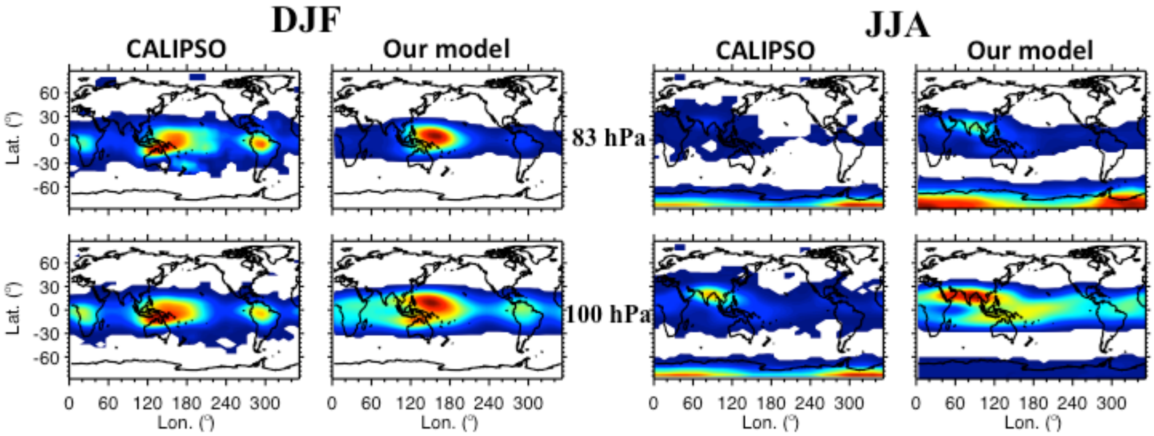

Figure 5.2. Cloud distribution from CALIPSO and our model from 2007 to 2011. For easy comparison, we scaled cloud count in each panel to be from 0 to 1.

Fig. 5.3 shows the evolution of tropical clouds (30^{o} N-S) at 100 and 83 hPa. Again, the cloud count in CALIPSO and our model are scaled from zero to one for easy comparison. Our cloud prediction shows encouraging agreement with the observations. However, there are still some issues with the model simulations. The simulated results and observations match very well in winter but less so in summer. In summer, the model generates clouds over the Western Pacific and South America (Fig. 5.2 JJA), which are not found in observations. This discrepancy offers at least a partial explanation for the relatively poorer model performance during summer. Furthermore, in observations ice amount in those regions might be too small to detect but in our model the detectable threshold of ice=0.1 ppmv seems to be too low. It reveals that the differences in definition of cloud between observations and models should be addressed.

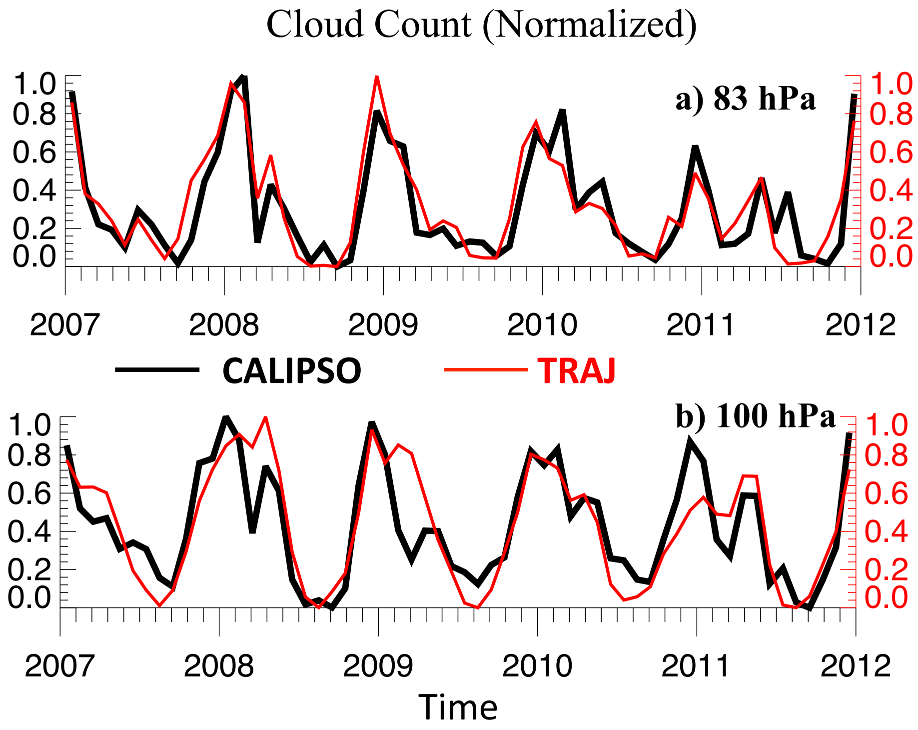

Figure 5.3. Time series of tropical cloud count (normalized) at (a) 83 hPa and (b) 100 hPa.

Successful simulation will provide us with the evolution of clouds over the long integration time. Fig. 5.4 shows the anomaly of tropic clouds reproduced by our model for the past three decades. The anomaly of temperature is also superimposed. Apparently, cloud and temperature are out of phase, which makes sense because lower temperature means more condensation, in turn making clouds more likely. From previous research we know that the QBO is a leading source of variability for water vapor (*Dessler et al.*, 2013). Well, it might also be true for clouds since the QBO variability is also obvious in Fig. 5.4. Currently we haven't quantified the impact of QBO on the cloud time series. A more detailed analysis of the time evolution of tropical clouds and polar clouds is currently in progress.

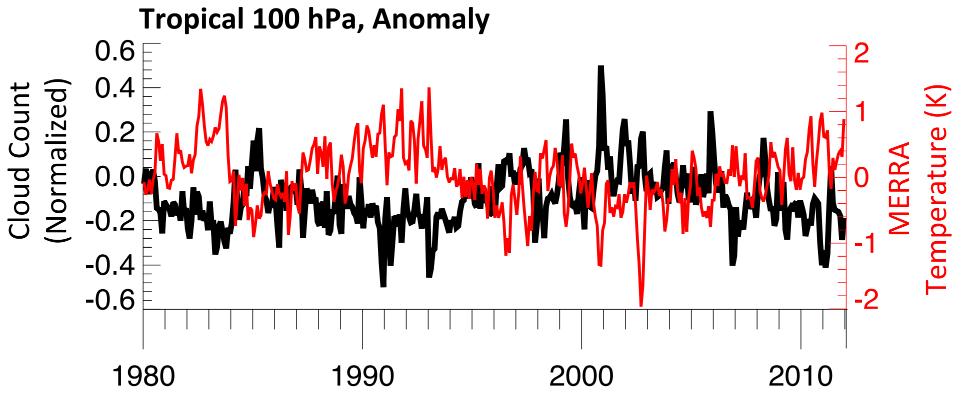

Figure 5.4. Time series of the anomaly of cloud counts predicted from our trajectory model (black) and the temperature from MERRA (red) at 100 hPa, averaged over 1980-2011.

The above analysis only includes a very simple condensation/evaporation scheme and the cloud prediction essentially depends on the large-scale transport over colder regions (Fig. 5.2). Therefore, temperature perturbations due to waves should also be included in our model. For example, we know that smaller scale gravity waves could also result in cloud formation on smaller spatial scales. Hence, we will re-run the model with gravity wave (the scheme by *Jensen and Pfister* [2004]) included to see their effect on clouds formation. In addition, we also know that clouds may form in regions subject to negative temperature anomalies associated with cold phases of large-scale equatorial Kelvin waves in the TTL [*Immler et al.*, 2008; *Fujiwara et al.*, 2009]. Therefore, in the future we intend to include Kelvin wave perturbations [using scheme developed by *Dinh et al.*, 2012] into our model to see if the cloud prediction will be improved.

5.2.3 Exploring the H_2O Enhancements During North American Monsoon

Both the Asian Monsoon (AM) and the North American Monsoon (NAM) are characterized by distinct rainfall maxima accompanied with an upper-level anticyclone. This unique system is found to have significant impact on water vapor distributions in the

Upper Troposphere and Lower Stratosphere (UTLS). Since our model is successful in reproducing water vapor distributions, we propose to examine the UTLS water vapor representations from MLS observations and our trajectory model to investigate their distinct behaviors in response to the Asian Monsoon and the North American Monsoon.

In Fig. 5.5 we see that our trajectory model can reproduce the upward tilting in enhanced H_2O from AM at 147 hPa to NAM at 100 hPa very well as compared with MLS observations, although quantitative differences exists. In Sect. 3 we have shown that those differences in water vapor amount are within uncertainties as long as the patterns agree (Fig. 3.7).

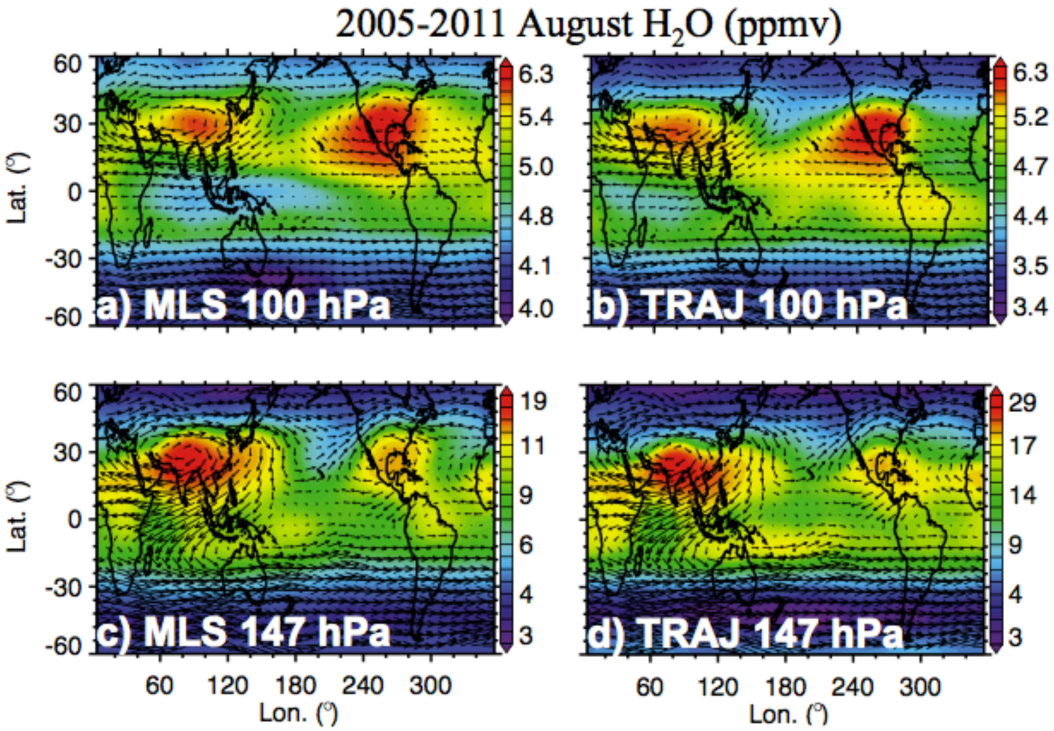

Figure 5.5. August H_2O climatology observed by MLS (panel a, c) and simulated by trajectory model (panel b, d), averaged over 2005-2011. Here the trajectory is driven by winds and temperatures from ERAi. The overlaid black vectors are the ERAi wind vectors from ERAi shown to indicate the anti-cyclone feature during Asian Monsoon (AM) and the North American Monsoon (NAM).

Fig. 5.5 shows how powerful the trajectory model is for reproducing the water vapor field. An interesting question would be where did the wet parcels originate and to where are they travelling? This question is solvable in our model because we know each parcels full history along the entire integration – this is the unique advantage of the Lagrangian trajectory model.

In operation, we have each parcel tagged with a unique ID since their releasing date. Throughout the entire integration time this ID is attached to the parcel so we can easily tell the historical pathways the parcel traveled by tracing its ID. Take the 100 hPa H_2O in August 2010 (Fig. 5.6a-b) as an example. First, we find all parcels within this NAM region are quite young (two months since their initiation, Fig. 5.6c). Then we trace those parcels' IDs back to when they were initiated, and find that besides those parcels that were initiated within the NAM region itself, some parcels originally initiated at AM and Africa could also contribute to the enhanced wet parcels within NAM (Fig. 5.6d). Among them, those parcels initiated at AM were trapped in the anti-cyclone for at least one month before they were blown into the NAM. Again, this information is unique to trajectory modeling.

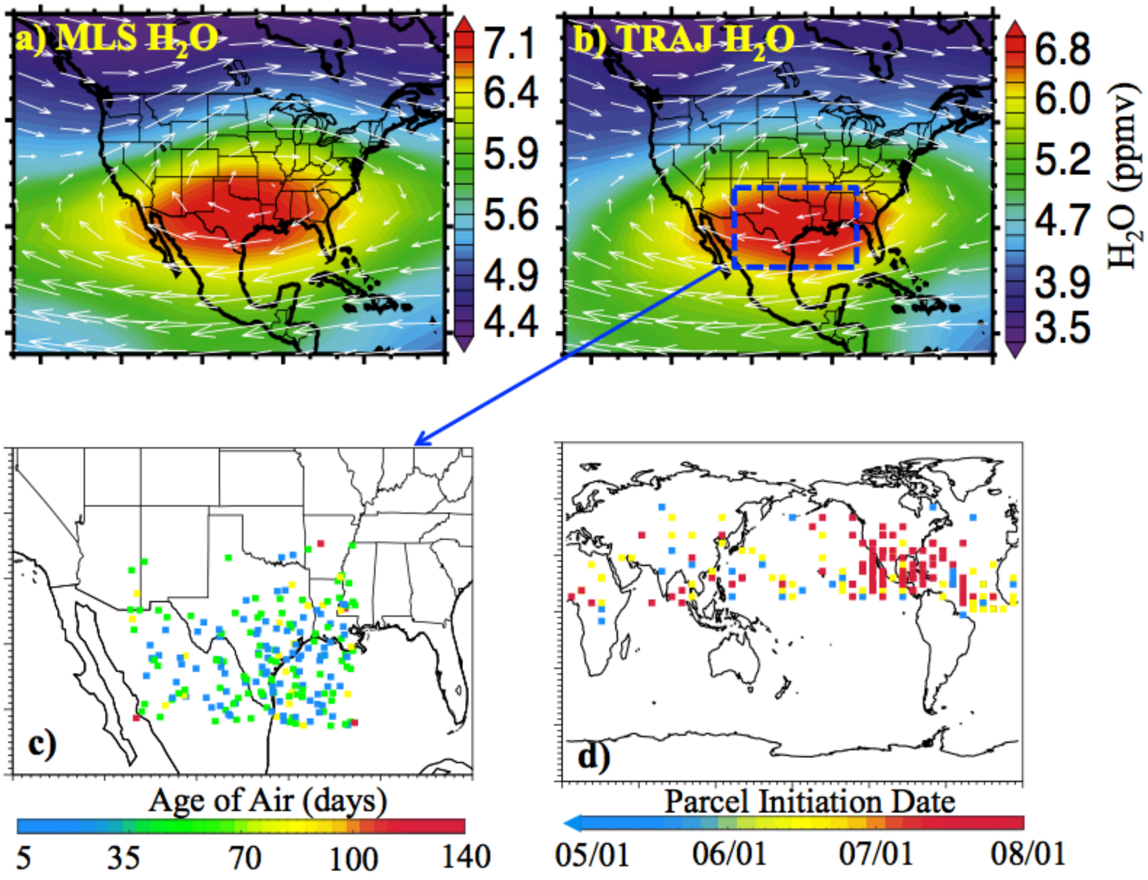

Figure 5.6. Climatological August H_2O observed by MLS, averaged over 2005-2011. The overlaid black vectors are the wind vectors from MERRA reanalysis shown to indicate the anti-cyclone feature during Asian Monsoon (AM) and the North American Monsoon (NAM).

5.2.4 Other Work

Our simulations with O_3 and CO have demonstrated the viability of the domain-filling forward trajectory model for simulating species with relatively simple chemistry in the UTLS, and extension to other species would be straightforward. There are several potential applications for such a trajectory model, including describing parcel histories that characterize different transport pathways, and evaluating the importance of tropical-extratropical exchanges. For example, trajectories can allow the sources of CO-rich air to be traced in the summertime Asian monsoon region. Quantifying the fate of the parcels after anticyclone breakup is also possible. The model lends itself to detailed comparisons of transport based on different and new reanalysis data sets, or to idealized studies of the chemical responses to UTLS circulation in a changing climate.

REFERENCES

Abalos, M., Randel, W. J., and Serrano, E. (2012), Variability in upwelling across the tropical tropopause and correlations with tracers in the lower stratosphere, Atmos. Chem. Phys., 12, 11505-11517, doi:10.5194/acp-12-11505-2012.

Abalos, M., Randel, W. J., Kinnison, D. E., and Serrano, E. (2013a), Quantifying tracer transport in the tropical lower stratosphere using WACCM, Atmos. Chem. Phys., 13, 10591-10607, doi:10.5194/acp-13-10591-2013.

Abalos, M., F. Ploeger, P. Konopka, W.J. Randel, and E. Serrano (2013b), Ozone seasonality above the tropical tropopause: reconciling the Eulerian and Lagrangian perspectives of transport processes. Atmos. Chem. Phys., 13, 10787-10794, doi:10.5194/acp-13-10787-2013.

Allen, D. R., J. L. Stanford, N. Nakamura, M. A. Lopez-Valverde, M. Lopez-Puertas, F. W. Taylor, and J. J. Remedios (2000), Antarctic polar descent and planetary wave activity observed in ISAMS CO from April to July 1992, Geophys. Res. Lett., 27(5), 665–668, doi:10.1029/1999GL010888.

Anderson, James G., David M. Wilmouth, Jessica B. Smith, and David S. Sayres (2012), UV dosage levels in summer: increased risk of ozone loss from convectively injected water vapor, Science 337, 835.

Andrews, D. G., Holton, J. R., and Leovy, C. B. (1987), Middle Atmosphere Dynamics, Academic Press, Orlando, Florida, 489 pp.

Anthes, R. A., et al. (2008), The COSMIC/FORMOSAT-3 - Mission early results, Bull. Am. Met. Soc., 89, doi: 10.1175/bams-89-3-313, 313-333.

Barnes, D. H., S. C. Wofsy, B. P. Fehlau, E. W. Gottlieb, J. W. Elkins, G. S. Dutton, and S. A. Montzka (2003), Urban/industrial pollution for the New York City–Washington, D. C., corridor, 1996–1998: 1. Providing independent verification of CO and PCE emissions inventories, J. Geophys. Res., 108, doi:10.1029/2001JD001116.

Bergman, J. W., F. Fierli, E. J. Jensen, S. Honomichl, and L. L. Pan (2013), Boundary layer sources for the Asian anticyclone: Regional contributions to a vertical conduit, J. Geophys. Res. Atmos., 118, 2560–2575, doi:10.1002/jgrd.50142.

Bernath, P. F., et al. (2005), Atmospheric Chemistry Experiment (ACE): Mission overview, Geophys. Res. Lett., 32, L15S01, doi:10.1029/2005GL022386.

Beyerle, G., Schmidt, T., Michalak, G., Heise, S., Wickert, J., and Reigber, Ch. (2005), GPS radio occultation with GRACE: Atmospheric profiling utilizing the zero difference technique, Geophys. Res. Lett., 32, L13806, doi:10.1029/2005GL023109.

Bowman, K. P. (1993), Large-scale isentropic mixing properties of the Antarctic polar vortex from analyzed winds, J. Geophys. Res., 98, 23013-23027.

Bowman, K. P., and G. D. Carrie (2002), The mean-meridional transport circulation of the troposphere in an idealized GCM, J. Atmos. Sci., 59, 1502-1514.

Bowman, Kenneth P., John C. Lin, Andreas Stohl, Roland Draxler, Paul Konopka, Arlyn Andrews, Dominik Brunner (2013), Input data requirements Lagrangian trajectory models. Bull. Amer. Meteor. Soc., 94, 1051–1058. doi: http://dx.doi.org/10.1175/BAMS-D-12-00076.1

Brewer, A. W. (1949), Evidence for a world circulation provided by the measurements of helium and water vapor distribution in the stratosphere, Q. J. R. Meteorol. Soc., 75, 351–363.

Chapman, S. (1930), A theory of upper-atmospheric ozone, Mem. R. Meteorol. Soc., 3, 103–125.

Clerbaux, C., et al. (2008), CO measurements from the ACE-FTS satellite instrument: data analysis and validation using ground-based, airborne and spaceborne observations, Atmos. Chem. Phys., 8, 2569–2594, doi:10.5194/acp-8-2569-2008.

Clancy, R. T., D. O. Muhleman, and M. Allen (1984), Seasonal variability of CO in the terrestrial mesosphere, J. Geophys. Res., 89(D6), 9673–9676.

Crutzen, P.J. (1973), A discussion of the chemistry ofsome minor constituentsin the stratosphere and troposphere, Pure App. Geophys., 106-109, 1385-1399.

Crutzen, P. J. (1971), Ozone production rates in an oxygen-hydrogen-nitrogen oxide atmosphere, J. Geophys. Res., 76(30), 7311–7327, doi:10.1029/JC076i030p07311.

Danielsen, Edwin F. (1961), Trajectories: isobaric, isentropic, and actual, J. Meteor., 18, 479–486.doi: http://dx.doi.org/10.1175/1520-0469(1961)018<0479:TIIAA>2.0.CO;2

Dee, D. P., et al. (2011), The ERA-Interim reanalysis: configuration and performance of the data assimilation system, Q. J. R. Meteorol. Soc., 137(656), 553–597, doi:10.1002/qj.828.

Dessler, A. E. (1998), A reexamination of the "stratospheric fountain" hypothesis, Geophys. Res. Lett., 25(22), 4165–4168, doi:10.1029/1998GL900120.

Dessler, A. E. (2000), The chemistry and physics of stratospheric ozone, International Geophysics Series, Vol. 74, Academic Press, San Diego, 221 pp.

Dessler, A. E. (2002), The effect of deep, tropical convection on the tropical tropopause layer, J. Geophys. Res., 107(D3), 4033, doi:10.1029/2001JD000511.

Dessler, A. E., and K. Minschwaner (2007), An analysis of the regulation of tropical tropospheric water vapor, J. Geophys. Res., 112, D10120, doi: 10.1029/2006JD007683.

Dessler, A. E., M. R. Schoeberl, T. Wang, S. M. Davis, and K. H. Rosenlof (2013), Stratospheric water vapor feedback, PNAS, 1310344110v1-201310344.

Diallo, M., Legras, B., and Chédin, A. (2012), Age of stratospheric air in the ERA-Interim, Atmos. Chem. Phys., 12, 12133-12154, doi:10.5194/acp-12-12133-2012.

Dinh, T., Durran, D. R., and Ackerman, T. (2012), Cirrus and water vapor transport in the tropical tropopause layer – Part 1: A specific case modeling study, Atmos. Chem. Phys., 12, 9799-9815, doi:10.5194/acp-12-9799-2012.

Farman, J. C.B. G. GardinerJ. D. Shanklin (1985), Large losses of total ozone in Antarctica reveal seasonal ClOx/NOx, interactions, Nature, 315, 207–210.

Fischer, H., et al. (2000), Tracer correlations in the northern high latitude lowermost stratosphere: Influence of cross-tropopause mass exchange, Geophys. Res. Lett., 27(1), 97–100, doi:10.1029/1999GL010879.

Fleming, E. L., C. H. Jackman, D. K. Weisenstein, and M. K. W. Ko (2007), The impact of interannual variability on multidecadal total ozone simulations, J. Geophys. Res., 112, D10310, doi: 10.1029/2006jd007953.

Folkins, I., C. Braun, A. M. Thompson, and J. Witte (2002), Tropical ozone as an indicator of deep convection, J. Geophys. Res., 107(D13), doi:10.1029/2001JD001178.

Forkman, P., P. Eriksson, D. Murtagh, and P. Espy (2005), Observing the vertical branch of the mesospheric circulation at latitude 60°N using ground-based measurements of CO and H2O, J. Geophys. Res., 110, D05107, doi:10.1029/2004JD004916.

Forster, P. M. F. and Shine, K. P. (1997), Radiative forcing and temperature trends from stratospheric ozone changes, J. Geophys. Res., 102, 10841–10855.

Forster, P. M. and Shine, K. P. (1999), Stratospheric water vapour changes as a possible contributor to observed stratospheric cooling, Geophys. Res. Lett., 26(21), 3309–3312, doi:10.1029/1999GL010487.

Forster, P., Ramaswamy, V., et al.: Changes in atmospheric constituents and in radiative forcing, in: climate change 2007 (2007), The Physical Science Basis. Contribution of Working Group I to the Fourth Assessment Report of the Intergovernmental Panel on Climate Change, edited by Solomon, S., Qin, D., Manning, M., Chen, Z., Marquis, M., Averyt, K. B., Tignor, M., and Miller, H. L., Cambridge University Press, Cambridge, United Kingdom and New York, NY, USA.

Froidevaux, L.,, et al. (2008), Validation of Aura Microwave Limb Sounder stratospheric ozone measurements, J. Geophys. Res., 113, D15S20, doi:10.1029/2007JD008771.

Fueglistaler, S., M. Bonazzola, P. H. Haynes, and T. Peter (2005), Stratospheric water vapor predicted from the Lagrangian temperature history of air entering the stratosphere in the tropics, J. Geophys. Res., 110(D8), D08107, doi:10.1029/2004JD005516.

Fueglistaler, S., and P. H. Haynes (2005), Control of interannual and longer-term variability of stratospheric water vapor, J. Geophys. Res., 110, D24108, doi:10.1029/2005JD006019.

Fueglistaler, S., A. Dessler, T. Dunkerton, I. Folkins, Q. Fu, and P. W. Mote (2009a), Tropical tropopause layer, Rev. Geophys., 47, RG1004, doi:10.1029/2008RG000267.

Fueglistaler, S., B. Legras, A. Beljaars, J.-J. Morcrette, A. Simmons, A. M. Tompkins, and S. Uppala (2009b), The diabatic heat budget of the upper troposphere and lower/mid stratosphere in ECMWF reanalyses, Q. J. R. Meteorol. Soc., 135, 21–37, doi:10.1002/qj.361.

Fueglistaler, S., et al. (2013), The relation between atmospheric humidity and temperature trends for stratospheric water, J. Geophys. Res. Atmos., 118, 1052–1074, doi:10.1002/jgrd.50157.

Fujiwara, M., et al. (2009), Cirrus observations in the tropical tropopause layer over the western Pacific, J. Geophys. Res., 114, D09304, doi:10.1029/2008JD011040.

Gettelman, A. and P. M. de Forster (2002), Definition and climatology of the tropical tropopause layer. Journal of the Meteorological Society of Japan, 80:4B, 911-924.

Gettelman, A., P. M. de F. Forster, M. Fujiwara, Q. Fu, H. Vömel, L. K. Gohar, C. Johanson, and M. Ammerman (2004), Radiation balance of the tropical tropopause layer, J. Geophys. Res., 109, D07103, doi:10.1029/2003JD004190.

Gettelman, A., P. Hoor, L. L. Pan, W. J. Randel, M. I. Hegglin, and T. Birner (2011), The extratropical upper troposphere and lower stratosphere, Rev. Geophys., 49, RG3003, doi:10.1029/2011RG000355.

Hajj, G. A., Ao, C. O., Iijima, B. A., Kuang, D., Kursinski, E.R., Mannucci, A. J., Meehan, T. K., Romans, L. J., de La Torre Juarez, M., and Yunck, T. P. (2004):

CHAMP and SAC-C atmospheric occultation results and intercomparisons, J. Geophys. Res., 109, D06109, doi:10.1029/2003JD003909.

Hampson J. (1964), "Chemical Instability of the Stratosphere", paper presented at the International Association of Meteorology and Atmospheric Physics (IUGG) Symposium on Atmospheric Radiation, Leningrad, USSR.

Held, I. M., and B. J. Soden (2000), Water vapor feedback and global warming, Annu. Rev. Energy Environ., 25, 441–475.

Highwood, E. J., and B. J. Hoskins (1998), The tropical tropopause, Q. J. R. Meteorol. Soc., 124, 1579–1604.

Ho, S. P., M. Goldberg, Y. H. Kuo, C. Z. Zou, and W. Schreiner (2009), Calibration of temperature in the lower stratosphere from microwave measurements using COSMIC radio occultation Data: Preliminary Results, Terrestrial Atmospheric and Oceanic Sciences, 20, doi:10.3319/tao.2007.12.06.01(f3c), 87-100.

Holton, J. R., P. H. Haynes, M. E. McIntyre, A. R. Douglass, R. B. Rood, and L. Pfister (1995), Stratosphere-troposphere exchange, Rev. Geophys., 33, 403–439.

Homeyer, C. R., K. P. Bowman, L. L. Pan, E. L. Atlas, R.-S. Gao, and T. L. Campos (2011), Dynamical and chemical characteristics of tropospheric intrusions observed during START08, J. Geophys. Res., 116, D06111, doi:10.1029/2010JD015098.

Hoskins, B. J. (1991), Toward a PV-theta view of the general circulation, Tellus, Ser. A, 43, 27–35.

Huang, L., Fu, R., Jiang, J. H., Wright, J. S., and Luo, M. (2012), Geographic and seasonal distributions of CO transport pathways and their roles in determining CO centers in the upper troposphere, Atmos. Chem. Phys., 12, 4683–4698, doi:10.5194/acp-12-4683-2012, 2012.

Hunt, B. G. (1966), The need for a modified photochemical theory of the ozonesphere, J. Atmos. Sci. 23: 88-95.

Immler, F., K. Krüger, S. Tegtmeier, M. Fujiwara, P. Fortuin, G. Verver, and O. Schrems (2007), Cirrus clouds, humidity, and dehydration in the tropical tropopause layer observed at Paramaribo, Suriname (5.8N, 55.2W), J. Geophys. Res., 112, D03209, doi:10.1029/2006JD007440.

Jensen, E., O. Toon, H. Selkirk, J. Spinhirne, and M. Schoeberl (1996), On the formation and persistence of subvisible cirrus clouds near the tropical tropopause, J. Geophys. Res., 101(D16), 21,361–21,37.

Jensen, E., and L. Pfister (2004), Transport and freeze-drying in the tropical tropopause layer, J. Geophys. Res., 109, D02207, doi:10.1029/2003JD004022.

Jensen, E. J., Ackerman, A. S., and Smith, J. A. (2007), Can overshooting convection dehydrate the tropical tropopause layer?, J. Geophys. Res., 112, D11209, doi:10.1029/2006JD007943.

Jiang, J. H., N. J. Livesey, H. Su, L. Neary, J. C. McConnell, and N. A. D. Richards (2007), Connecting surface emissions, convective uplifting, and long-range transport of carbon monoxide in the upper troposphere: New observations from the Aura Microwave Limb Sounder, Geophys. Res. Lett., 34, L18812, doi:10.1029/2007GL030638.

Johnston, H. S. (1971), Reduction of stratospheric ozone by nitrogen oxide catalysts from supersonic transport exhaust, Science, 173: 517-522.

Kalnay et al. (1996), The NCEP/NCAR 40-year reanalysis project, Bull. Amer. Meteor. Soc., 77, 437-470.

Kar, J., et al. (2004), Evidence of vertical transport of carbon monoxide from Measurements of Pollution in the Troposphere (MOPITT), Geophys. Res. Lett., 31, L23105, doi:10.1029/2004GL021128.

Kinnison, D. E., et al. (2007), Sensitivity of chemical tracers to meteorological parameters in the MOZART-3 chemical transport model, J. Geophys. Res., 112, D20302, doi:10.1029/2006JD007879.

Kley, D., et al. (2000), SPARC Assessment of upper tropospheric and stratospheric water vapour, WCRP 113, WMO/TD No. 1043, SPARC Rep. No. 2, World Meteorol. Organ., Geneva.

Konopka, P., J.-U. Grooß, F. Plöger, and R. Müller (2009), Annual cycle of horizontal in-mixing into the lower tropical stratosphere, J. Geophys. Res., 114, D19111, doi:10.1029/2009JD011955.

Konopka, P., J.U. Grooss, G. Gunther, F. Ploeger, R. Pommrich, R. Mueller, N. Livesey (2010), Annual cycle of ozone at and above the tropical tropopause: observations versus simulations with the Chemical Lagrangian Model of the Stratosphere (CLaMS), vol doi:10.5194/acp-10-121-2010, num 9.

Kunz, A., L. L. Pan, P. Konopka, D. E. Kinnison, and S. Tilmes (2011), Chemical and dynamical discontinuity at the extratropical tropopause based on START08 and WACCM analyses, J. Geophys. Res., 116, D24302, doi:10.1029/2011JD016686.

Lacis, A., Wuebbles, D. J., and Logan, J. A. (1990), Radiative forcing of climate by changes in the vertical distribution of ozone, J. Geo- phys. Res., 95, 9971–9981.

Lamarque, J.-F., et al. (2012), CAM-chem: description and evaluation of interactive atmospheric chemistry in the Community Earth System Model, Geosci. Model Dev., 5, 369-411, doi:10.5194/gmd-5-369-2012.

Levy, H., J. D. Mahlmann, W. J. Moxim, and S. C. Liu (1985), Tropospheric ozone: The role of transport, J. Geophys. Res., 90, 3753–3772.

Liebmann, B. and Smith, C. A. (1996), Description of a complete (interpolated) outgoing longwave radiation data set, B. Am. Meteorol. Soc., 77, 1275–1277.

Lin, Shian-Jiann, (2004), A "vertically Lagrangian" finite-volume dynamical core for global models. Mon. Wea. Rev., 132, 2293–2307. doi: http://dx.doi.org/10.1175/1520-0493(2004)132<2293:AVLFDC>2.0.CO;2

Lin, Shian-Jiann, D. Brunner, and C. Gerbig (2011), Improving and applying Lagrangian models of the atmosphere. Eos, Trans. Amer. Geophys. Union, 93, 32, doi:10.1029/2012EO030010.

Liu, C., E. Zipser, T. Garrett, J. H. Jiang, and H. Su (2007), How do the water vapor and carbon monoxide "tape recorders" start near the tropical tropopause? Geophys. Res. Lett., 34, L09804, doi:10.1029/2006GL029234.

Liu, Y. S., S. Fueglistaler, and P. H. Haynes (2010), Advection-condensation paradigm for stratospheric water vapor, J. Geophys. Res., 115, D24307, doi: 10.1029/2010jd014352.

Livesey, N. J., et al. (2008), Validation of Aura Microwave Limb Sounder O3 and CO observations in the upper troposphere and lower stratosphere, J. Geophys. Res., 113, D15S02, doi:10.1029/2007JD008805.

Logan, J., Prather, M., Wofsy, S. and McElroy, M. (1981). Tropospheric chemistry: A global perspective. Journal of Geophysical Research 86. doi: 10.1029/0JGREA0000860000C8007210000001. issn: 0148-0227.

McFarquhar, G., A. Heymsfield, J. Spinhirne, and B. Hart (2000), Thin and subvisual tropopause tropical cirrus: Observations and radiative impacts, J. Atmos. Sci., 57, 1841–1853, doi:10.1175/1520-0469(2000)057<1841:TASTTC>2.0.CO;2.

Minschwaner, K., et al. (2010), The photochemistry of carbon monoxide in the stratosphere and mesosphere evaluated from observations by the Microwave Limb Sounder on the Aura satellite, J. Geophys. Res., 115, D13303, doi:10.1029/2009JD012654.

Molina, M. J., F. S. Rowland (1974), Stratospheric sink for chlorofluoromethanes: chlorine atom catalyzed destruction of ozone, Nature, 249, 810–814.

Mote, P. W., K. H. Rosenlof, M. E. McIntyre, E. S. Carr, J. C. Gille, J. R. Holton, J. S. Kinnersley, and H. C. Pumphrey (1996), An atmospheric tape recorder: the imprint of tropical tropopause temperatures on stratospheric water vapor, J. Geophys. Res., 101,3989–4006.

Murphy, D. M. and Koop, T. (2005), Review of the vapour pressures of ice and supercooled water for atmospheric applications, Q. J. Roy. Meteor. Soc., 131, 1539–1565.

Oltmans, S. J., and D. J. Hofmann (1995), Increase in lower-stratospheric water vapor at a mid-latitude site from 1981 to 1994, Nature, 374, 146–149.

Oltmans, S. J., H. Voemel, D. J. Hofmann, K. H. Rosenlof, and D. Kley (2000), The increase in stratospheric water vapor from balloon borne, frostpoint hygrometer measurements at Washington, D. C., and Boulder, Colorado, Geophys. Res. Lett., 27, 3453–3457.

Onogi, K., J.Tsutsui, H.Koide, M. Sakamoto, S. Kobayashi, H. Hatsushika, T. Matsumoto, N. Yamazaki, H. Kamahori, K. Takahashi, S. Kadokura, K. Wada, K. Kato, R. Oyama, T. Ose, N. Mannoji and R. Taira (2007): The JRA-25 Reanalysis. J. Meteor. Soc. Japan, 85, 369-432.

Pan, L. L., W. J. Randel, B. L. Gary, M. J. Mahoney, and E. J. Hintsa (2004), Definitions and sharpness of the extratropical tropopause: A trace gas perspective, J. Geophys. Res., 109, D23103, doi:10.1029/2004JD004982.

Pan, L. L., L. Paulik, S. B. Honomichl, L. A. Munchak, J. C. Bian, and H. Selkirk, and H. Vömel, Identification of the tropical tropopause transition layer using the ozone-water vapor relationship (2013), J. Geophys. Res. doi: 10.1002/2013JD020558.

Park, M., W. J. Randel, L. K. Emmons, and N. J. Livesey (2009), Transport pathways of carbon monoxide in the Asian summer monsoon diagnosed from Model of Ozone and Related Tracers (MOZART), J. Geophys. Res., 114, D08303, doi:10.1029/2008JD010621.

Park, M., W. J. Randel, D. E. Kinnison, L. K. Emmons, P. F. Bernath, K. A. Walker, C. D. Boone, and N. J. Livesey (2013), Hydrocarbons in the upper troposphere and lower stratosphere observed from ACE-FTS and comparisons with WACCM, J. Geophys. Res. Atmos., 118, 1964–1980, doi:10.1029/2012JD018327.

Ploeger, F., P. Konopka, G. Gunther, J. U. Grooss, and R. Muller (2010), Impact of the vertical velocity scheme on modeling transport in the tropical tropopause layer, J. Geophys. Res., 115, D03301, doi: 10.1029/2009jd012023.

Ploeger, F., P. Konopka, R. Müller, S. Fueglistaler, T. Schmidt, J. C. Manners, J.-U. Grooß, G. Günther, P. M. Forster, and M. Riese (2012), Horizontal transport affecting trace gas seasonality in the Tropical Tropopause Layer (TTL), J. Geophys. Res., 117, D09303, doi:10.1029/2011JD017267.

Pressman and Warneck (1970), The stratosphere as a chemical sink for carbon monoxide. J. Atmos. Sci., 27, 155–163.

Pumphrey, H. C., et al. (2007), Validation of middle-atmosphere carbon monoxide retrievals from the Microwave Limb Sounder on Aura, J. Geophys. Res., 112, D24S38, doi:10.1029/2007JD008723.

Pumphrey, H. C., C. Boone, K. A. Walker, P. Bernath, and N. J. Livesey (2008), Tropical tape recorder observed in HCN, Geophys. Res. Lett., 35, L05801, doi:10.1029/2007GL032137.

Randel, W.J., R.R. Garcia and F. Wu (2002), Time dependent upwelling in the tropical lower stratosphere estimated from the zonal mean momentum budget. J. Atmos. Sci., 59, 2141-2152.

Randel, W. J., F. Wu, and W. Rivera Ríos (2003), Thermal variability of the tropical tropopause region derived from GPS/MET observations, J. Geophys. Res., 108(D1), 4024, doi:10.1029/2002JD002595.

Randel, W.J., F. Wu, S. Oltmans, K. Rosenlof and G. Nedoluha (2004), Interannual changes of stratospheric water vapor and correlations with tropical tropopause temperatures. J. Atmos. Sci., 61, 2133-2148.

Randel, W. J., and M. Park (2006), Deep convective influence on the Asian summer monsoon anticyclone and associated tracer variability observed with Atmospheric Infrared Sounder (AIRS), J. Geophys. Res., 111, D12314, doi:10.1029/2005JD006490.

Randel, W. J., et. al, (2007), A large annual cycle in Ozone above the tropical tropopause Linked to the Brewer–Dobson Circulation. J. Atmos. Sci., 64, 4479–4488.

Randel, W. J., M. Park, L. Emmons, D. Kinnison, P. Bernath, K. Walker, C. Boone and H. Pumphrey (2010), Asian monsoon transport of pollution to the stratosphere, Science, 328, 611–613, doi:10.1126/science.1182274.

Randel, W.J., and E.J. Jensen (2013), Physical processes in the tropical tropopause layer and their role in a changing climate. Nature Geoscience, 6, 169-176, doi:10.1038/ngeo1733

Read, W. G., et al. (2007), Aura Microwave Limb Sounder upper tropospheric and lower stratospheric H2O and relative humidity with respect to ice validation, J. Geophys. Res., 112, D24S35, doi:10.1029/2007JD008752.

Read, W. G., M. J. Schwartz, A. Lambert, H. Su, N. J. Livesey, W. H. Daffer, and C. D. Boone (2008), The roles of convection, extratropical mixing, and in situ freeze-drying in the tropical tropopause layer, Atmos. Chem. Phys., 8, 6051–6067, doi:10.5194/acp-8-6051-2008.

Reid, G. C., and K. S. Gage (1996), The tropical tropopause over the western Pacific: Wave driving, convection, and the annual cycle, J. Geophys. Res., 101(D16), 21,233–21,241, doi:10.1029/96JD01622.

Rienecker, M. M., et al. (2011), MERRA - NASA's Modern-Era Retrospective Analysis for Research and Applications. J. Climate, 24, 3624–3648, doi:10.1175/JCLI-D-11-00015.1.

Rosenfield, J. E., D. B. Considine, M. R. Schoeberl, and E. V. Browell (1998), The impact of subvisible cirrus clouds near the tropical tropopause on stratospheric water vapor, Geophys. Res. Lett., 25(11), 1883–1886, doi:10.1029/98GL01294.

Rosenlof, K. H. (1995), The seasonal cycle of the residual mean meridional circulation in the stratosphere, J. Geophys. Res., 100,5173–5191.

Rosenlof, K. H., et al. (2001), Stratospheric water vapor increases over the past half-century, Geophys. Res. Lett., 28, 1195–1198.

Sachse, G. W., R. C. Harriss, J. Fishman, G. F. Hill, and D. R. Cahoon (1988), Carbon monoxide over the Amazon basin during the 1985 dry season, J. Geophys. Res., 93, 1422–1430.

Saha, S., et al. (2010), THE NCEP climate forecast system reanalysis Bull. Am. Met. Soc., 91, doi: 10.1175/2010bams3001.1, 1015-1057.

Schnadt Poberaj, C., Staehelin, J., Brunner, D., Thouret, V., De Backer, H., and Stübi, R. (2009), Long-term changes in UT/LS ozone between the late 1970s and the 1990s deduced from the GASP and MOZAIC aircraft programs and from ozonesondes, Atmos. Chem. Phys., 9, 5343-5369, doi:10.5194/acp-9-5343-2009.

Schoeberl, M., L. Sparling (1995), Trajectory modelling. in diagnostic tools in atmospheric physics. Proceedings of the International School of Physics“ Enrico Fermi”, Course CXXIV, held June 22-July 2, 1993, at Verenna on Lake Como, Villa Monastero. Edited by G. Fiocco and G. Visconti. Published by IOS Press, OHM (Ohmsha), Amsterdam, 1995, p. 289.

Schoeberl, M. R., A. R. Douglass, Z. Zhu, and S. Pawson (2003), A comparison of the lower stratospheric age spectra derived from a general circulation model and two data assimilation systems, J. Geophys. Res., 108, 4113, doi:10.1029/2002JD002652, D3.

Schoeberl, M. R., B. N. Duncan, A. R. Douglass, J. Waters, N. Livesey, W. Read, and M. Filipiak (2006), The carbon monoxide tape recorder, Geophys. Res. Lett., 33, L12811, doi:10.1029/2006GL026178.

Schoeberl, M. R., et al. (2008), QBO and annual cycle variations in tropical lower stratosphere trace gases from HALOE and Aura MLS observations, J. Geophys. Res., 113, D05301, doi:10.1029/2007JD008678.

Schoeberl, M. R. and Dessler, A. E. (2011), Dehydration of the stratosphere, Atmos. Chem. Phys., 11, 8433-8446, doi:10.5194/acp-11-8433-2011.

Schoeberl, M. R., Dessler, A. E., and Wang, T. (2012), Simulation of stratospheric water vapor and trends using three reanalyses, Atmos. Chem. Phys., 12, 6475-6487, doi:10.5194/acp-12-6475-2012, 2012.

Schoeberl, M. R., Dessler, A. E., and Wang, T. (2013), Modeling upper tropospheric and lower stratospheric water vapor anomalies, Atmos. Chem. Phys., 13, 7783-7793, doi:10.5194/acp-13-7783-2013.

Seidel, D. J., R. J. Ross, J. K. Angell, and G. C. Reid (2001), Climatological characteristics of the tropical tropopause as revealed by radiosondes, J. Geophys. Res., 106(D8), 7857–7878, doi:10.1029/2000JD900837.

Seiler, W. and Junge, C. (1969), Decrease of carbon monoxide mixing ratio above the polar tropopause. Tellus, 21: 447–449. doi: 10.1111/j.2153-3490.1969.tb00459.x

Sherwood, S. C. (2000), A stratospheric “drain” over the Maritime Continent, Geophys. Res. Lett., 27, 677–680.

Sherwood, S. C., and A. E. Dessler (2000), On the control of stratospheric humidity, Geophys. Res. Lett., 27, 2513–2516.

Solomon, S., R. R. Garcia, J. J. Olivero, R. M. Bevilacqua, P. R. Schwartz, R. T. Clancy, and D. O. Muhleman (1985), Photochemistry and transport of carbon monoxide in the middle atmosphere, J. Atmos. Sci., 42, 1072–1083.

Solomon, S., Rosenlof, K. H., Portmann, R. W., Daniel, J. S., Davis, S. M., Sanford, T. J., and Plattner, G.-K. (2010): Contributions of stratospheric water vapor to decadal changes in the rate of global warming, Science, 327, 1219–1223.

SPARC CCMVal (2010), SPARC Report on the evaluation of chemistry-climate models, V. Eyring, T. G. Shepherd, D. W. Waugh (Eds.), SPARC Report No. 5, WCRP-132, WMO/TD-No. 1526, http://www.atmosp.physics.utoronto.ca/SPARC.

Stohl, A. (1998), Computation, accuracy and applications of trajectories—A review and bibliography. Atmos. Environ., 32, 947–966.

Stohl, A., Seibert, P., Wotawa, G., Arnold, D., Burkhart, J. F., Eckhardt, S., Tapia, C., Vargas, A., and Yasunari, T. J. (2012), Xenon-133 and caesium-137 releases into the atmosphere from the Fukushima Dai-ichi nuclear power plant: determination of the source term, atmospheric dispersion, and deposition, Atmos. Chem. Phys., 12, 2313-2343, doi:10.5194/acp-12-2313-2012.

Uppala, S. M., D. Dee, S. Kobayashi, P. Berrisford, and A. Simmons (2008), Towards a climate data assimilation system: Status update of ERA-Interim, ECMWF Newslett., 115, 12–18.

Vogel, B., T. Feck, and J.-U. Grooß (2011), Impact of stratospheric water vapor enhancements caused by CH_4 and H_2O increase on polar ozone loss, J. Geophys. Res., 116, D05301.

Wang, T., and A. E. Dessler (2012), Analysis of cirrus in the tropical tropopause layer from CALIPSO and MLS data: A water perspective, J. Geophys. Res., 117, D04211, doi:10.1029/2011JD016442.

Wang, T., Randel, W. J., Dessler, A. E., Schoeberl, M. R., and Kinnison, D. E. (2014), Trajectory model simulations of ozone and carbon monoxide in the Upper Troposphere and Lower Stratosphere (UTLS), Atmos. Chem. Phys. Discuss., 14, 5991-6025, doi:10.5194/acpd-14-5991-2014.

Waters, J. W., et al. (2006), The Earth Observing System Microwave Limb Sounder (EOS MLS) on the Aura satellite, IEEE Trans. Geosci. Remote Sens., 44(5), 1075–1092.

Waugh, D. W., T. M. Hall (2002), Age of stratospheric air: Theory, observations, and models, Rev. Geophys., 40 (4), doi:10.1029/2000RG000101, 1010.

Webster, H. N., and Coauthors (2012), Operational prediction of ash concentrations in the distal volcanic cloud from the 2010 Eyjafjallajökull eruption. J. Geophys. Res., 117, D00U08, doi:10.1029/2011JD016790.

Wickert, J., Reigber, C., Beyerle, G., Ko ̈nig, R., Marquardt, C., Schmidt, T., Grundwaldt, L., Galas, R., Meehan, T. K., Mel- bourne, W. G., and Hocke, K. (2001), Atmosphere sounding by GPS radio occultation: First results from CHAMP, Geophys. Res. Lett., 28, 3263–3266.

Winker, D., and C. Trepte (1998), Laminar cirrus observed near the tropical tropopause by LITE, Geophys. Res. Lett., 25(17), 3351–3354.

Wofsy, S. C., J. C. McConnell, and M. B. McElroy (1972), Atmospheric CH_4, CO, and CO_2, J. Geophys. Res., 77, doi: 10.1029/JC077i024p04477, 4477-4493.

Wright, J. S. and Fueglistaler, S. (2013), Large differences in reanalyses of diabatic heating in the tropical upper troposphere and lower stratosphere, Atmos. Chem. Phys., 13, 9565-9576, doi:10.5194/acp-13-9565-2013.

Zhou, X. L., M. A. Geller, and M. Zhang (2001), Cooling trend of the tropical cold point tropopause temperatures and its implications, J. Geophys. Res., 106, 1511–1522.